

**TWO DIMENSIONAL FINITE VOLUME WEIGHTED ESSENTIALLY  
NON-OSCILLATORY EULER SCHEMES WITH DIFFERENT FLUX  
ALGORITHMS**

**A THESIS SUBMITTED TO  
THE GRADUATE SCHOOL OF NATURAL AND APPLIED SCIENCES  
OF  
MIDDLE EAST TECHNICAL UNIVERSITY**

**BY**

**ALİ AKTÜRK**

**IN PARTIAL FULFILLMENT OF THE REQUIREMENTS**

**FOR**

**THE DEGREE OF MASTER OF SCIENCE**

**IN**

**AEROSPACE ENGINEERING**

**JULY 2005**

Approval of the Graduate School of Natural and Applied Sciences.

Prof. Dr. Canan ÖZGEN  
Director

I certify that this thesis satisfies all the requirements as a thesis for the degree of Master of Science.

Prof. Dr. Nafiz ALEMDAROĞLU  
Head of the Department

This is to certify that we have read this thesis and that in our opinion it is fully adequate, in scope and quality, as a thesis for the degree of Master of Science.

Prof. Dr. İ. Sinan AKMANDOR  
Supervisor

Examining Committee Members

Prof. Dr. M. Cevdet ÇELENLİGİL	(AEE, METU)	_____
Prof. Dr. İ. Sinan AKMANDOR	(AEE, METU)	_____
Ins. Dr. Tahsin ÇETİNKAYA	(ME, METU)	_____
Prof. Dr. Ünver KAYNAK	(ETÜ)	_____
Dr. A. Ruhşen ÇETE	(TAI)	_____

**I hereby declare that all information in this document has been obtained and presented in accordance with academic rules and ethical conduct. I also declare that, as required by these rules and conduct, I have fully cited and referenced all material and results that are not original to this work.**

Name, Last name: Ali Aktürk

Signature :

## **ABSTRACT**

### **TWO-DIMENSIONAL FINITE VOLUME WEIGHTED ESSENTIALLY NON-OSCILLATORY EULER SCHEMES WITH DIFFERENT FLUX ALGORITHMS**

Ali Aktürk

M.S., Department of Aerospace Engineering

Supervisor: Prof. Dr. İ. Sinan Akmandor

July 2005, 130 pages

The purpose of this thesis is to implement Finite Volume Weighted Essentially Non-Oscillatory (FV-WENO) scheme to solution of one and two-dimensional discretised Euler equations with different flux algorithms. The effects of the different fluxes on the solution have been tested and discussed. Beside, the effect of the grid on these fluxes has been investigated.

Weighted Essentially Non-Oscillatory (WENO) schemes are high order accurate schemes designed for problems with piecewise smooth solutions that involve discontinuities. WENO schemes have been successfully used in applications, especially for problems containing both shocks and complicated smooth solution structures. Fluxes are used as building blocks in FV-WENO scheme. The efficiency of the scheme is dependent on the fluxes used in scheme

The applications tested in this thesis are the 1-D Shock Tube Problem, Double Mach Reflection, Supersonic Channel Flow, and supersonic Staggered Wedge Cascade.

The numerical solutions for 1-D Shock Tube Problem and the supersonic channel flow are compared with the analytical solutions. The results for the Double Mach Reflection and the supersonic staggered cascade are compared with results from literature.

**Key Words:** Weighted Essentially Non-Oscillatory, Riemann solver, HLLC Flux, MUSTA flux, RUSANOV flux, LAX FRIEDRICHS flux.

# ÖZ

## İKİ BOYUTLU, SONLU HACİMLİ, AĞIRLIKLIL OLARAK ESASTAN SALINIMSIZ, DEĞİŞİK AKI ALGORİTMALARINA SAHİP EULER ŞEMALARI

Ali Aktürk

Yüksek Lisans, Havacılık Mühendisliği Bölümü

Tez Yöneticisi: Prof. Dr. İ. Sinan Akmandor

Temmuz 2005, 130 sayfa

Bu tezin amacı sonlu hacimli ve ağırlıklı olarak esastan salınımsız (FV-WENO) şemasının bir ve iki boyutlu ayrıklaştırılmış Euler denklemlerinin çözümünde değişik akı algoritmaları ile uygulanmasıdır. Değişik akıların FV-WENO şeması üzerinde ki etkileri denenmiş ve tartışılmıştır. Bunun yanında ağ yapılarının bu akı algoritmalarına etkisi araştırılmıştır.

WENO şemaları, yüksek dereceli hassasiyete sahip şemalardır ve düzgün çözüm alan parçalarının içindeki değer kırılma problemleri için tasarlanmıştır. WENO şemaları özellikle hem şoklar hem karmaşık pürüzsüz çözüm yapıları için başarılı şekilde kullanılmıştır. Akı algoritmaları FV-WENO şemalarının kurucu öğeleridir. FV-WENO şemalarının verimi akı algoritmalarına bağlıdır.

Bu tez de, tek boyutlu şok tüpü problemi, ikili Mac yansıması , ses üstü kanal akışı ve ses üstü verev kenarlı kaskad uygulamalarına yer verilmiştir.

Tek boyutlu şok tüpü problemi ve ses üstü kanal akışlarının sayısal çözümleri analitik çözümler ile karşılaştırılmıştır. İkili Mac yansıması sonuçları ve ses üstü verev kenarlı kaskad sonuçları ise yayınlanmış bulunan sonuçlarla karşılaştırılmıştır.

**Anahtar kelimeler:** Ağırlıklı olarak esastan salınımsız, Riemann Problemi, HLLC akısı, MUSTA akısı, RUSANOV akısı, LAX FRIEDRICHS akısı .

## ACKNOWLEDGMENTS

I would like to express my gratitude to my supervisor , Prof. Dr. İ. Sinan Akmandor, for his valuable guidance and support during this study. I learned so many from that I cannot express all, thanks.

I am deeply grateful to my very dear parents, Ruhiye and Kemal Aktürk, for supporting me and for showing me love and patience to carry on my work successfully.

I offer sincere thanks to my wife, Esra , for her love and support.

I would like to thank my dear friend Monier Ali El-Farra for all his help, support and valuable hints that helped me much in accomplishing this work. I offer special thanks to my dear friend Özhan Hulusi Turgut for his help, support.

Thanks also to all friends from Aerospace Engineering department. Specially I would thank to Argün Katırcı for his help and support.

Special thanks go to my colleagues at TAI for their patience and support.

# TABLE OF CONTENTS

PLAGIARISIM.....	iii
ABSTRACT.....	iv
ÖZ .....	vi
ACKNOWLEDGMENTS .....	viii
TABLE OF CONTENTS.....	ix
LIST OF TABLES.....	xii
LIST OF FIGURES .....	xiii
LIST OF SYMBOLS .....	xviii
CHAPTER	
1. INTRODUCTION .....	1
2. 2-D EULER EQUATIONS AND WENO DISCRETIZATION .....	7
2.1.    Governing Equations .....	7
2.2.    Finite Volume Formulation in Two Space Dimensions .....	8
2.3.    WENO Reconstruction in Two Space Dimensions .....	10
2.4.    One – Dimensional WENO Reconstruction .....	12
2.4.1. Reconstruction from Cell Averages.....	12
2.5.    WENO Approximations in 1-D (In Scalar Case) .....	15
2.6.    Characteristic -wise FV WENO Reconstruction .....	22
2.7.    Application of Piece-wise Parabolic WENO Approximation .....	23
2.8.    Time Discretization.....	32

3. NUMERICAL FLUXES AND BOUNDARY CONDITONS .....	35
3.1 The HLL Approximate Riemann Solver.....	35
3.2 The HLLC Approximate Riemann Solver.....	37
3.3 Wave- Speed Calculations .....	40
3.4. Lax Friedrichs Flux.....	43
3.4.1. Monotone Schemes.....	45
3.4.2.Application of Monotonicity and flux theorem to the Lax- Friedrichs Method.....	46
3.5 Lax-Wendroff Scheme.....	46
3.6 First-Order Centred (FORCE) Flux.....	47
3.7 Rusanov Flux .....	47
3.8 The Upwind MUSTA Fluxes.....	48
3.9 Boundary Conditions .....	50
3.9.1. Inflow Boundary Condition .....	50
3.9.2. Outflow Boundary Condition .....	51
3.9.3. Wall Boundary Condition (Body Surface) .....	52
3.9.4. Symmetric Wall Boundary Condition .....	55
3.9.5. Periodic Boundary Conditions.....	56
3.9.6. Ghost Points.....	56
4. RESULTS AND DISCUSSION .....	58
4.1. One Dimensional Results.....	58
4.1.1. Problem Description .....	58
4.1.2. The Sod 's Problem.....	60
4.1.3. The Lax 's Problem.....	63

4.2. Two Dimensional Results .....	67
4.2.1 Double Mach Reflection (DMR ) .....	67
4.2.2 Supersonic Channel Flow .....	73
4.2.3 Supersonic Wedge Cascade Results .....	92
5. CONCLUSIONS.....	119
REFERENCES .....	122
APPENDIX	
A. CODE DESCRIPTION AND FLOW CHARTS.....	127

# LIST OF TABLES

## TABLES

2.1 . The $C_{rj}$ constants [1]. .....	16
-----------------------------------------	----

# LIST OF FIGURES

## FIGURES

2.1. Explanation of weights and stencil choosing process for $v_{i+1/2}$ .....	21
2.2. Explanation of weights and stencil choosing process for $v_{i-1/2}$ .....	21
2.3. Reconstructed points and gaussian integraion points for one cell .....	31
3.1. Approximate HLL Riemann Solver. Solution in the Star Region Consists of a single state $Q^{hll}$ separated from data states by two waves of speeds $S_L$ and $S_R$ .....	36
3.2. Structure of the exact solution of the Riemann problem for the x-split three dimensional Euler equations. There are four wave families associated with the eigenvalues $u-a$ , $u$ (multiplicity 2) and $u+a$ .....	37
3.3. HLLC approximate Riemann Solver. Solution in the Star Region consists of two constant states separated from each other by a middle wave of speed $S^*$ .....	38
3.4. Control Volume $V=[X_{i-1/2}, X_{i+1/2}] \times [0, \Delta t/2]$ on x-t plane .....	43
3.5 .The Control Volume For Simple discretization.....	49
3.6. Properties of Supersonic inflow BC. ....	51
3.7. Properties of Supersonic Outflow BC.....	51
3.8. Properties of Subsonic Outflow BC.....	52
3.9. Symmetric Boundary Condition .....	55
3.10. Periodic boundary condition .....	56
4.1. Shock Tube at the initial state and pressure distribution [29].....	59
4.2. Solution of Sod's problem with HLLC flux at $t=0.25$ and $CFL=0.6$ .....	60
4.3. Solution of Sod's problem with Lax-Friedrich flux .....	61

4.4. Solution of Sod's problem with Musta flux.....	61
4.5. Solution of Sod's problem with Rusanov flux.....	62
4.6. Comparison of all the fluxes for Sod's Problem.....	62
4.7. Solution of Lax's problem with HLLC flux .....	64
4.8. Solution of Lax's problem with Lax-Friedrich flux. ....	64
4.9. Solution of Lax's problem with Musta flux.....	65
4.10. Solution of Lax's problem with Rusanov flux.....	65
4.11. Comparison of all the fluxes for Lax's Problem.....	66
4.12. The Computational Domain for Double Mach Reflection problem .....	67
4.13. The computational domain and 120x30 size grid used in computations .....	68
4.14. The Result of DMR problem with 120x30 grid size .....	69
4.15. The computational domain and 480x120 size grid used in computations .....	70
4.16. The Result of DMR problem with 480x120 grid size .....	71
4.17. Zoomed area of the figure 4.16.....	72
4.18. Geometry of the channel.....	73
4.19. The Grid#1 with size 82x45.....	74
4.20. The Grid#2 with size 119x65.....	74
4.21. The Grid#3 with size 241x131.....	75
4.22. The Grid#4 with size 318x150.....	75
4.23. Pressure contours for grid#1 (82x45) for Weno-HLLC .....	76
4.24. Pressure contours for grid#2 (119x65) for Weno-HLLC .....	76
4.25. Pressure contours for grid#3 (241x131) for Weno-HLLC .....	77
4.26. Pressure contours for grid#4(318x150) for Weno-HLLC .....	77
4.27. Pressure distribution on channel wall for Weno-HLLC .....	78

4.28. The convergence of the WENO-HLLC scheme with different mesh sizes .....	79
4.29. Pressure contours for grid#1 for Weno-LF .....	80
4.30. Pressure contours for grid#2 for Weno-LF .....	80
4.31. Pressure contours for grid#3 for Weno-LF .....	80
4.32. Pressure contours for grid#4 for Weno-LF .....	81
4.33. Pressure distribution on channel wall for Weno-LF .....	81
4.34. The convergence of the WENO-LF scheme with different mesh sizes .....	82
4.35. Pressure contours for grid#1 for Weno-MUSTA.....	83
4.36. Pressure contours for grid#2 for Weno-MUSTA.....	83
4.37. Pressure contours for grid#3 for Weno-MUSTA.....	83
4.38. Pressure contours for grid#4 for Weno-MUSTA.....	84
4.39. Pressure distribution on channel wall for WENO-MUSTA .....	84
4.40. The convergence of the WENO-MUSTA scheme with different mesh sizes .....	85
4.41. Pressure contours for grid#1 for Weno-RUSANOV .....	86
4.42. Pressure contours for grid#2 for Weno-RUSANOV .....	86
4.43. Pressure contours for grid#3 for Weno-RUSANOV .....	86
4.44. Pressure contours for grid#4 for Weno-RUSANOV .....	87
4.45. Pressure distribution on channel wall for Weno-RUSANOV .....	87
4.46. The convergence of the WENO-RUSANOV scheme with different mesh sizes .....	88
4.47. The pressure distribution on channel wall for all the fluxes and with grid#1 (82x45).....	89
4.48. The pressure distribution on channel wall for all the fluxes and with grid#2 (119x65).....	90

4.49. The pressure distribution on channel wall for all the fluxes and with grid#3 (241x131).....	90
4.50. The pressure distribution on channel wall for all the fluxes and with grid#4 (318x150).....	91
4.51. The supersonic wedge cascade geometry and boundary conditions.....	92
4.52. Analytical (Exact) Mach number distribution on the blade pressure and suction sides [34].....	93
4.53. Shock structure that is found by Analytical solution [34] .....	94
4.54. The Grid#1 for wedge cascade geometry .....	95
4.55. Mach number contour obtained by WENO HLLC scheme for CFL=0.2.....	96
4.56. Mach number contours obtained by WENO HLLC scheme for CFL=0.6 .....	96
4.57. Mach Number distributions on the wedge cascade walls for both CFL numbers	97
4.58. Convergence History graphs for WENO-HLLC scheme .....	98
4.59. Mach number contour obtained by WENO LF scheme for CFL=0.2 .....	99
4.60. Mach number contour obtained by WENO LF scheme for CFL=0.6 .....	99
4.61. Mach Number distributions on the wedge cascade walls for both CFL numbers	100
4.62. Convergence History graphs for WENO-LF scheme .....	101
4.63. Mach number contour obtained by WENO-MUSTA scheme for CFL=0.2..	102
4.64. Mach number contour obtained by WENO-MUSTA scheme for CFL=0.6..	102
4.65. Mach Number distributions on the wedge cascade walls for both CFL numbers	103
4.66. Convergence History graphs for WENO-MUSTA scheme.....	104
4.67. Mach number contour obtained by WENO-RUSANOV scheme CFL=0.2 .....	105
4.68. Mach number contour obtained by WENO-RUSANOV scheme CFL=0.6 .....	105
4.69. Mach number distributions on the wedge cascade walls both CFL numbers...	106

4.70. Convergence History graphs for WENO-LF flux.....	107
4.71. Comparison of the Mach number distribution of all the fluxes for grid#1 and for CFL=0.2 .....	108
4.72. Comparison of the Mach number distribution of all the fluxes for grid#1 and for CFL=0.6 .....	109
4.73. The Grid#2 for wedge cascade geometry .....	110
4.74. Mach number contour obtained by WENO-HLLC scheme .....	111
4.75. Mach number contour obtained by WENO-LF scheme .....	111
4.76. Mach number contour obtained by WENO-MUSTA scheme.....	112
4.77. Mach number contour obtained by WENO-RUSANOV scheme.....	112
4.78. Comparison of Mach Number distributions obtained by WENO-HLLC scheme for different grids .....	113
4.79. Comparison of Mach Number distributions obtained by WENO-LF scheme for different grids.....	114
4.80. Comparison of Mach Number distributions obtained by WENO-MUSTA scheme for different grids .....	115
4.81. Comparison of Mach number distributions obtained by WENO-RUSANOV scheme for different grids .....	116
4.82. Convergence History of the schemes.....	117
4.83. Comparison of Mach number distributions for all schemes for grid #2.....	118
A.1. Algorithm flow chart[28].....	130

## LIST OF SYMBOLS

$a$	Speed of sound
$c$	CFL coefficient
$C_{rj}$	Grid coefficient constant
$d_r$	Weighted averaging coefficient
$e$	Internal energy
$E$	Total energy
$f$	Flux vector in x-direction
$\hat{f}_{i+1/2, j}$	Numerical flux at the cell faces in x-direction
$g$	Flux vector in y-direction
$\hat{g}_{i, j+1/2}$	Numerical flux at the cell faces in y-direction
GQ	Gaussian quadrature
$h$	Inverse of Jacobian
$H$	Total enthalpy
$I_i$	Cell
$J$	Jacobian
$k$	Order of accuracy
$K1, K2$	Gaussian weights
$M$	Mach number
$n$	Normal unit vector
$N$	Number of cells

$p$	Pressure
$Q$	Flow property vector
$\bar{Q}$	Averaged flow property vector
$r$	Number of cells to the left
$R$	Eigenvectors
$R^{-1}$	Inverse of eigenvectors
$s$	Number of cells to the left
$S$	Entropy
$S_i$	Stencil
$t$	Time
$u$	Velocity in x-direction
$v$	Velocity in y-direction
$V_n$	Velocity normal component
$V_t$	Velocity tangential component
$x, y$	Cartesian Coordinates
$x_i, y_j$	Cell center
$\Delta x_i, \Delta y_j$	Cell sizes

### 3.1 Greek Symbols

$\rho$	Density
$\xi, \eta$	General Coordinates
$\omega_r$	Weights for WENO
$\beta_r$	Smooth indicators
$\gamma$	Specific heats ratio

$\lambda$	Eigenvalues
$\epsilon$	Vortex strength

### 3.2 Subscripts

RL	Roe averaged value
$\alpha$	Gaussian quadrature point
$\infty$	Free stream

### 3.3 Superscripts

r	Reconstructed value
---	---------------------

# CHAPTER 1

## INTRODUCTION

Nowadays, constructing high order accurate and robust schemes for simulation of compressible fluid flow has a growing interest. These are the schemes relied on interpolation of discrete data. The approximation theory constructs a basis for this interpolation. If smoothness of the function inside the interpolation stencil is provided, a wider interpolation stencil yields a higher order of accuracy.

Traditional higher order accurate schemes are relied on fixed stencil interpolations. To build second order interpolation polynomial; one should look one to the left and right cell boundaries and the center of the cell itself. Whereas, fixed stencil interpolation of second or higher order accuracy would have an oscillatory behaviour near a discontinuity. These oscillations are called as Gibbs Phenomena in spectral methods. [1]

All attempts are done to eliminate or reduce such oscillations near discontinuities. One of these attempts is to use explicit artificial viscosity. Artificial viscosity term is added to the solution to overcome these oscillations. However these artificial viscosity terms should damp the oscillations while maintaining the order of accuracy.

Another approach to eliminate or reduce the oscillations is to apply limiters. The spurious oscillations are eliminated or reduced by reducing the slope of a linear interpolant, or by using a linear rather than a quadratic interpolant near the shock. The importance of these schemes is to apply limiters carefully, so that TVD (total variation diminishing) property can be achieved for one dimensional nonlinear scalar problems or linear systems. One of the disadvantage of this method is the reduction of the order of accuracy of the interpolation near discontinuity. Therefore, by applying limiters, the

accuracy necessarily degenerates to first order near smooth extrema. The TVB (total variation bounded) modifications to the limiter in Shu [2] and Cockburn and Shu [3] are suggested to fix this disadvantage [4,5,1,6].

ENO (Essentially Non- Oscillatory ) scheme is the first succesful attempt to get a self similar , uniformly high order accurate , essentially non-oscillatory approximations to the smooth functions. The ENO schemes were first introduced by Harten, Engquist, Osher and Chakravarthy in 1987 [7]. In [7] Harten, Engquist, Osher and Chakravarthy searched for different ways of measuring the local smoothness. Once the local smoothness is measured, the local stencil can be determined. That constitutes a basis for the hierarchy that begins with one or two cells, then adds one cell left at a time to the stencil from the neighbours on the left and, right based on the size of two relevant Newton divided differences. However, there are other reasonable ways to select the stencil based on the local smoothness. One of them is to compare the magnitudes of the highest degree divided differences among all the neighbour stencils and picking the one with the least absolute value. The method proposed in [7] is the most robust for a wide range of grid sizes. ENO schemes are uniformly higher order accurate and resolve the shocks with sharp and monotone transitions. Also these schemes are suitable for the problems that are both containing shocks and complicated flow structures.

ENO scheme is uniformly higher order accurate right up to the discontinuity. This is achieved by adaptively choosing stencil based on the absolute values of divided differences. However , some remarks can be made for ENO scheme. First of all, the round of error perturbation near zeros of the solution and its derivatives can be changed by stencils . That is, propagation direction of stencil choosing procedure can be changed by this error. In the smooth regions, the free adaption of the stencil is not required. In addition this can cause loss of accuracy when applied to hyperbolic PDE [8] ENO scheme is computationally expensive because it contains many logical “if” structures in the stencil choosing procedure.

WENO (Weighted Essentially Non-Oscillatory) scheme is a more recent attempt to improve upon ENO in these points. The basic idea is to use a convex combination of all candidate stencils to form the reconstruction instead of using only one of them. Each candidate stencil is assigned a weight. That weight determines the contribution of the stencil to the final approximation. The stencil which is near discontinuity would have the smallest weight while the stencil which is far away from the discontinuity would have the biggest weight. Weighted ENO schemes were first introduced by Liu, Osher and Chan [9].

Two approaches are commonly used to formulate WENO scheme. These are finite difference and finite volume formulations. The finite difference version based on the point values while the finite volume version based on the cell averages. That is, the finite difference WENO scheme approximates the numerical fluxes at the points while the finite volume WENO scheme approximates the flow variables at the cell centers, and then calculates the numerical fluxes. Jiang and Shu [10] developed multi dimensional finite difference WENO scheme with improved accuracy. Also, Balsara and Shu have efficiently implemented finite difference WENO scheme in their work [11]. Friedrichs [12] applied WENO with multi dimensional finite volume formulation and also, Hu and Shu [13,14] applied WENO with multi dimensional finite volume formulation with improved accuracy. Levy, Puppo and Russo [15] used WENO scheme for 1-D finite volume based on a staggered grid and Lax-Friedrichs formulation. Besides the structured grid, Weighted ENO schemes can be applied to the unstructured meshes. Hu and Shu [13,14] also presented third and fourth order WENO reconstruction in their work. A lower order reconstruction procedure can be found in [16]. Another work for unstructured WENO scheme is done by Shi, Hu and Shu in [17].

In this thesis, the finite volume formulation of WENO scheme is used because it can be applied with arbitrary meshes provided that WENO reconstruction is available. Finite difference formulation has some drawbacks in application to arbitrary meshes. To apply finite difference formulations, the domain should be predominantly rectangle or smoothly mapped to a rectangle. If the domain aspect ratio is disproportionate the transformation parameters can disturb the order of accuracy. Therefore, It is more

convenient to use finite volume formulations. The formulations are done for structured meshes because it is easier to apply WENO reconstruction on structured meshes compared with unstructured meshes. In Unstructured meshes, it is very hard to find propagation direction. Also reconstruction procedure for unstructured meshes is more expensive than structured meshes. For example for third order reconstruction, one should use the information of neighbour cells and neighbours of neighbour cells. That is, for 3<sup>rd</sup> order reconstruction 10 cells should be used. Whereas in structured meshes for 3<sup>rd</sup> order reconstruction only five cells are used.

In two space directions the flux computation in WENO schemes involves the use of a high-order Gaussian quadrature for integration over cell sides. WENO reconstructed values are needed for each Gaussian integration point. More information about the Gaussian integration can be found in the work of Toro and Titarev [18]. The Gaussian integration is also used in this thesis.

After Reconstructed flow variables are obtained by Finite Volume WENO scheme, the final step is to calculation of fluxes with building block algorithms. This thesis proposes to use different fluxes as building block in WENO scheme. The first flux is the HLLC flux which is an approximate riemann solver. The HLLC does not use linearizations of the equations and works well for the low density problems and sonic points without any fixes. References [19,20] give detailed information about the HLLC type Riemann solver. The second flux is the Rusanov flux [20, 21]. Rusanov flux is a first order upwind flux and a basic approximate riemann solver. The third flux is the Lax-Friedrichs flux. The Lax-Friedrichs solution is weighted average of the solution of the riemann problem with the left and right neighbours states as data. It is an upwind biased scheme. References [20,22,23] give detailed information about Lax-Friedrichs scheme. The last flux is the Upwind Multi-Stage (MUSTA) flux. This family of fluxes successes upwinding by solving the local riemann problem at the cell interface numerically rather than analytically by means of simple and computationally inexpensive first-order centred method. References [18,24,25,26] give detailed information about MUSTA scheme.

In this thesis these different fluxes are used in WENO scheme with different mesh sizes. Then these schemes are compared in accuracy. All of the fluxes are tested in same boundary conditions and time discretization.

In METU, Department of Aerospace Engineering, there has been two thesis addressing WENO schemes. One of them is done by Ebru Sarıgöl [27] on WENO schemes with finite difference formulations. The other work is done by Monier EL-Farra [28] on WENO schemes with finite volume formulations. He has applied WENO schemes on test case problems and tested uniform and non uniform grid coefficients.

Although there are studies that investigate the different flux algorithms on weno scheme, all of these works are done on rectangular or non-complicated domains. The significance of this thesis is that it is the first study that employs different fluxes in WENO schemes on complicated geometries with different size of meshes, such as turbomachinery cascade geometries, non-rectangular geometries... This would help to solve complicated problems with higher order of accuracy without numerical oscillations.

The progress of this study includes the modification of finite difference WENO code and application of the code to the complicated geometries, generation of two-dimensional finite volume WENO code and application of it to the complicated geometries, and using different fluxes in formulation of WENO schemes.

First of all, the finite difference WENO code that is supplied by Shu [1] is modified to apply non-rectangular geometries. This modification is done by adding transformation matrices to the original code. Then this code is applied to the complex geometric problems. However, It is concluded that insertion of transformation matrices brings some errors to the solution. So that the solutions obtained are not in the desired order of accuracy. Therefore, a two dimensional finite volume WENO code is developed by Monier El-Farra and the present author. That code is applied to the complicated geometries and provided us desired order of accuracy. Then, different fluxes are applied to the algorithm to see the effect of fluxes on complex geometries in this thesis.

The rest of this thesis is organized as follows. In Chapter 2 , Euler equation and the general semi-discrete WENO reconstruction procedure are described. In Chapter 3, The numerical fluxes and boundary conditions are explained. In Chapter 4, five different test case problems and the solutions of these problems are described. These are Shock tube problem in one-dimension, also in two dimensions Double Mach Reflection problem, channel flow problem, and wedge cascade problems. Finally Chapter 5 includes discussion and conclusion of the study.

## CHAPTER 2

### 2-D EULER EQUATIONS AND WENO DISCRETIZATION

#### 2.1. Governing Equations

The two-dimensional Euler equations are expressed as;

$$\text{(Continuity)} \quad \frac{\partial}{\partial t}(\rho) + \frac{\partial}{\partial x}(\rho u) + \frac{\partial}{\partial y}(\rho v) = 0 \quad (2.1)$$

$$\text{(x - Momentum)} \quad \frac{\partial}{\partial t}(\rho u) + \frac{\partial}{\partial x}(\rho u^2 + p) + \frac{\partial}{\partial y}(\rho uv) = 0 \quad (2.2)$$

$$\text{(y - Momentum)} \quad \frac{\partial}{\partial t}(\rho v) + \frac{\partial}{\partial x}(\rho uv) + \frac{\partial}{\partial y}(\rho v^2 + p) = 0 \quad (2.3)$$

$$\text{(Energy)} \quad \frac{\partial}{\partial t}(\rho E) + \frac{\partial}{\partial x}(\rho Eu + pu) + \frac{\partial}{\partial y}(\rho Ev + pv) = 0 \quad (2.4)$$

Where  $v$  is the y-velocity

Equations (2.1) through (2.4) are expressed in flux vector form as

$$\frac{\partial Q}{\partial t} + \frac{\partial f}{\partial x} + \frac{\partial g}{\partial y} = 0 \quad (2.5)$$

where

$$Q = \begin{bmatrix} \rho \\ \rho u \\ \rho v \\ \rho E \end{bmatrix}, \quad f = \begin{bmatrix} \rho u \\ \rho u^2 + p \\ \rho uv \\ (\rho E + p)u \end{bmatrix}, \quad \text{and} \quad g = \begin{bmatrix} \rho v \\ \rho uv \\ \rho v^2 + p \\ (\rho E + p)v \end{bmatrix} \text{ is the y-flux}$$

## 2.2. Finite Volume Formulation in Two Space Dimensions

Consider two-dimensional hyperbolic systems in conservation form

$$\frac{\partial Q}{\partial t} + \frac{\partial f}{\partial x} + \frac{\partial g}{\partial y} = 0$$

Where  $Q(x,y,t)$  is the vector of unknown conservative variables and  $f(Q)$  and  $g(Q)$  are physical flux vectors in  $x$  and  $y$  coordinate directions respectively. The semi-discrete finite volume methods begin by considering a control volume  $I_{ij}$  in  $x$ - $y$  space

$$I_{ij} = [x_{i-1/2}, x_{i+1/2}] \times [y_{j-1/2}, y_{j+1/2}] \quad 1 \leq i \leq N_x, \quad 1 \leq j \leq N_y \quad (2.6)$$

And the grid sizes are given by

$$\Delta x_i = x_{i+1/2} - x_{i-1/2} \quad i = 1, 2, \dots, N_x \quad (2.7)$$

$$\Delta y_j = y_{j+1/2} - y_{j-1/2} \quad j = 1, 2, \dots, N_y$$

Integrating 2.5 over the control  $I_{ij}$ , we obtain the following semi-discrete relations

$$\frac{dQ_{ij}(t)}{dt} = -\frac{1}{\Delta x} \left( f_{i+1/2,j} - f_{i-1/2,j} \right) - \frac{1}{\Delta y} \left( g_{i,j+1/2} - g_{i,j-1/2} \right) \quad (2.8)$$

Where  $Q_{ij}(t)$  is the space average of the solution in cell  $I_{ij}$  at time  $t$

$$Q_{ij}(t) \equiv \frac{1}{\Delta x_i \Delta y_j} \int_{y_{j-1/2}}^{y_{j+1/2}} \int_{x_{i-1/2}}^{x_{i+1/2}} Q(\xi, \eta, t) d\xi d\eta \quad (2.9)$$

And  $f_{i+1/2,j}$  and  $g_{i,j+1/2}$  are space averages of physical fluxes over cell faces at time  $t$ :

$$f_{i+1/2,j}(t) \equiv \frac{1}{\Delta y} \int_{y_{j-1/2}}^{y_{j+1/2}} f(Q(x_{i+1/2}, y)) dy \quad (2.10)$$

$$g_{i+1/2,j}(t) \equiv \frac{1}{\Delta x} \int_{x_{i-1/2}}^{x_{i+1/2}} f(Q(x, y_{j+1/2})) dx$$

Expressions 2.9 and 2.10 are so far exact relations, but can also be used in construction of higher order accurate semi-discrete schemes if  $Q_{ij}(t)$ ,  $f_{ij}$  and  $g_{ij}$  are regarded as numerical approximations to the corresponding exact quantities.

The first step to discretize the integrals over the faces using suitable Gaussian numerical quadrature .

$$\hat{f}_{i+1/2,j} = \frac{1}{\Delta y} \sum_{\alpha=1}^N f(Q(x_{i+1/2}, y_{\alpha})) \omega_{\alpha} \quad (2.11)$$

Where the subscript  $\alpha$  correspond to different Gaussian integration points and weights  $K_{\alpha}$ . Expression 2.11 involves point-wise values of  $Q$  whereas the scheme evolves the cell averages of  $Q$ . Thus the second step in evaluating the fluxes is to reconstruct the point-wise values of the solution from the cell averages and obtain high-order accurate approximations to the values of the at the integration points. In WENO schemes this is achieved by means of weighted essentially non-oscillatory (WENO) adaptive-stencil reconstruction procedure which estimates the smoothness of the solution and constructs the reconstruction polynomial in such a way so as to avoid interpolation across discontinuities. After reconstruction is carried out at each face we have two sets of values of  $Q$ , corresponding to  $x_{i+1/2} - 0$  and  $x_{i+1/2} + 0$  which often called minus and plus boundary extrapolated values.

$$\begin{aligned} Q_{i+1/2,\alpha}^- &= Q(x_{i+1/2} - 0, y_\alpha) \\ Q_{i+1/2,\alpha}^+ &= Q(x_{i+1/2} + 0, y_\alpha) \end{aligned} \quad (2.12)$$

And the numerical fluxes given as;

$$\hat{f}_{i+1/2,j} = \sum_{\alpha} \omega_{\alpha} h(Q_{i+1/2,y_j+\beta_{\alpha}\Delta y}^-, Q_{i+1/2,y_j+\beta_{\alpha}\Delta y}^+) \quad (2.13)$$

$$\hat{g}_{i,j+1/2} = \sum_{\alpha} \omega_{\alpha} h(Q_{x_i+\beta_{\alpha}\Delta x,j+1/2}^-, Q_{x_i+\beta_{\alpha}\Delta x,j+1/2}^+) \quad (2.14)$$

$h$  in (2.13) and (2.14) is the one-dimensional monotone flux .

### 2.3. WENO Reconstruction in Two Space Dimensions

The Reconstruction problem we face is the following. Given spatial averages of a scalar function  $q(x, y)$  in a cell  $I_{ij}$  ;

$$q_{ij} \equiv \frac{1}{\Delta x \Delta y} \int_{y_{j-1/2}}^{y_{j+1/2}} \int_{x_{i-1/2}}^{x_{i+1/2}} q(x, y) dy dx \quad (2.15)$$

The point-wise value of  $q$  at Gaussian integration points  $(x_{i+1/2}, y_{\alpha})$  is going to be computed so that the reconstruction procedure is conservative and these reconstructed values are of higher order of accuracy. The way to accomplish this is to use dimension by dimension reconstruction. Dimension by dimension reconstruction consists of a number of one-dimensional reconstruction sweeps. The dimension-by-dimension reconstruction is more simpler and less computationally expensive than other reconstruction methods so that in this thesis the dimension-by dimension reconstruction method will be used throughout.

The left  $Q_{i+1/2,y_{\alpha}}^-$  and right  $Q_{i+1/2,y_{\alpha}}^+$  extrapolated values are needed. For the left values, the stencil consists of cells  $I_{ij}$  such that;

$$i-k \leq i \leq i+k \quad , \quad j-k \leq j \leq j+k \quad (2.16)$$

For the right values, the stencil consists of cells for which  $i+1-k \leq i \leq i+1+k$  and  $j$  varies according to (2.16).

The reconstruction for 2-D consists of two steps:

In the first step, one-dimensional WENO reconstruction in  $x$  coordinate direction for all values of  $j$  with respect to  $y$  coordinate direction is performed.

$$w_{i+1/2,j}^+ = \frac{1}{\Delta y_j} \int_{y_{j-1/2}}^{y_{j+1/2}} v^+(x_{i+1/2}, y) dy \quad (2.17)$$

$$w_{i+1/2,j}^- = \frac{1}{\Delta y_j} \int_{y_{j-1/2}}^{y_{j+1/2}} v^-(x_{i+1/2}, y) dy$$

In the second step, reconstructed values  $v_{i+1/2,y_\alpha}^\pm$  are obtained by applying one-dimensional reconstruction to  $w_{i+1/2,j}^\pm$  in the  $y$  coordinate direction.

In the second step (the  $y$ -sweep) the weights are designed to achieve high accuracy for Gaussian integration point  $y_\alpha$ ; the values of these weights are tailored to a specific Gaussian integration rule used to discretize (2.13). The numerical experiments in [18] show that the best results in terms of accuracy and computational cost for 3<sup>rd</sup> and 4<sup>th</sup> order WENO reconstruction are obtained if the following two-point (forth order) Gaussian quadrature is used:

$$\int_{-1}^1 \varphi(\xi) d\xi = \varphi\left(\frac{-1}{\sqrt{3}}\right) + \varphi\left(\frac{1}{\sqrt{3}}\right) \quad (2.18)$$

The WENO sweep in the  $x$  coordinate direction corresponds to the left and right reconstructed values at  $x_{i+1/2}$  whereas the  $y$ -sweep needs values at the Gaussian points  $y_\alpha$ , for the two-point quadrature (2.18) those are  $\xi_i \pm \Delta\xi(2\sqrt{3})$ . It appears that the weights and reconstruction formulas for the Gaussian integration points  $y_\alpha$  have not reported in the literature so far. However, [21] gave explicit formulas and weights for the two-point Gaussian integration for 3<sup>rd</sup> and 4<sup>th</sup> order WENO reconstruction which we use in this thesis.

## 2.4. One – Dimensional WENO Reconstruction

Before explaining the WENO reconstruction, it is worth to consider the reconstruction for finite volume schemes in general.

### 2.4.1. Reconstruction from Cell Averages

The first approximating problem in solving hyperbolic conservation laws using cell averages (finite volume schemes) is the following reconstruction problem [1] .

Given the cell averages of a function  $v(x)$

$$\bar{v}_i = \frac{1}{\Delta x_i} \int_{x_{i-1/2}}^{x_{i+1/2}} v(\xi) d\xi \quad i = 1, 2, \dots, N \quad (2.19)$$

in which the computational domain is defined as  $a < x < b$  and the grid is defined by

$$a < x_{\frac{1}{2}} < x_{\frac{3}{2}} < \dots < x_{\frac{N-1}{2}} < x_{\frac{N+1}{2}} < b \quad (2.20)$$

The cells, cell centers, and cell sizes are defined by

$$I_i \equiv \left[ x_{i-\frac{1}{2}}, x_{i+\frac{1}{2}} \right], \quad x_i \equiv \frac{1}{2} \left( x_{i-\frac{1}{2}} + x_{i+\frac{1}{2}} \right), \quad (2.21)$$

$$\Delta x_i \equiv x_{i+\frac{1}{2}} - x_{i-\frac{1}{2}}, \quad i = 1, 2, \dots, N.$$

where  $N$  is the number of cells

One wants to find a polynomial  $p_i(x)$  of degree at most  $k-1$ , for each  $I_i$ , such that it is a  $k^{\text{th}}$  order accurate approximation to the function  $v(x)$  inside  $I_i$

$$p_i(x) = v(x) + O(\Delta x^k), \quad x \in I_i, \quad i = 1, \dots, N \quad (2.22)$$

In particular, this gives approximation to the function  $v(x)$  at the cell boundaries

$$v_{i+1/2}^- = p_i(x_{i+1/2}) \quad , \quad v_{i-1/2}^+ = p_i(x_{i-1/2}) \quad , \quad i = 1, \dots, N \quad (2.23)$$

which are  $k^{th}$  order accurate.

To solve the above problem, the following procedure is described:

Given the location  $I_i$  and the order of accuracy  $k$ , we first choose a stencil

$$\{S(i)\}$$

$$S(i) \equiv \{I_{i-r}, \dots, I_{i+s}\} \quad , \quad r, s \geq 0 \quad (2.24)$$

where  $r$  is the number of cells to the left,  $s$  is the number of cells to the right with

$$r + s + 1 = k .$$

There is a unique polynomial of degree at most  $k - 1 = r + s$ , denoted by  $p(x)$  (the subscript  $i$  is removed when there is no confusion), whose cell average in each of the cells in the stencil  $S(i)$  agrees with that of  $v(x)$

$$\frac{1}{\Delta x_j} \int_{x_{j-1/2}}^{x_{j+1/2}} p(\xi) d\xi = \bar{v}_j \quad , \quad j = i - r, \dots, i + s \quad (2.25)$$

This unique polynomial  $p(x)$  is the  $k^{th}$  order approximation we are looking for.

Another consideration for solving the previous problem is that, approximations to the values of  $v(x)$  at the cell boundaries (2.23) are also needed. Since the mappings from the given cell averages  $\bar{v}_j$  in the stencil  $S(i)$  to the values  $v_{i+1/2}^-$ ,  $v_{i-1/2}^+$  in (2.23) are linear, there exist constants  $C_{rj}$  and  $\tilde{C}_{rj}$ , which depend on the left shift  $r$  of the stencil  $S(i)$  in (2.24), on the order of accuracy  $k$ , and on the cell sizes  $\Delta x_j$  in the stencil, but not on the function  $v$  itself.

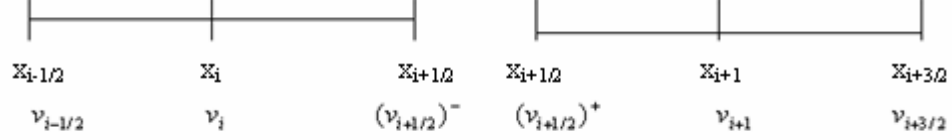
This relation is such that:

$$v_{i+1/2}^- = \sum_{j=0}^{k-1} C_{rj} \bar{v}_{i-r+j} \quad , \quad v_{i-1/2}^+ = \sum_{j=0}^{k-1} \tilde{C}_{rj} \bar{v}_{i-r+j} \quad (2.26)$$

with  $\tilde{C}_{rj} = C_{r-1,j}$

The difference between the values with  $\pm$  superscripts at the same location ( $x_{i+1/2}$  or  $x_{i-1/2}$ ) is due to the possibility of different stencils for cell  $I_i$  and cell  $I_{i+1}$ .

This difference is explained in the sketch below



So at location ( $x_{i+1/2}$ ),  $v_{i+1/2}$  for cell  $I_i$  has a (-) superscript and at the same location it has a (+) superscript for cell  $I_{i+1}$  and so on. If the left shift  $r$  is identified with the point of reconstruction  $x_{i+1/2}$  not with the cell  $I_i$  itself, then the  $\pm$  superscripts can be dropped.

The  $C_{rj}$  constants are given in [1] as:

$$C_{rj} = \left( \frac{\sum_{l=0}^k \prod_{\substack{q=0 \\ l \neq m, q \neq m, l}}^k \left( x_{i+\frac{1}{2}} - x_{i-r+q-\frac{1}{2}} \right)}{\prod_{\substack{l=0 \\ l \neq m}}^k \left( x_{i-r+m-\frac{1}{2}} - x_{i-r+l-\frac{1}{2}} \right)} \right) \Delta x_{i-r+j}. \quad (2.27)$$

The  $C_{rj}$  constants are related to the grid that is why they are referred to as grid coefficients. Equation (2.27) is used to evaluate the grid coefficients ( $C_{rj}$  constants) for any grid (uniform and non-uniform). However, for uniform grids, since  $\Delta x_i = \Delta x =$  constant,  $C_{rj}$  doesn't depend on  $i$  or  $\Delta x$  any more. So equation (2.27) reduces to:

$$C_{rj} = \sum_{m=j+1}^k \frac{\sum_{l=0}^k \prod_{\substack{q=0 \\ q \neq m, l}}^k (r-q+1)}{\prod_{l=0}^k (m-l)} \quad (2.28)$$

Values for  $C_{rj}$  constants are listed in Table (2.1) for order of accuracy between 1 and 7 [1].

Now as a summary for this section:

$$\bar{v}_{i-r}, \dots, \bar{v}_{i-r+k-1} \quad (\text{Notice that } k-r = s+1)$$

There are grid coefficients ( $C_{rj}$  constants) such that the reconstructed values at the cell boundary  $x_{i+1/2}$

$$v_{i+1/2} = \sum_{j=0}^{k-1} C_{rj} \bar{v}_{i-r+j} \quad (2.29)$$

is the  $k^{\text{th}}$  order accurate:

$$v_{i+1/2} = v(x_{i+1/2}) + O(\Delta x^k) \quad (2.30)$$

If the left shift  $r$  in (2.24) is the same for all locations  $i$ , then the stencil is fixed. For a globally smooth function  $v(x)$ , the best approximation is usually obtained either by a central approximation  $r = s-1$  for even  $k$  or by a one point upwind biased approximation  $r = s$  or  $r = s-2$  for odd  $k$  [1].

## 2.5. WENO Approximations in 1-D (In Scalar Case)

For solving hyperbolic conservation laws, one is interested in the class of piecewise smooth functions. A piecewise smooth function  $v(x)$  is smooth except at finitely many isolated points. At these points,  $v(x)$  and its derivatives are assumed to have finite left and right limits.

If the function  $v(x)$  is only piecewise smooth, a fixed stencil approximation described in the previous section may not be adequate near discontinuities and it may lead to oscillations. These oscillations happen because the stencils contain the discontinuous cell for  $x_i$  close enough to the discontinuity. As a result the

approximation property (2.22) is no longer valid in such stencils. From her the idea of choosing an adaptive stencil among the candidate stencils to form the reconstruction has arose and led to the Essentially Non-Oscillatory ENO scheme which has been modified later to produce the weighted ENO (WENO) schemes.

**Table 2-1.** The  $C_{rj}$  constants [1].

k	r	j=0	j=1	j=2	j=3	j=4	j=5	j=6
1	-1	1						
	0	1						
2	-1	3/2	-1/2					
	0	1/2	1/2					
	1	-1/2	3/2					
3	-1	11/6	-7/6	1/3				
	0	1/3	5/6	-1/6				
	1	-1/6	5/6	1/3				
	2	1/3	-7/6	11/6				
4	-1	25/12	-23/12	13/12	-1/4			
	0	1/4	13/12	-5/12	1/12			
	1	-1/12	7/12	7/12	-1/12			
	2	1/12	-5/12	13/12	1/4			
	3	-1/4	13/12	-23/12	25/12			
5	-1	137/60	-163/60	137/60	-21/20	1/5		
	0	1/5	77/60	-43/60	17/60	-1/20		
	1	-1/20	9/20	47/60	-13/60	1/30		
	2	1/30	-13/60	47/60	9/20	-1/20		
	3	-1/20	17/60	-43/60	77/60	1/5		
	4	1/5	-21/20	137/60	-163/60	137/60		
6	-1	49/20	-71/20	79/20	-163/60	31/30	-1/6	
	0	1/6	29/20	-21/20	37/60	-13/60	1/30	
	1	-1/30	11/30	19/20	-23/60	7/60	-1/60	
	2	1/60	-2/15	37/60	37/60	-2/15	1/60	
	3	-1/60	7/60	-23/60	19/20	11/30	-1/30	
	4	1/30	-13/60	37/60	-21/20	29/20	1/6	
	5	-1/6	31/30	-163/60	79/20	-71/20	49/20	
7	-1	363/140	-617/140	853/140	-2341/420	667/210	-43/42	1/7
	0	1/4	223/140	-197/140	153/140	-241/420	37/210	-1/42
	1	-1/42	13/42	153/140	-241/420	109/420	-31/420	1/105
	2	1/105	-19/210	107/210	319/420	-101/420	5/84	-1/140
	3	-1/140	5/84	-101/420	319/420	107/210	-19/210	1/105
	4	1/105	-31/420	109/420	-241/420	153/140	13/42	-1/42
	5	-1/42	37/210	-241/420	153/140	-197/140	223/140	1/7
	6	1/7	-43/42	667/210	-2341/420	853/140	-617/140	363/140

WENO [9,10] is based on ENO and it is a trial to improve upon ENO in the mentioned remarks about ENO. The basic idea of WENO is to use a convex combination of all of the candidate stencils instead of using only one of them (as in ENO).

Suppose the  $k$  candidate stencils are:

$$S_r(i) = \{x_{i-r}, \dots, x_{i-r+k-1}\}, \quad r = 0, \dots, k-1 \quad (2.31)$$

Those stencils produce  $k$  different reconstructions to the value  $v_{i+1/2}$ .

According to (2.29)

$$v_{i+1/2}^{(r)} = \sum_{j=0}^{k-1} C_{rj} \bar{v}_{i-r+j}, \quad r = 0, \dots, k-1 \quad (2.32)$$

WENO reconstruction would take a convex combination of all  $v_{i+1/2}^{(r)}$  defined in (2.32) as a new approximation to the cell boundary value  $v(x_{i+1/2})$

$$v_{i+1/2} = \sum_{r=0}^{k-1} \omega_r v_{i+1/2}^{(r)} \quad (2.33)$$

It should be clear that the key to the success of WENO would be the choice of the weights  $\omega_r$ .

For consistency, it is required that

$$\omega_r \geq 0, \quad \sum_{r=0}^{k-1} \omega_r = 1 \quad (2.34)$$

To understand (2.34), one should remember the fixed stencil approximation. In the fixed stencil approximation only one stencil is used everywhere in the solution domain. This approximation assuming that this stencil contributes 100% to the solution so as if this stencil is multiplied by one. For the WENO case, there are more than one stencil used, each one of them contributes with some amount, which can't be negative, and also the total contribution should be 100% (or one). These weights determine the

amount of contribution of each stencil. As a result, none of them is negative and their summation is one (i.e., (2.24)).

If the function  $v(x)$  is smooth in all of the candidate stencils (2.31), there are constants  $d_r$  such that

$$v_{i+1/2} = \sum_{r=0}^{k-1} d_r v_{i+1/2}^{(r)} = v(x_{i+1/2}) + O(\Delta x^{2k-1}) \quad (2.35)$$

It is noticed that  $d_r$  is always positive and due to consistency (as explained for  $\omega_r$ )

$$\sum_{r=0}^{k-1} d_r = 1 \quad (2.36)$$

The order of accuracy in (2.35) expected to be  $(2k-1)$  in smooth regions because for the  $k$  stencils contain  $(2k-1)$  cells so it is  $(2k-1)^{th}$  order.

In this smooth case, to keep the order of accuracy  $(2k-1)$ , then  $\omega_r$  should be

$$\omega_r = d_r + O(\Delta x^{k-1}) \quad , \quad r = 0, \dots, k-1 \quad (2.37)$$

So

$$\begin{aligned} \sum_{r=0}^{k-1} \omega_r v_{i+1/2}^{(r)} - \sum_{r=0}^{k-1} d_r v_{i+1/2}^{(r)} &= \sum_{r=0}^{k-1} (\omega_r - d_r) (v_{i+1/2}^{(r)} - v(x_{i+1/2})) \\ &= \sum_{r=0}^{k-1} O(\Delta x^{k-1}) O(\Delta x^k) = O(\Delta x^{2k-1}) \end{aligned} \quad (2.38)$$

Which would imply  $(2k-1)^{th}$  order of accuracy

$$v_{i+1/2} = \sum_{r=0}^{k-1} \omega_r v_{i+1/2}^{(r)} = v(x_{i+1/2}) + O(\Delta x^{2k-1}) \quad (2.39)$$

The form of the weights is based on the following considerations:

When the function  $v(x)$  has a discontinuity in one or more of the stencils (2.31), the corresponding weights  $\omega_r$  should essentially be zero, which implies that there is no contribution for the stencils that contain discontinuity.

A final consideration, the weights should be computationally efficient. Thus, polynomials or rational functions are preferred over exponential type functions.

Considering the three remarks above, the following form of the weights came into picture [10].

$$\omega_r = \frac{\alpha_r}{\sum_{s=0}^{k-1} \alpha_s}, \quad r = 0, \dots, k-1 \quad (2.40)$$

where

$$\alpha_r = \frac{d_r}{(\epsilon + \beta_r)^2} \quad (2.41)$$

$\epsilon$  here is a small number always greater than zero which is introduced to avoid the denominator to become zero. We take  $\epsilon = 10^{-6}$  throughout our numerical calculations.

$\beta_r$ 's are the smooth indicators of the stencil  $S_r(i)$ .  $\beta_r$  is used in calculation of weights and it constructs weights such that the discontinuity is avoided inside the stencil.

After extensive experiments, a robust choice of smooth indicators is obtained [10]

$$\beta_r = \sum_{l=1}^{k-1} \int_{x_{i-\frac{1}{2}}}^{x_{i+\frac{1}{2}}} \Delta x^{2l-1} \left( \frac{\partial^l p_r(x)}{\partial^l x} \right)^2 dx \quad (2.42)$$

where  $p_r(x)$  is the reconstruction polynomial on the stencil  $S_r(i)$  (Lagrange Polynomial).

As an example, for  $k = 3$ , (2.42) gives the following smoothness indicators [10]

$$\begin{aligned}
\beta_0 &= \frac{13}{12}(\bar{v}_i - 2\bar{v}_{i+1} + \bar{v}_{i+2})^2 + \frac{1}{4}(3\bar{v}_i - 4\bar{v}_{i+1} + \bar{v}_{i+2})^2 \\
\beta_1 &= \frac{13}{12}(\bar{v}_{i-1} - 2\bar{v}_i + \bar{v}_{i+1})^2 + \frac{1}{4}(\bar{v}_{i-1} - \bar{v}_{i+1})^2 \\
\beta_2 &= \frac{13}{12}(\bar{v}_{i-2} - 2\bar{v}_{i-1} + \bar{v}_i)^2 + \frac{1}{4}(\bar{v}_{i-2} - 4\bar{v}_{i-1} + 3\bar{v}_i)^2
\end{aligned} \tag{2.43}$$

Since the order of WENO scheme is  $(2k - 1)^{th}$ , equation (2.43) gives a fifth order scheme.

It is worth to summarize this section (the WENO reconstruction for the scalar case) in the following procedure:

Given the cell averages  $\{\bar{v}_i\}$  of a function  $v(x)$ , for each  $I_i$  we obtain  $(2k - 1)^{th}$  order approximation to the function  $v(x)$  at the cell boundary  $v_{i+1/2}^-$ ,  $v_{i-1/2}^+$  in the following steps:

Obtain the  $k$  reconstructed values  $v_{i+1/2}^{(r)}$  of  $k^{th}$  order accuracy in (2.32) based on the stencils  $S_r(i)$  in (2.31) for  $r = 0, \dots, k - 1$ . Also obtain the  $k$  reconstructed values  $v_{i-1/2}^{(r)}$  of  $k^{th}$  order accuracy using (2.26), again based on the stencils (2.31) for  $r = 0, \dots, k - 1$ .

Find the constants  $d_r$  such that (2.35) and

$$v_{i-1/2} = \sum_{r=0}^{k-1} \tilde{d}_r v_{i-1/2}^{(r)} = v(x_{i-1/2}) + O(\Delta x^{2k-1})$$

For example for  $k=3$  case,  $(2k-1)=5$  candidate cells should be used. Three stencils, each containing three cells, are formed. That can easily be seen on figure 2.1.

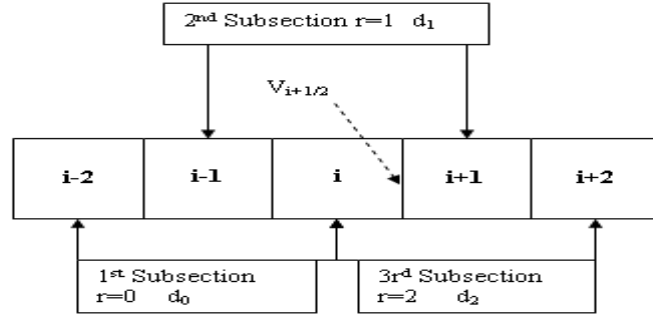


**Figure 2.1.** Explanation of weights and stencil choosing process for  $v_{i+1/2}$

By symmetry  $\tilde{d}_r = d_{k-1-r}$ , Also for  $k=3$  the weights  $\tilde{d}$  can be seen at figure 2.2

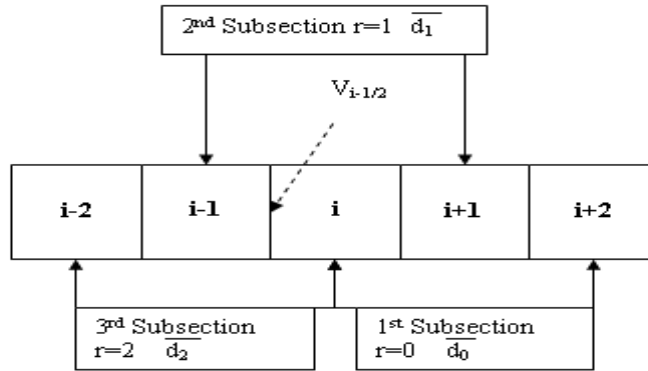


**Figure 2.2.** Explanation of weights and stencil choosing process for  $v_{i-1/2}$

Find the smooth indicators  $\beta_r$  in (2.42) for all  $r = 0, \dots, k-1$ .

Form the weights  $\omega_r$  and  $\tilde{\omega}_r$  using (2.40), (2.41) and

$$\tilde{\omega}_r = \frac{\tilde{\alpha}_r}{\sum_{s=0}^{k-1} \tilde{\alpha}_s}, \quad \tilde{\alpha}_r = \frac{\tilde{d}_r}{(\epsilon + \beta_r)^2}, \quad r = 0, \dots, k-1 \quad (2.44)$$

Find the  $(2k - 1)^{th}$  order reconstruction

$$v_{i+1/2}^- = \sum_{r=0}^{k-1} \omega_r v_{i+1/2}^{(r)} \quad , \quad v_{i-1/2}^+ = \sum_{r=0}^{k-1} \tilde{\omega}_r \bar{v}_{i-1/2}^{(r)} \quad (2.45)$$

## 2.6. Characteristic -wise FV WENO Reconstruction

As mentioned before, the finite volume WENO reconstruction is used for evaluating the left and right flow variables  $Q_{i+1/2}^\pm$  at the cell boundary  $(x_{i+1/2})$ . Those values are important for solving equations (2.13 and 2.14) and finding the flux at the cell interface i.e.,  $\hat{f}_{i+1/2}$ .

Before carrying out the WENO reconstruction, it is worth to mention that there are mainly two types of WENO reconstruction for system of equations. The component-wise and the characteristic-wise WENO reconstruction types. It is easier to apply WENO scheme in a component-by-component fashion. In the finite volume case this means that the reconstruction is made using WENO for each component of  $Q$  separately to obtain  $Q_{i+1/2}^\pm$ . The component-by-component version of WENO is simple and cost effective. It works well for many problems especially when the order of accuracy is not high (2<sup>nd</sup> or sometimes 3<sup>rd</sup>). However, for more demanding test problems, or when the order of accuracy is high, this method doesn't work well. Instead a more costly but much more robust characteristic decomposition is needed. In this work, only the characteristic – wise version is implemented.

The characteristic – wise FV WENO scheme is explained in upcoming procedure: Given the cell averages for the flow variables  $\bar{Q}$  for all  $i$ , at each fixed  $x_{i+1/2}$  we do the following:

Compute the average state  $Q_{i+1/2}$  using Roe averaging method.

Compute the right eigenvectors  $R$ , left eigenvectors  $R^{-1}$ , and the eigenvalues  $\lambda$  's of the Jacobian matrix  $f'(Q_{i+1/2})$ . The left eigenvectors are useful in transforming the flow properties (or the physical variables) into the characteristic variables, where the right eigenvectors are used in transforming back into the physical space.

Transform all the given cell averages which are in the physical space into characteristic variables using the left eigenvectors.

$$\bar{v}_j = R^{-1}(Q_{i+1/2})\bar{Q}_j \quad , \quad j \text{ in a neighborhood of } i$$

Perform the WENO reconstruction procedure for each component of the characteristic variables  $\bar{v}_j$  obtained in (c) to get the corresponding component of the reconstruction  $v_{i+1/2}^\pm$ .

Transform back into the physical space using the right eigenvectors. After obtaining  $v_{i+1/2}^\pm$  from WENO reconstruction, those characteristic variables are transformed into physical space by utilizing the right eigenvectors.

$$Q_{i+1/2}^\pm = Rv_{i+1/2}^\pm$$

Now these variables are the ones to be used in the flux calculation.

2- Finally, apply an exact or approximate Riemann solver to compute the flux at the cell interface  $\hat{f}_{i+1/2}$  for all  $i$  in (2.13 and 2.14) then form the scheme (2.8).

## 2.7. Application of Piece-wise Parabolic WENO Approximation

In this section the fifth order characteristic-wise finite volume WENO scheme is going to be applied to calculate the fluxes  $\hat{f}_{i+1/2,j}$  and  $\hat{g}_{i,j+1/2}$  in (2.13) and (2.14). Only the  $\hat{f}_{i+1/2,j}$  flux calculation is considered knowing that the  $\hat{g}_{i,j+1/2}$  flux is calculated in exactly the same fashion. In the steps below we assume the grid to be uniform and Cartesian.

Given the cell averages for the flow variables  $\bar{Q}$  for all  $(i, j)$ , at each fixed  $(x_{i+1/2}, y)$  we do the following:

Compute the average state  $Q_{i+1/2,j}$  using Roe averaging method for 2-D Euler equations. From (2.5)

$$Q_{RL} = \begin{bmatrix} \rho_{RL} \\ \rho_{RL} u_{RL} \\ \rho_{RL} v_{RL} \\ \rho_{RL} E_{RL} \end{bmatrix} = \begin{bmatrix} \rho_{RL} \\ \rho_{RL} u_{RL} \\ \rho_{RL} v_{RL} \\ \rho_{RL} (H_{RL} + p_{RL}) \end{bmatrix}$$

where  $R$  refers to  $(i+1, j)$ ,  $L$  refers to  $(i, j)$ , and  $RL$  refers to  $(i+1/2, j)$

The average quantities are obtained from [23] as:

$$\begin{aligned} \rho_{RL} &= \sqrt{\rho_R \rho_L} \\ u_{RL} &= \frac{\sqrt{\rho_R} u_R + \sqrt{\rho_L} u_L}{\sqrt{\rho_R} + \sqrt{\rho_L}} \\ v_{RL} &= \frac{\sqrt{\rho_R} v_R + \sqrt{\rho_L} v_L}{\sqrt{\rho_R} + \sqrt{\rho_L}} \\ H_{RL} &= \frac{\sqrt{\rho_R} H_R + \sqrt{\rho_L} H_L}{\sqrt{\rho_R} + \sqrt{\rho_L}} \end{aligned} \tag{2.46}$$

Using gas dynamics relations, other quantities can easily be obtained

$$a_{RL} = \sqrt{(\gamma - 1) \left( H_{RL} - 1/2 (u_{RL}^2 + v_{RL}^2) \right)} \tag{2.47}$$

$$p_{RL} = \frac{a_{RL}^2 \rho_{RL}}{\gamma}$$

Compute the eigenvalues and the corresponding right and left eigenvectors. [35] provides these eigenvalues and eigenvectors for 3-D case and the 2-D ones have been obtained from these eigenvectors.

The eigenvalues for 2-D Euler equations are given by [23] ;

$$\lambda_1 = \lambda_1(Q_{i+1/2,j}) = u_{RL} - a_{RL}$$

$$\lambda_2 = \lambda_2(Q_{i+1/2,j}) = u_{RL}$$

$$\lambda_3 = \lambda_2 \quad (2.48)$$

$$\lambda_4 = \lambda_4(Q_{i+1/2,j}) = u_{RL} + a_{RL}$$

The corresponding eigenvectors (right eigenvectors) are

$$R = \begin{bmatrix} 1 & 0 & 1 & 1 \\ u_{RL} - a_{RL} & 0 & u_{RL} & u_{RL} + a_{RL} \\ v_{RL} & 1 & v_{RL} & v_{RL} \\ H_{RL} - u_{RL}a_{RL} & v_{RL} & 1/2(u_{RL}^2 + v_{RL}^2) & H_{RL} + u_{RL}a_{RL} \end{bmatrix} \quad (2.49)$$

And the inverse eigenvectors (left eigenvectors) are

$$R^{-1} = \begin{bmatrix} 1/2(b2 + t0) & -1/2(t1 + ra) & -1/2t3 & t2 \\ -v_{RL} & 0 & 1 & 0 \\ 1 - b2 & t1 & t3 & -b1 \\ 1/2(b2 - t0) & -1/2(t1 - ra) & -1/2t3 & t2 \end{bmatrix} \quad (2.50)$$

where

$$\begin{aligned} ra &= 1/a_{RL}^2 \\ b1 &= (\gamma - 1) * ra^2 \\ b2 &= 1/2(u_{RL}^2 + v_{RL}^2) * b1 \\ t0 &= u_{RL} * ra \\ t1 &= b1 * u_{RL} \\ t2 &= 1/2b1 \\ t3 &= b1 * v_{RL} \end{aligned}$$

Transform all the given average values  $\bar{Q}$  into characteristic variables by using

$$\bar{v} = R^{-1}\bar{Q} \quad (2.51)$$

Apply one-dimensional reconstruction in the x-coordinate direction to each component of  $\bar{v}$  to obtain  $v_{i+1/2,y}^-$  and  $v_{i-1/2,y}^+$

For  $k = 3$ , since in this step, all the weights are the same as in the one-dimensional reconstruction equations (2.40)-(2.41),

$$\text{For } k = 3$$

Using (2.32)  $v_{i+1/2}^{(r)} = \sum_{j=0}^{k-1} C_{rj} \bar{v}_{i-r+j}$  ,  $r = 0,1,2$

$$\begin{aligned}
(r=0) \quad v_{i+1/2}^{(0)} &= C_{00} \bar{v}_i + C_{01} \bar{v}_{i+1} + C_{02} \bar{v}_{i+2} \\
(r=1) \quad v_{i+1/2}^{(1)} &= C_{10} \bar{v}_{i-1} + C_{11} \bar{v}_i + C_{12} \bar{v}_{i+1} \\
(r=2) \quad v_{i+1/2}^{(2)} &= C_{20} \bar{v}_{i-2} + C_{21} \bar{v}_{i-1} + C_{22} \bar{v}_i
\end{aligned} \tag{2.52}$$

Similarly using (2.26) (for WENO it becomes)  $v_{i-1/2}^{(r)} = \sum_{j=0}^{k-1} \tilde{C}_{rj} \bar{v}_{i-r+j}$  ,  $r = 0,1,2$

Remember  $\tilde{C}_{rj} = C_{r-1,j}$

$$\begin{aligned}
(r=0) \quad v_{i-1/2}^{(0)} &= C_{-10} \bar{v}_i + C_{-11} \bar{v}_{i+1} + C_{-12} \bar{v}_{i+2} \\
(r=1) \quad v_{i-1/2}^{(1)} &= C_{00} \bar{v}_{i-1} + C_{01} \bar{v}_i + C_{02} \bar{v}_{i+1} \\
(r=2) \quad v_{i-1/2}^{(2)} &= C_{10} \bar{v}_{i-2} + C_{11} \bar{v}_{i-1} + C_{12} \bar{v}_i
\end{aligned} \tag{2.53}$$

For uniform grid (the case we used in our 1-D numerical test cases), using Table (2.1) for the  $C_{rj}$  values at  $k = 3$  , and substituting these values we get

$$\begin{aligned}
v_{i+1/2}^{(0)} &= \frac{1}{3} \bar{v}_i + \frac{5}{6} \bar{v}_{i+1} - \frac{1}{6} \bar{v}_{i+2} \\
v_{i+1/2}^{(1)} &= -\frac{1}{6} \bar{v}_{i-1} + \frac{5}{6} \bar{v}_i + \frac{1}{3} \bar{v}_{i+1} \\
v_{i+1/2}^{(2)} &= \frac{1}{3} \bar{v}_{i-2} - \frac{7}{6} \bar{v}_{i-1} + \frac{11}{6} \bar{v}_i
\end{aligned} \tag{2.54}$$

And

$$v_{i-1/2}^{(0)} = \frac{11}{6} \bar{v}_i - \frac{7}{6} \bar{v}_{i+1} + \frac{1}{3} \bar{v}_{i+2}$$

$$v_{i-1/2}^{(1)} = \frac{1}{3}\bar{v}_{i-1} + \frac{5}{6}\bar{v}_i - \frac{1}{6}\bar{v}_{i+1} \quad (2.55)$$

$$v_{i-1/2}^{(2)} = -\frac{1}{6}\bar{v}_{i-2} + \frac{5}{6}\bar{v}_{i-1} + \frac{1}{3}\bar{v}_i$$

For  $k = 3$  also, the constants  $d_r$  are given in [1] as:

$$d_0 = \frac{3}{10}, \quad d_1 = \frac{3}{5}, \quad d_2 = \frac{1}{10} \quad (2.56)$$

By symmetry  $\tilde{d}_r = d_{k-1-r}$ , thus

$$\tilde{d}_0 = d_2 = \frac{1}{10}, \quad \tilde{d}_1 = d_1 = \frac{3}{5}, \quad \tilde{d}_2 = d_0 = \frac{3}{10} \quad (2.57)$$

The smooth indicators  $\beta_r$  are given by (2.42) for  $k = 3$ .

Now using equations, (2.40) and (2.41), the weights can be calculated as:

where the weights are defined as;

$$\begin{aligned} \alpha_0 &= \frac{d_0}{(\epsilon + \beta_0)^2}, & \alpha_1 &= \frac{d_1}{(\epsilon + \beta_1)^2}, & \alpha_2 &= \frac{d_2}{(\epsilon + \beta_2)^2} \\ \omega_0 &= \frac{\alpha_0}{(\alpha_0 + \alpha_1 + \alpha_2)}, & \omega_1 &= \frac{\alpha_1}{(\alpha_0 + \alpha_1 + \alpha_2)}, & \omega_2 &= \frac{\alpha_2}{(\alpha_0 + \alpha_1 + \alpha_2)} \\ \tilde{\alpha}_0 &= \frac{\tilde{d}_0}{(\epsilon + \beta_0)^2}, & \tilde{\alpha}_1 &= \frac{\tilde{d}_1}{(\epsilon + \beta_1)^2}, & \tilde{\alpha}_2 &= \frac{\tilde{d}_2}{(\epsilon + \beta_2)^2} \\ \tilde{\omega}_0 &= \frac{\tilde{\alpha}_0}{(\tilde{\alpha}_0 + \tilde{\alpha}_1 + \tilde{\alpha}_2)}, & \tilde{\omega}_1 &= \frac{\tilde{\alpha}_1}{(\tilde{\alpha}_0 + \tilde{\alpha}_1 + \tilde{\alpha}_2)}, & \tilde{\omega}_2 &= \frac{\tilde{\alpha}_2}{(\tilde{\alpha}_0 + \tilde{\alpha}_1 + \tilde{\alpha}_2)} \end{aligned}$$

From (2.45) the variables at the cell boundaries are evaluated

$$v_{i+1/2}^- = \omega_0 v_{i+1/2}^{(0)} + \omega_1 v_{i+1/2}^{(1)} + \omega_2 v_{i+1/2}^{(2)} \quad (2.58)$$

$$v_{i-1/2}^+ = \tilde{\omega}_0 v_{i-1/2}^{(0)} + \tilde{\omega}_1 v_{i-1/2}^{(1)} + \tilde{\omega}_2 v_{i-1/2}^{(2)} \quad (2.59)$$

Finally, substituting from (2.54) and (2.55) we get

$$\begin{aligned}
v_{i+1/2,y}^- &= \frac{1}{6}\omega_0(2\bar{v}_{i,j} + 5\bar{v}_{i+1,j} - \bar{v}_{i+2,j}) + \frac{1}{6}\omega_1(-\bar{v}_{i-1,j} + 5\bar{v}_{i+1,j} + 2\bar{v}_{i+1,j}) \\
&+ \frac{1}{6}\omega_2(\bar{v}_{i-2,j} - 7\bar{v}_{i-1,j} + 11\bar{v}_{i,j})
\end{aligned} \tag{2.60}$$

$$\begin{aligned}
v_{i-1/2,y}^+ &= \frac{1}{6}\tilde{\omega}_0(11\bar{v}_{i,j} - 7\bar{v}_{i+1,j} + 2\bar{v}_{i+2,j}) + \frac{1}{6}\tilde{\omega}_1(2\bar{v}_{i-1,j} + 5\bar{v}_{i,j} - \bar{v}_{i+1,j}) \\
&+ \frac{1}{6}\tilde{\omega}_2(-\bar{v}_{i-2,j} + 5\bar{v}_{i-1,j} + 2\bar{v}_{i,j})
\end{aligned} \tag{2.61}$$

Apply the one-dimensional reconstruction to  $v_{i-1/2,y}^+$  and  $v_{i+1/2,y}^-$  to obtain the reconstructed values  $v_{i-1/2,y_\alpha}^+$  and  $v_{i+1/2,y_\alpha}^-$  at the Gaussian integration points  $\alpha$ .

Two-point Gaussian quadrature (i.e.,  $\alpha = 1$  and  $\alpha = 2$ ) is used.

For  $\alpha = 1$

For the first Gaussian integration point  $(x_{i+1/2}, y_1)$  the optimal  $d_r$  constants are given by [18] as follows:

$$d_0 = \frac{210 - \sqrt{3}}{1080}, \quad d_1 = \frac{11}{18}, \quad d_2 = \frac{210 + \sqrt{3}}{1080}$$

using equations (2.40) and (2.41) for  $v_{i-1/2,y}^+$ , the weights are calculated as:

$$\begin{aligned}
\alpha_{0R} &= \frac{d_0}{(\epsilon + \beta_{0R})^2}, & \alpha_{1R} &= \frac{d_1}{(\epsilon + \beta_{1R})^2}, & \alpha_{2R} &= \frac{d_2}{(\epsilon + \beta_{2R})^2} \\
\omega_{0R} &= \frac{\alpha_{0R}}{(\alpha_{0R} + \alpha_{1R} + \alpha_{2R})}, & \omega_{1R} &= \frac{\alpha_{1R}}{(\alpha_{0R} + \alpha_{1R} + \alpha_{2R})}, & \omega_{2R} &= \frac{\alpha_{2R}}{(\alpha_{0R} + \alpha_{1R} + \alpha_{2R})}
\end{aligned}$$

$R$  denotes to the values evaluated for  $v_{i-1/2,y}^+$ . The smoothness indicators  $\beta$ 's are calculated according to (2.42) but as a function of  $v_{i-1/2,y}^+$ .

The reconstructed value  $v_{i-1/2,y_1}^+$  is given by [18] as:

$$v_{i-1/2,y_1}^+ = \omega_{0R} \left[ u_i + (3u_i - 4u_{i+1} + u_{i+2}) \frac{\sqrt{3}}{12} \right] + \omega_{1R} \left[ u_i - (-u_{i-1} + u_{i+1}) \frac{\sqrt{3}}{12} \right] \quad (2.62)$$

$$+ \omega_{2R} \left[ u_i - (3u_i - 4u_{i-1} + u_{i-2}) \frac{\sqrt{3}}{12} \right]$$

where  $u_i = v_{i-1/2,y}^+$  obtained in (2.62)

Now the same procedure above is repeated for  $v_{i+1/2,y}^-$

Again using equations (2.40) and (2.41) for  $v_{i+1/2,y}^-$ , the weights are calculated as:

$$\alpha_{0L} = \frac{d_0}{(\epsilon + \beta_{0L})^2}, \quad \alpha_{1L} = \frac{d_1}{(\epsilon + \beta_{1L})^2}, \quad \alpha_{2L} = \frac{d_2}{(\epsilon + \beta_{2L})^2}$$

$$\omega_{0L} = \frac{\alpha_{0L}}{(\alpha_{0L} + \alpha_{1L} + \alpha_{2L})}, \quad \omega_{1L} = \frac{\alpha_{1L}}{(\alpha_{0L} + \alpha_{1L} + \alpha_{2L})}, \quad \omega_{2L} = \frac{\alpha_{2L}}{(\alpha_{0L} + \alpha_{1L} + \alpha_{2L})}$$

$L$  denotes to the values evaluated for  $v_{i+1/2,y}^-$ . The smoothness indicators  $\beta$ 's are calculated according in (2.42) as a function of  $v_{i+1/2,y}^-$ .

The reconstructed value  $v_{i+1/2,y_1}^-$  is given by [18] as:

$$v_{i+1/2,y_1}^- = \omega_{0L} \left[ w_i + (3w_i - 4w_{i+1} + w_{i+2}) \frac{\sqrt{3}}{12} \right] + \omega_{1L} \left[ w_i - (-w_{i-1} + w_{i+1}) \frac{\sqrt{3}}{12} \right] \quad (2.63)$$

$$+ \omega_{2L} \left[ w_i - (3w_i - 4w_{i-1} + w_{i-2}) \frac{\sqrt{3}}{12} \right]$$

where  $w_i = v_{i+1/2,y}^-$  obtained in (2.63).

For  $\alpha = 2$

For the second Gaussian integration point  $(x_{i+1/2}, y_2)$  the optimal  $d_r$  constants are given by [18] as follows:

$$d_0 = \frac{210 + \sqrt{3}}{1080}, \quad d_1 = \frac{11}{18}, \quad d_2 = \frac{210 - \sqrt{3}}{1080}$$

Using these constants and following the same procedure in (A), we get the following reconstructed values at the second point Gaussian integration:

$$\begin{aligned} v_{i-1/2,y_2}^+ &= \omega_{0R} \left[ u_i - (3u_i - 4u_{i+1} + u_{i+2}) \frac{\sqrt{3}}{12} \right] + \omega_{1R} \left[ u_i - (u_{i-1} - u_{i+1}) \frac{\sqrt{3}}{12} \right] \\ &\quad + \omega_{2R} \left[ u_i + (3u_i - 4u_{i-1} + u_{i-2}) \frac{\sqrt{3}}{12} \right] \\ v_{i+1/2,y_2}^- &= \omega_{0L} \left[ w_i - (3w_i - 4w_{i+1} + w_{i+2}) \frac{\sqrt{3}}{12} \right] + \omega_{1L} \left[ w_i - (w_{i-1} - w_{i+1}) \frac{\sqrt{3}}{12} \right] \\ &\quad + \omega_{2L} \left[ w_i + (3w_i - 4w_{i-1} + w_{i-2}) \frac{\sqrt{3}}{12} \right] \end{aligned} \quad (2.64)$$

where  $u_i = v_{i-1/2,y}^+$ , and  $w_i = v_{i+1/2,y}^-$  are obtained from (2.61) and (2.62) respectively. Also, figure 2.3 shows reconstructed and gaussian points for one cell.

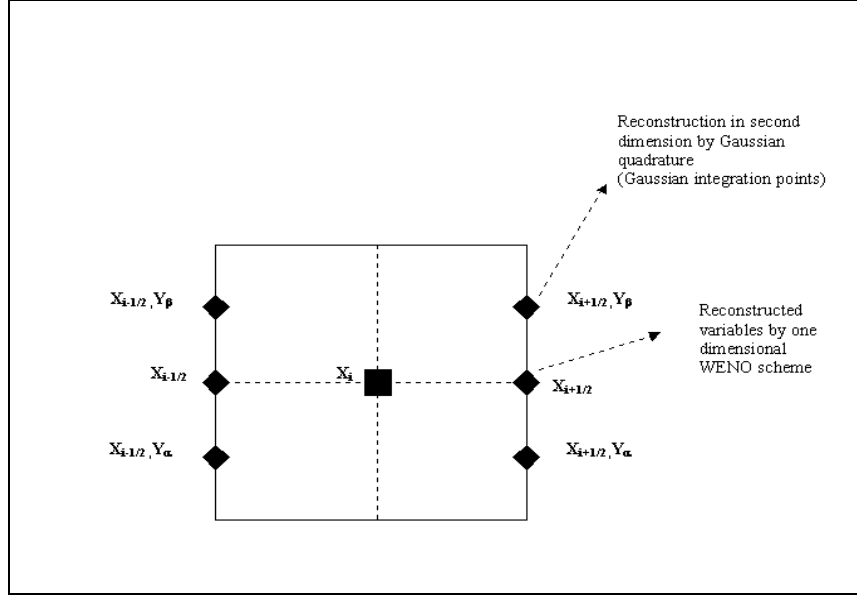


**Figure 2.3.** Reconstructed points and gaussian integration points for one cell

Again the  $\pm$  values are required at the same location  $(x_{i+1/2}, y_{\alpha})$ . Note that

$$v_{i+1/2, y_{\alpha}}^{+} = v_{i-1/2+1, y_{\alpha}}^{+}$$

So once  $v_{i-1/2, y_{\alpha}}^{+}$  is found,  $v_{i+1/2, y_{\alpha}}^{+}$  is easily obtained.

Transform back into physical space using

$$Q_{i+1/2, y1}^{\pm} = Rv_{i+1/2, y1}^{\pm}$$

$$Q_{i+1/2, y2}^{\pm} = Rv_{i+1/2, y2}^{\pm}$$

Apply an approximate Riemann solver to the variables at each Gaussian integration point (as will be explained in chapter 3)

The flux at the cell faces  $\hat{f}_{i+1/2, j}$  is now computed using Gaussian quadrature method as follow:

$$\hat{f}_{i+1/2, j} = h(Q_{i+1/2, y1}^{-}, Q_{i+1/2, y1}^{+}) * K1 + h(Q_{i+1/2, y2}^{-}, Q_{i+1/2, y2}^{+}) * K2 \quad (2.65)$$

where  $K1$  and  $K2$  are the Gaussian weights, for this two-point case [36]:

$$K1 = 1$$

$$K2 = 1$$

Once the fluxes at the cell faces are calculated, we can form the scheme (2.8) and calculate the RHS of this equation.

Note that  $\hat{f}_{i-1/2,j} = \hat{f}_{i+1/2-1,j}$ , so we need only to calculate  $\hat{f}_{i+1/2,j}$  values.

Also, as mentioned before, the  $\hat{g}_{i,j+1/2}$  flux is obtained in entirely the same way.

The procedure and formulation in the example, is valid for uniform Cartesian grids. For non-rectangular grids the formulation is similar. However, instead of using the Cartesian velocity components, the tangential and normal components are used. Derivation and formulas for the tangential and normal velocity components are set in Appendix (A).

## 2.8. Time Discretization

So far only the spatial discretization of (2.5) is considered. In this section we consider the time discretization. There are many types of time discretization; the one used is 3<sup>rd</sup> order Runge – Kutta method.

A class of TVD (total variation diminishing) high order Runge – Kutta methods is developed in [9]. These Runge – Kutta methods are used to solve a system of initial value problems of ODE's written as:

$$\frac{dQ}{dt} = L(Q) \quad (2.66)$$

resulting from a method of lines spatial approximation to a PDE such as:

$$\frac{\partial Q}{\partial t} = -\frac{\partial f(Q)}{\partial x} \quad (2.67)$$

Clearly, in our case,  $L(Q)$  in (2.66) is the WENO approximation to the derivative  $-\frac{\partial f(Q)}{\partial x}$  in the PDE (2.67).

Solving (2.66) with 1<sup>st</sup> order Euler forward time stepping:

$$Q^{n+1} = Q^n + \Delta t L(Q^n) \quad (2.68)$$

Assuming (2.68) is stable in a certain norm:

$$\|Q^{n+1}\| \leq \|Q^n\| \quad (2.69)$$

under a suitable restriction on  $\Delta t$

$$\Delta t \leq \Delta t_1 \quad (2.70)$$

then we look for higher order RK methods in which the stability condition (2.69) holds. But still this RK method may have a different restriction on  $\Delta t$

$$\Delta t \leq c\Delta t_1 \quad (2.71)$$

where  $c$  is the CFL coefficient for the high order time discretization.

Note that the stability condition (2.69) for the 1<sup>st</sup> order time stepping (2.68) can easily be attained in many cases for one-dimensional problems. However, for multi – dimensional conservation laws, the same stability condition can not be obtained (2.69) with the first order Euler stepping (2.68).

For example, if it is used for multi – dimensional conservation laws for which TVD is not possible but maximum norm stability can be maintained for high order spatial discretization plus forward Euler time stepping, then the same maximum norm stability can be maintained if TVD high order time discretization is used.

In [9], a general RK method for (2.67) is written in the form:

$$Q^{(p)} = \sum_{k=0}^{p-1} (\alpha_{pk} Q^{(k)} + \Delta t \beta_{pk} L(Q^{(p)})) , \quad p = 1, \dots, m \quad (2.72)$$

$$Q^{(0)} = Q^{(n)} , \quad Q^{(m)} = Q^{(n+1)}$$

If all the coefficients are nonnegative, i.e.,  $\alpha_{pk} \geq 0$ ,  $\beta_{pk} \geq 0$ , then (2.71) is just a convex combination of the Euler forward operators, with  $\Delta t$  replaced by  $\frac{\beta_{pk}}{\alpha_{pk}} \Delta t$ , since

by consistency  $\sum_{k=0}^{p-1} \alpha_{pk} = 1$ .

**Lemma** [9] The Runge – Kutta method (2.71) is TVD under the CFL coefficient (2.70).

$$c = \min_{p,k} \frac{\alpha_{pk}}{\beta_{pk}} \quad (2.73)$$

provided that  $\alpha_{pk} \geq 0$ ,  $\beta_{pk} \geq 0$ .

The optimal third order TVD Runge – Kutta method is given by [9]

$$\begin{aligned} Q^{(1)} &= Q^{(n)} + \Delta t L(Q^{(n)}) \\ Q^{(2)} &= \frac{3}{4} Q^{(n)} + \frac{1}{4} Q^{(1)} + \frac{1}{4} \Delta t L(Q^{(1)}) \\ Q^{(n+1)} &= \frac{1}{3} Q^{(n)} + \frac{2}{3} Q^{(2)} + \frac{2}{3} \Delta t L(Q^{(2)}) \end{aligned} \quad (2.74)$$

with a CFL coefficient  $c = 1$  in (2.73).

The third order Runge – Kutta method without TVD is given as:

$$\begin{aligned} Q^{(1)} &= Q^{(n)} + \frac{1}{2} \Delta t L(Q^{(n)}) \\ Q^{(2)} &= Q^{(n)} + \Delta t L(Q^{(1)}) \\ Q^{(n+1)} &= \frac{1}{2} Q^{(n)} + \frac{1}{3} Q^{(1)} + \frac{1}{6} Q^{(2)} + \frac{2}{3} \Delta t L(Q^{(2)}) \end{aligned}$$

The difference between TVD RK and RK without TVD is explained below:

The total variation of a discrete scalar solution is defined by:

$$TV(Q) = \sum_j |Q_{j+1} - Q_j|$$

The scheme is said to be TVD if

$$TV(Q^{n+1}) \leq TV(Q^n)$$

Thus for time discretization, if the norm in (2.69) is chosen to be the total variation norm, then the terminology becomes TVD time discretization.

(2.74) Is the way used for time discretization in this thesis.

## CHAPTER 3

### NUMERICAL FLUXES AND BOUNDARY CONDITONS

In this chapter we first briefly review the fluxes to be used in the framework of our schemes. Then we briefly describe the boundary conditions used in algorithm.

#### 3.1 The HLL Approximate Riemann Solver

Harten, Lax and Van Leer [22] put forward the following approximate Riemann solver

$$\tilde{Q}(x, t) = \begin{cases} Q_L & \text{if } \frac{x}{t} \leq S_L \\ Q^{hll} & \text{if } S_L \leq \frac{x}{t} \leq S_R \\ Q_R & \text{if } \frac{x}{t} \geq S_R \end{cases} \quad (3.1)$$

where

$$Q^{hll} = \frac{S_R Q_R - S_L Q_L + F_L - F_R}{S_R - S_L}$$

Where  $Q^{hll}$  is the constant state vector,  $S_L$  and  $S_R$  are the fastest signal velocities perturbing the initial data states  $Q_L$  and  $Q_R$  respectively. Fig 3.1 shows the structure of this approximate solution of the Riemann problem, called the approximate Riemann solver. Note that this approximation consists of just three constant states separated by two waves. The star region consists of a single constant state; all intermediate states separated by intermediate waves lumped into the single state  $Q^{hll}$ . The corresponding flux  $F^{hll}$  along t-axis is found from relations with the exact integrand replaced by the approximate solution. (3.1)

Note that  $F^{hll} \neq F(Q^{hll})$ .

$$\begin{aligned} F^{hll} &= F_R + S_R(Q^{hll} - Q_L) \quad \text{or} \\ F^{hll} &= F_R + S_R(Q^{hll} - Q_R) \end{aligned} \quad (3.2)$$

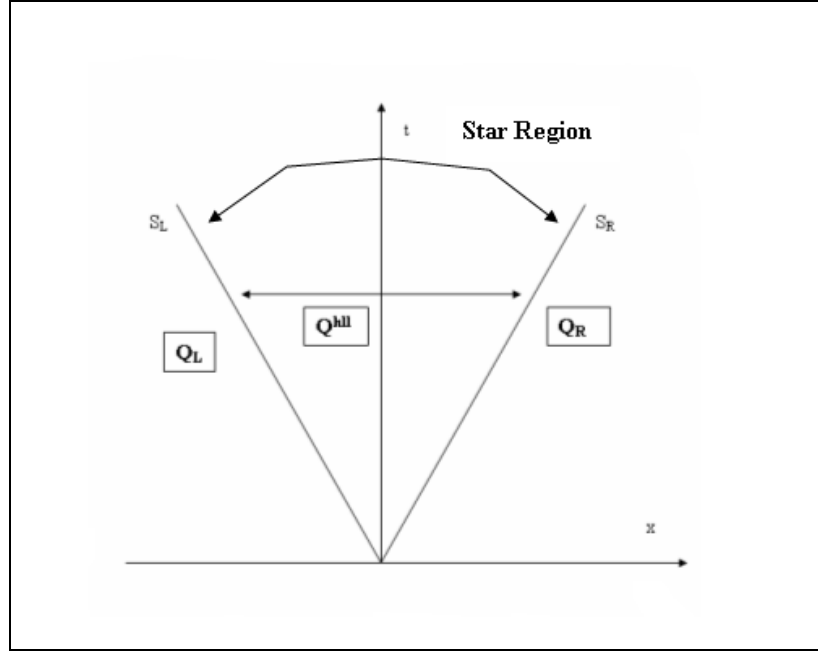


**Figure 3.1.** Approximate HLL Riemann Solver. Solution in the Star Region Consists of a single state  $Q^{hll}$  separated from data states by two waves of speeds  $S_L$  and  $S_R$

Note that relations 3.2 are also obtained from applying Rankine- Hugoniot Conditions across the left and right waves respectively.

$$F^{hll} = \frac{S_R F_L - S_L F_R + S_L S_R (Q_R - Q_L)}{S_R - S_L} \quad (3.3)$$

Procedures to estimate the wave speeds  $S_L$  and  $S_R$  are given in Section 3.3. The converged solution of HLL approximate Riemann Solver is the physical, entropy satisfying, solution of conservation laws. One of the requirements is the consistency with the integral form of the conservation laws.

A shortcoming of the HLL scheme is exposed by contact discontinuities, shear waves and material interfaces. These waves are associated with the multiple eigenvalue  $\lambda_2 = \lambda_3 = u$  See Fig. 3.2. This defect of HLL scheme may be corrected by restoring the

missing waves. Accordingly Toro, Spruce and Speares [37] proposed so called HLLC scheme, where C stands for Contact. In this scheme the missing middle waves are put back into the structure of the approximate Riemann Solver.

### Implementation of HLL Flux

In order to implement the HLL Riemann Solver one performs the following steps:

1. Compute the Wave Speeds  $S_L$  and  $S_R$  according to any of algorithms of section 3.3
2. Compute the HLL flux according to equation (3.1) and find  $F_{i+1/2}$

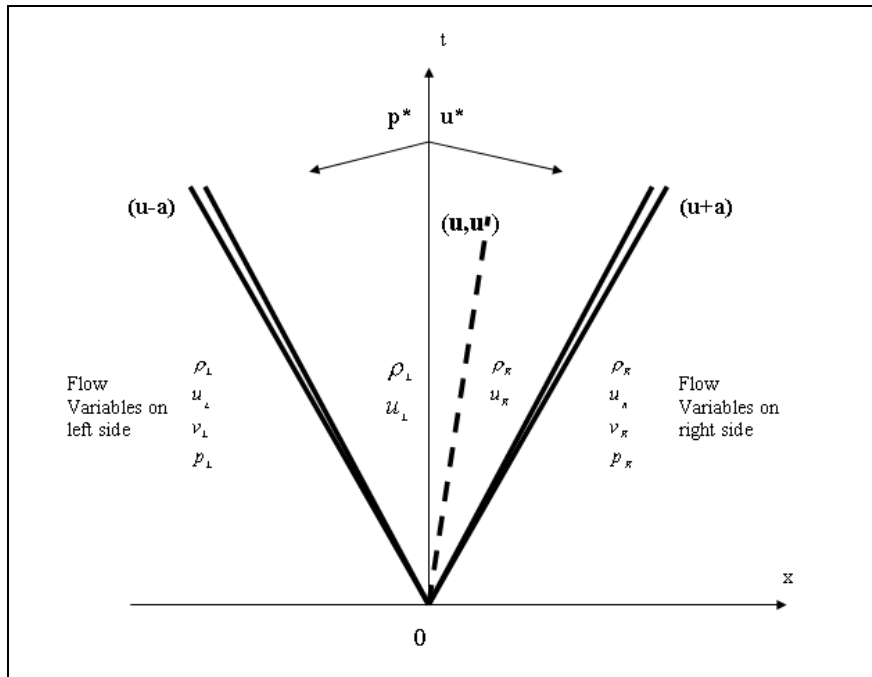


**Figure 3.2.** Structure of the exact solution of the Riemann problem for the x-split three dimensional Euler equations. There are four wave families associated with the eigenvalues  $u-a$ ,  $u$  (multiplicity 2) and  $u+a$

### **3.2 The HLLC Approximate Riemann Solver**

The HLLC scheme is a modification of the HLL scheme described in previous section, whereby the missing contact and shear waves are restored. Consider Figure 3-1 ,in which the complete structure of the solution of the Riemann problem is contained in

a sufficiently large control volume  $[ X_L, X_R ] \times [ 0, T ]$ . Now in addition to the slowest and fastest signal speeds  $S_L$  and  $S_R$  we include a middle wave of speed  $S_*$ , corresponding to the multiple eigenvalue  $\lambda_2 = \lambda_3 = u$  See Fig 3-3

The HLLC approximate Riemann solver is given as follows;

$$\tilde{Q}(x,t) = \begin{cases} Q_L & \text{if } \frac{x}{t} \leq S_L \\ Q_{*L} & \text{if } S_L \leq \frac{x}{t} \leq S_* \\ Q_{*R} & \text{if } S_* \leq \frac{x}{t} \leq S_R \\ Q_R & \text{if } \frac{x}{t} \geq S_R \end{cases} \quad (3.4)$$

where

$$Q^{hll} = \left( \frac{S_* - S_L}{S_R - S_L} \right) Q_{*L} + \left( \frac{S_R - S_*}{S_R - S_L} \right) Q_{*R} \quad (3.5)$$

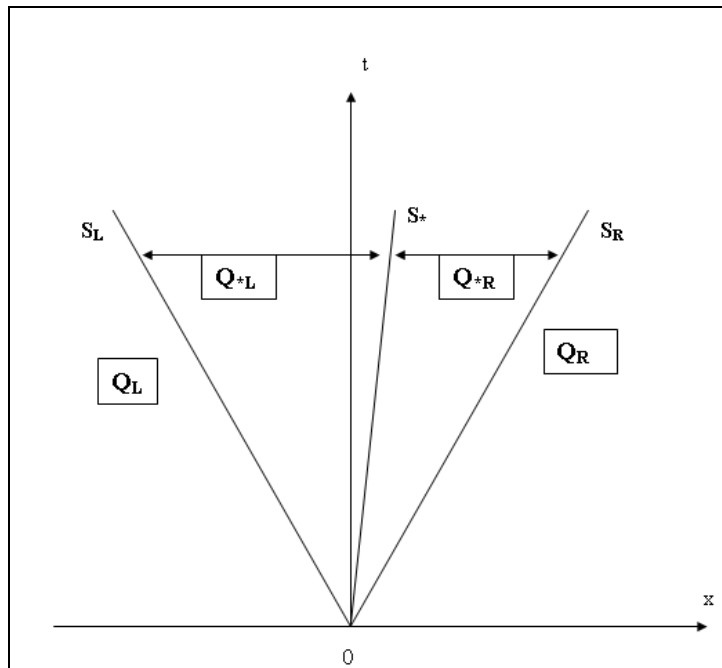


**Figure 3.3.** HLLC approximate Riemann Solver. Solution in the Star Region consists of two constant states separated from each other by a middle wave of speed  $S_*$

Figure 3.3 shows the structure of the HLLC scheme, By applying Rankine-Hugoniot conditions across each of the waves of speeds  $S_L$ ,  $S^*$ ,  $S_R$ , we obtain

$$\begin{aligned} F_{*L} &= F_L + S_L(Q_{*L} - Q_L) \\ F_{*R} &= F_R + S^*(Q_{*R} - Q_L) \\ F_{*R} &= F_R + S_R(Q_{*R} - Q_R) \end{aligned} \quad (3.6)$$

The aim is to find the vectors  $Q_{*L}$  and  $Q_{*R}$  so that the fluxes  $F_{*L}$  and  $F_{*R}$  can be determined from equation (3.6). We impose the following conditions on the approximate Riemann Solver.

$$\begin{aligned} u_{*L} &= u_{*R} = u_* \\ p_{*L} &= p_{*R} = p_* \\ v_{*L} &= v_L, v_{*R} = v_R \end{aligned} \quad (3.7)$$

Set  $S^*=u^*$

Now equations (3.6) can be re-arranged as;

$$\begin{aligned} Q_L &= S_L Q_{*L} - F_{*L} \\ Q_R &= S^* Q_{*R} - F_{*R} \end{aligned} \quad (3.8)$$

Where  $Q_L$  and  $Q_R$  are known constant vectors. Finally the solution vector is;

$$U_{*D} = \rho_D \left( \frac{S_D - u_D}{S_D - S^*} \right) \left[ \begin{array}{c} 1 \\ S^* \\ v_D \\ \frac{E_D}{\rho_D} + (S^* - u_D) \left[ S^* + \frac{p_D}{\rho_D (S_D - u_D)} \right] \end{array} \right] \quad (3.9)$$

Where  $D=L$  and  $D=R$ . Therefore the fluxes  $F_{*L}$  and  $F_{*R}$  in Equation (3.6) completely determined.

In view of Equation (3.4) the HLLC flux for the approximate Godunov method can be written as;

$$F_{i+\frac{1}{2}}^{hllc} = \begin{cases} F_L & \text{if } 0 \leq S_L \\ F_{*L} = F_L + S_L(Q_{*L} - Q_L) & \text{if } S_L \leq 0 \leq S_* \\ F_{*R} = F_R + S_R(Q_{*R} - Q_R) & \text{if } S_* \leq 0 \leq S_R \\ F_R & \text{if } 0 \geq S_R \end{cases} \quad (3.10)$$

Where  $Q_{*L}$  and  $Q_{*R}$  are given by Equation (3.9).

### **Implementation HLLC Flux**

To implement the HLLC Riemann solver , one performs the following steps.

1. Compute the wave Speeds  $S_L$ ,  $S_*$  and  $S_R$  according to any of the algorithms of section 3.3
2. Compute the appropriate states according to equation (3.9)
3. Compute HLLC flux according to equation (3.10)

### **3.3 Wave- Speed Calculations**

In order to determine completely the numerical fluxes in both the HLL and HLLC Riemann solvers we need to provide an algorithm for computing the wave speeds. For the HLL solver one requires  $S_L$  and  $S_R$ . For the HLLC scheme one requires in addition an estimate for the speed of the middle wave  $S_*$ . There are essentially two ways for calculating  $S_L$ ,  $S_*$  and  $S_R$ . To calculate the speeds directly is the most popular way of calculating wave speeds. A more recent approach relies on pressure-velocity estimates for the Star Region; these are then utilized to obtain  $S_L, S_*$  and  $S_R$  using exact wave relations.

#### **3.3.1. Direct Wave Speed Calculations**

The most popular approach for calculating the bounds for the minimum and maximum signal velocities present in the solution of the Riemann problem is to provide wave speeds  $S_L$  and  $S_R$ . It suggested as [38];

$$S_L = u_L - a_L, \quad S_R = u_R + a_R \quad (3.11)$$

And

$$S_L = \min(u_L - a_L, u_R - a_R), \quad S_R = (u_L + a_L, u_R + a_R) \quad (3.12)$$

These calculations make uses of data values only. It is also being used Roe average eigenvalues for the left and right non-linear waves are used, that is

$$S_L = \tilde{u} - \tilde{a}, \quad S_R = \tilde{u} + \tilde{a} \quad (3.13)$$

Where  $\tilde{u}$  and  $\tilde{a}$  are the Roe-average particle and sound speeds respectively, given as follows

$$\tilde{u} = \frac{\sqrt{\rho_L} u_L + \sqrt{\rho_R} u_R}{\sqrt{\rho_L} + \sqrt{\rho_R}}, \quad a = \left[ (\gamma - 1)(\tilde{H} - 0.5 \tilde{u}^2) \right]^{1/2}$$

where  $H = (E + p) / \rho$  (3.14)

$$H = \frac{\sqrt{\rho_L} H_L + \sqrt{\rho_R} H_R}{\sqrt{\rho_L} + \sqrt{\rho_R}}$$

### 3.3.2. Pressure-Velocity Based Wave Speed Calculations

A different approach for finding wave speed estimate was proposed by Toro [37]. Whereby one first finds an estimate for the pressure  $p^*$  in the Star Region and then one derives estimates for  $S_L$  and  $S_R$ . This is a simple task and several reliable choices are available. For the HLLC scheme of the previous section one also requires an estimate for the particle velocity  $u^*$ ; this is easily achieved, as approximations for  $p^*$  and  $u^*$  are closely related. The second approach derives a wave speed estimate  $S^*$  from the estimates  $S_L$  and  $S_R$  using conditions (3.7).

Suppose we have estimates  $p^*$  and  $u^*$  for the pressure and particle velocity in the Star Region. Then we choose the following wave speeds

$$S_L = u_L - a_L q_L, \quad S_* = u_*, \quad S_R = u_R + a_R q_R \quad (3.15)$$

Where

$$q_D = \begin{cases} 1 & \text{if } p_* \leq p_D \\ \left[ 1 + \frac{\gamma+1}{2\gamma} (p_* / p_D - 1) \right]^{1/2} & \text{if } p_* > p_D \end{cases} \quad (3.16)$$

This choice of wave speeds discriminates between shock and rarefaction waves. If the D wave (D=L or D=R) is a rarefaction then the speed  $S_D$  corresponds to the characteristic speed of the head of the rarefaction, which carries the fastest signal. If the wave is shock wave then the speed corresponds to an approximation of the true shock speed; then the speed used are exact but the pressure ratio across the shock is approximated, because the solution for  $p_*$  is an approximation.

As indicated earlier, there is an alternative way of computing the middle wave speed  $S_*$  in the HLLC Riemann Solver. Given the wave speeds  $S_L$  and  $S_R$ , by assuming  $S_* = u_*$  in equations (3.8) one obtains the following solutions for the pressure in the Star Region

$$p_{*L} = p_L + \rho_L (S_L - u_L)(S_* - u_L), \quad p_{*R} = p_R + \rho_R (S_R - u_R)(S_* - u_R) \quad (3.17)$$

From the condition Equation (3.7)  $p_{*L} = p_{*R}$  which leads to an expression for the speed  $S_*$  purely in terms of the assumed speeds  $S_L$  and  $S_R$ , namely

$$S_* = \frac{p_R - p_L + \rho_L u_L (S_L - u_L) - p_R u_R (S_R - u_R)}{\rho_L (S_L - u_L) - p_R (S_R - u_R)} \quad (3.18)$$

### 3.4 Lax Friedrichs Flux

This scheme is an first order scheme and obtained from forward in time and central in space approximations to partial derivatives. The Lax-Friedrichs solution at cell I is a weighted average of the solution of the Riemann Problem with the left and right neighboring states as data, at time  $t = \Delta t/2$ .

The conservation laws in one-dimension states that;

$$Q_t + F(Q)_x = 0 \quad (3.19)$$

Also the integral form of the conservation equation is defined as;

$$\frac{d}{dt} \int_{x_{i-1/2}}^{x_{i+1/2}} Q(x,t) dx = F(Q(x_{i-1/2})) - F(Q(x_{i+1/2})) \quad (3.20)$$

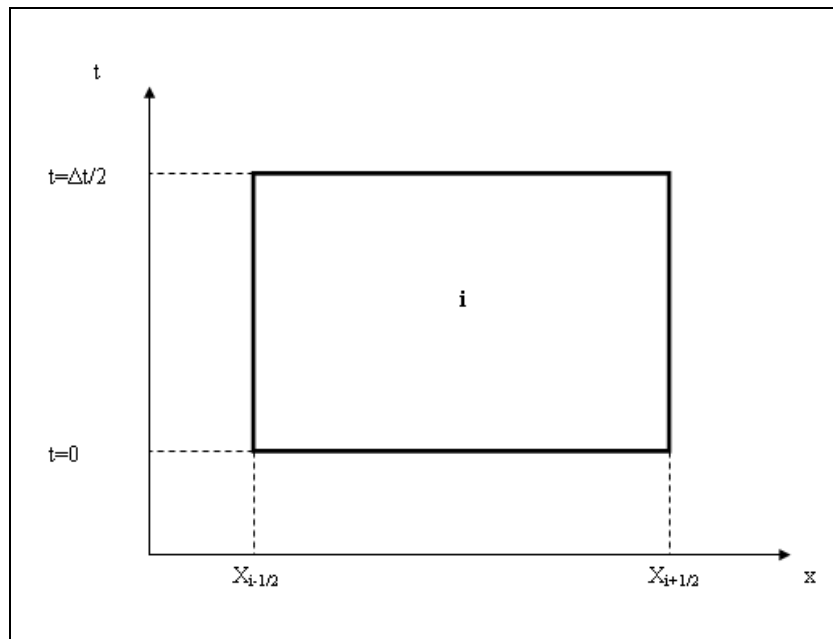


**Figure 3.4.** Control Volume  $V = [x_{i-1/2}, x_{i+1/2}] \times [0, \Delta t/2]$  on x-t plane

When the control volume displayed on Figure 3-4 used in (3.20)

$$\int_{x_{i-1/2}}^{x_{i+1/2}} \tilde{Q}(x, \frac{1}{2} \Delta t) dx = \int_{x_{i-1/2}}^{x_{i+1/2}} \tilde{Q}(x, 0) dx + \int_0^{\frac{\Delta t}{2}} F(\tilde{Q}(X_{i-1/2}, t)) dt - \int_0^{\frac{\Delta t}{2}} F(\tilde{Q}(X_{i+1/2}, t)) dt \quad (3.21)$$

Where

$$Q_i^{n+1} = \frac{1}{\Delta x} \int_{x_{i-1/2}}^{x_{i+1/2}} \tilde{Q}(x, \frac{\Delta t}{2}) dx \quad (3.22)$$

where  $\tilde{Q}$  is the solution of Riemann Problem  $RP(Q_{i-1}^n, Q_{i+1}^n)$

Substitute (3.22) into (3.21).

$$Q_i^{n+1} = \frac{1}{2} (Q_{i-1}^n + Q_{i+1}^n) + \frac{1}{2} \frac{\Delta t}{\Delta x} (F_{i-1}^n - F_{i+1}^n) \quad (3.23)$$

Also; If we discretize (3.19) on C.V.  $V=[X_{i-1/2}, X_{i+1/2}] \times [0, \Delta t/2]$  (Forward in time and Central in space);

$$Q_i^{n+1} = Q_i^n + \frac{\Delta t}{\Delta x} (F_{i-1/2}^n - F_{i+1/2}^n) \quad (3.24)$$

After substituting (3.24) into (3.23) we get Lax-Friedrichs intercell flux as;

$$F_{i+1/2}^{LF} = \frac{1}{2} (F_i^n + F_{i+1}^n) + \frac{1}{2} \frac{\Delta x}{\Delta t} (Q_{i+1}^n - Q_i^n) \quad (3.25)$$

This is the conventional numerical flux for the Lax-Friedrichs scheme when applied to systems of conservation laws (3.19). The Lax-Friedrichs method is monotone, when applied to systems of conservation laws (3.19).

### 3.4.1. Monotone Schemes

Useful class of methods for systems of conservation laws (3.19) is those which are monotone.

$$Q_i^{n+1} = H(Q_{i-k_L+1}^n, \dots, Q_{i+k_R}^n) \quad (3.26)$$

With  $k_L$  and  $k_R$  two non-negative integers,

Monotone scheme is a scheme if  $H$  is a non-decreasing function of each of its arguments.

$$\frac{\partial H}{\partial Q_j^n} \geq 0 \quad \forall j \quad (3.27)$$

This property in turn is the discrete version of the following property of the exact solution of the conservation law. (3.19) : If two initial data functions  $v_0(x)$  and  $u_0(x)$  for (3.19) satisfy  $v_0(x) \geq u_0(x)$  for all  $x$ , then their corresponding solutions  $v(x,t)$  and  $u(x,t)$  satisfy  $v(x,t) \geq u(x,t)$ ,  $t > 0$ . Hence monotone schemes mimic a basic property of exact solutions of conservation laws (3.19)

#### **Theorem 3-1 Monotonicity and the Flux**

A three point scheme of the form is given by (3.24) for non-linear conservation law (3.19) is monotone if ;

$$\frac{\partial}{\partial Q_i^n} f_{i+1/2}(Q_i^n, Q_{i+1}^n) \geq 0 \quad \text{and} \quad \frac{\partial}{\partial Q_{i+1}^n} f_{i+1/2}(Q_i^n, Q_{i+1}^n) \leq 0 \quad (3.28)$$

That is, the numerical flux  $f_{i+1/2}(Q_i^n, Q_{i+1}^n)$  is an increasing function of its first argument and a decreasing function of its second argument.

### 3.4.2. Application of Monotonicity and flux theorem to the Lax-Friedrichs Method.

For general conservation law (3.19) the Lax-Friedrichs flux is given by (3.25);

$$F_{i+1/2}^{LF} = \frac{1}{2}(F_i^n - F_{i+1}^n) + \frac{1}{2} \frac{\Delta x}{\Delta t} (Q_i^n - Q_{i+1}^n)$$

When condition (3.28) applied monotonicity is ensured provided

$$-1 \leq \frac{\Delta t \lambda_{\max}(Q)}{\Delta x} \leq 1 \quad (3.29)$$

where  $\lambda(q) = \partial f / \partial q$  is the characteristic speed

That is, provided the CFL stability condition is enforced properly, the Lax-Friedrichs method is monotone.

### 3.5 Lax-Wendroff Scheme

Recall the solution of the Riemann problem by invoking the integral form of the conservation laws (3.19) .

$$Q_{i+\frac{1}{2}}^{n+\frac{1}{2}} = \frac{1}{\Delta x} \int_{X_{i-1/2}}^{X_{i+1/2}} \tilde{Q}_{i+\frac{1}{2}}(x, \frac{\Delta t}{2}) dx \quad (3.30)$$

where  $\tilde{Q}_{i+\frac{1}{2}}$  is the solution of Riemann Problem  $RP(Q_i^n, Q_{i+1}^n)$

As done for Lax-Friedrichs scheme one may replace the integral involving the solution of the Riemann problem by invoking the integral form of conservation laws. Analogously; in the C.V  $V=[X_{i-1/2}, X_{i+1/2}] \times [0, \Delta t/2]$ ;

$$F_{i+\frac{1}{2}}^{LW} = F\left(Q_{i+\frac{1}{2}}^{n+\frac{1}{2}}\right); \quad Q_{i+\frac{1}{2}}^{n+\frac{1}{2}} = \frac{1}{2}(Q_i^n + Q_{i+1}^n) + \frac{1}{2} \frac{\Delta t}{\Delta x} (F_i^n - F_{i+1}^n) \quad (3.31)$$

### 3.6 First-Order Centred (FORCE) Flux

The FORCE flux [20] is a recent centred flux which is an arithmetic mean of the Lax-Friedrichs and Lax-Wendroff fluxes. The numerical viscosity of the FORCE flux is smaller than that of the Lax-Friedrichs flux by a factor of two.

$$\begin{aligned}
 F_{i+\frac{1}{2}}^{FORCE} &= \frac{1}{2} \left( F_{i+\frac{1}{2}}^{LW} + F_{i+\frac{1}{2}}^{LF} \right) \\
 F_{i+\frac{1}{2}}^{FORCE} &= \frac{1}{4} \left( F_i^n + 2F^n(Q_{i+\frac{1}{2}}^{n+\frac{1}{2}}) + F_{i+1}^n - \frac{\Delta x}{\Delta t} (Q_{i+1}^n - Q_i^n) \right) \\
 Q_{i+\frac{1}{2}}^{n+\frac{1}{2}} &= \frac{1}{2} (Q_{i+1}^n + Q_i^n) + \frac{1}{2} (F_i^n - F_{i+1}^n)
 \end{aligned} \tag{3.32}$$

### 3.7 Rusanov Flux

For a given Riemann problem we can identify a positive speed  $S^+$ . Then by choosing  $S_L = -S^+$  and  $S_R = S^+$  in HLL flux (3.3) one obtains a Rusanov flux [39].

$$F_{i+1/2}^{RUSANOV} = \frac{1}{2} (F_i^n + F_{i+1}^n) - \frac{1}{2} S^+ (Q_{i+1}^n - Q_i^n) \tag{3.33}$$

As to the choice of the speed  $S^+$ , Davis [38] considered.

$$S^+ = \max \left\{ |u_i - a_i|, |u_{i+1} - a_{i+1}|, |u_i + a_i|, |u_{i+1} + a_{i+1}| \right\} \tag{3.34}$$

Actually, the above speed is bounded by;

$$S^+ = \max \left\{ |u_i + a_i|, |u_{i+1} + a_{i+1}| \right\} \tag{3.35}$$

Another possible choice is  $S^+ = S_{\max}^n$ , the maximum wave speed present at appropriate time found by imposing Courant Stability condition. That is ;  $S^+$  is related to the time step  $\Delta t$  and the grid spacing  $\Delta x$  via ;

$$S_{\max}^n = \frac{C_{cfl} \Delta x}{\Delta t} \quad (3.36)$$

Courant number is chosen to be  $C_{cfl}=1$  one has  $S^+=\Delta x/\Delta t$ , which results in the Lax-Friedrichs numerical flux (3.25)

### 3.8 The Upwind MUSTA Fluxes

A very simple and general approach to the construction of numerical fluxes, which combines the simplicity of centred fluxes and the good accuracy of the Godunov method is Multi-Stage (MUSTA) approach [18,25,26]. The key idea of the original MUSTA is to open the Riemann fan by evolving in time the initial data  $Q_L, Q_R$

$$\frac{\partial}{\partial t} Q + \frac{\partial}{\partial x} F = 0, \quad Q(x,0) = \begin{cases} Q_L = Q_i & x < 0 \\ Q_R = Q_{i+1} & x > 0 \end{cases}$$

Riemann solvers recognize all waves in the Riemann fan and therefore provide good resolution of delicate features of the flow, such as contact discontinuities and Shear waves. Incomplete Riemann solvers (HLL Flux) do not recognize the intermediate waves in the Riemann fan and lump them all in one state. Centred fluxes (Lax-Friedrichs, Lax-Wendroff, FORCE Flux ...etc) can be regarded as very rough Riemann Solvers in which the Riemann fan is not opened at all.

The MUSTA approach develops upwind numerical fluxes by utilizing centred fluxes in a multi-stage predictor-corrector fashion. Effectively, MUSTA can be regarded as an approximate Riemann solver in which the predictor step opens the Riemann fan and the corrector step makes use of the information extracted from the opened Riemann fan, which is precisely the information needed for the upwind numerical flux. The advantages of this multi-stage predictor –corrector solver are its simplicity and generality.

The key idea of MUSTA is to open Riemann fan by solving local Riemann Problem (3.37) numerically rather than analytically. The existing discontinuity is

resolved by applying in the corrector step a simple flux, such as a centred flux. A particularly successful flux, constructed on the basis of the centred FORCE flux, is used in corrector step.

### Implementation of MUSTA Flux

In order to implement the MUSTA Flux one performs the following steps:

1. For initialization of the iteration, set  $k=1$  and  $Q_L^{(1)}=Q_L$  and  $Q_R^{(1)}=Q_R$
2. Evaluate the Fluxes at  $k=1$

$$F_L^{(1)}=F(Q_L^{(1)}) \text{ and } F_R^{(1)}=F(Q_R^{(1)})$$

3. Evaluate the centred FORCE Flux at  $k=1$ .

$$Q_M^{(1)} = \frac{1}{2}(Q_L^{(1)} + Q_R^{(1)}) + \frac{1}{2}(F_L^{(1)} - F_R^{(1)})$$

$$F_{i+1/2}^{(1)} = \frac{1}{4} \left( F_L^{(1)} + 2F^{(1)}(Q_M) + F_R^{(1)} - \frac{\Delta x}{\Delta t} (Q_R^{(1)} - Q_L^{(1)}) \right)$$

4. New Flow variables for following iteration step is calculated. By simple discretization (Forward in time and Forward in space) of Euler equation across control volume of Figure3-5

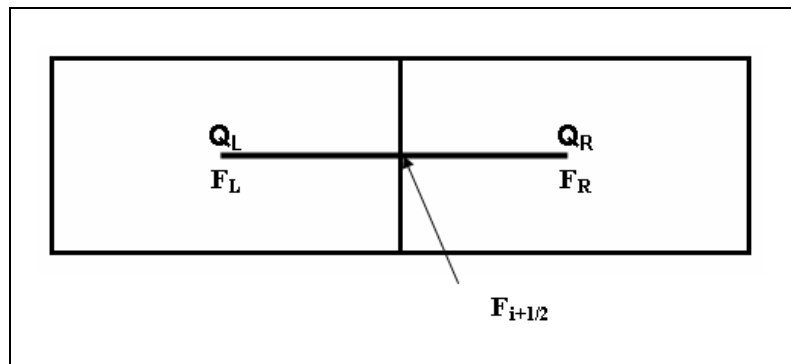


**Figure 3.5** .The Control Volume For Simple discretization.

$$Q_L^{(i+1)} = Q_L^{(i)} + \frac{\Delta t}{\Delta x} (F_L^{(i)} - F_{i+1/2}^{(i)})$$

$$Q_R^{(i+1)} = Q_R^{(i)} + \frac{\Delta t}{\Delta x} (F_{i+1/2}^{(i)} - F_R^{(i)})$$

## 5. Go to Step 1

The procedure is stopped at the end of Step1 if desired number of stages  $k$  has been reached. Practical Investigations [18] suggests that a number of stages between 3 and 4 gives numerical results that are comparable with those from the most accurate of fluxes, namely, the first order Godunov upwind flux used in conjunction with the exact Riemann solver.

### 3.9 Boundary Conditions

Here five different types of boundary conditions are discussed. They are: inflow, outflow, wall (body surface), symmetry, and periodic boundary conditions. Also information about ghost points is mentioned.

#### 3.9.1. Inflow Boundary Condition

The inflow boundary condition is defined as the location for which  $\vec{V} \cdot \vec{h}$  is negative. Where,  $\vec{V} = u \vec{i} + v \vec{j}$  and  $\vec{h}$  is the unit vector normal to the boundary in an outward direction.

For supersonic inflow, since all the eigenvalues are positive, which means that four characteristics enter into the domain and therefore four analytical boundary conditions may be specified. In this thesis, the inflow boundary is set at the free-stream that is the values  $u$ ,  $v$ ,  $\rho$ , and  $p$  are specified at the free-stream condition as can be seen at Figure 3-6.

$$u = u_{\infty}$$

$$v = v_{\infty}$$

$$\rho = \rho_{\infty}$$

$$p = p_{\infty}$$

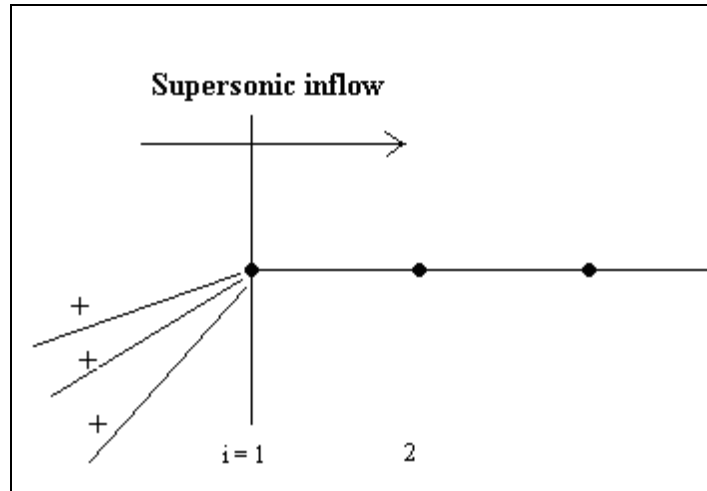


**Figure 3.6.** Properties of Supersonic inflow BC.

In this Thesis, Test cases require only supersonic inflow boundary condition. No subsonic inflow Boundary condition is required.

### 3.9.2. Outflow Boundary Condition

The outflow boundary is defined as a location for which  $\vec{V} \cdot \vec{n}$  is positive.

For supersonic outflow, again all the eigenvalues are positive, so all the characteristics leave the domain. Then the information at the boundary is received from the interior points of the domain. Therefore, no boundary condition is specified at the exit.

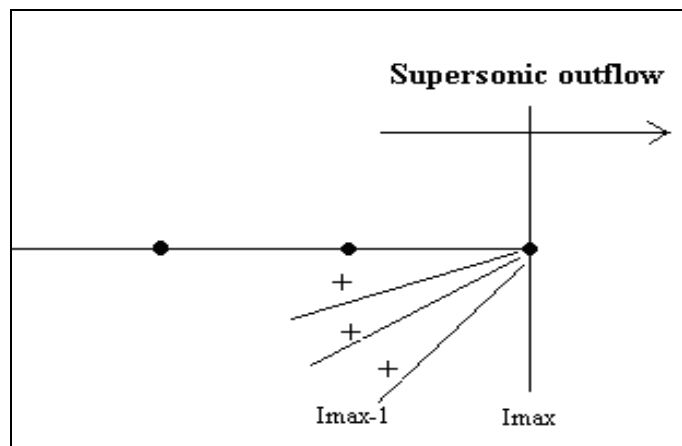


**Figure 3.7.** Properties of Supersonic Outflow BC.

The properties at the outflow boundary are extrapolated from the interior points. In the test cases, zero<sup>th</sup> order extrapolation is used (See Figure 3-7)

$$Q_{i \max, j} = Q_{i \max - 1, j} \quad (3.37)$$

If the outflow is subsonic, then two of the eigenvalues are positive (outgoing) and one is negative (incoming from outside). Therefore, one analytical boundary condition may be specified and the other two are extrapolated from the interior domain in the same fashion as in the previous subsection. This condition is illustrated in Figure (3-8) :

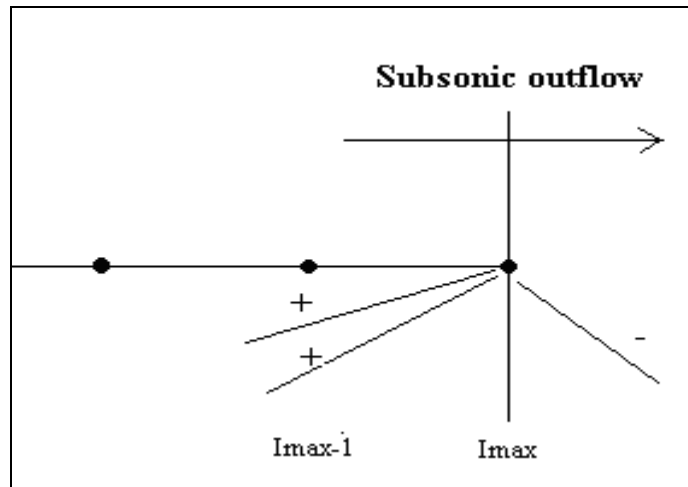


**Figure 3.8.** Properties of Subsonic Outflow BC.

### 3.9.3. Wall Boundary Condition (Body Surface)

In Euler equations, since the flow is inviscid, the slip condition is used at the surface. So the flow must be tangent to the solid wall, thus:

$$\vec{V} \cdot \vec{h} = 0, \quad \vec{V} = u \vec{i} + v \vec{j}, \quad \vec{h} \text{ is the unit vector normal to the wall.}$$

There are many ways for determining the boundary condition at the wall, the following one is used:

**Density:** The density is extrapolated from the interior points. Using zero<sup>th</sup> order extrapolation:

$$\rho_{i,js} = \rho_{i,js-1} \quad (\text{for upper wall})$$

$$\rho_{i,js} = \rho_{i,js+1} \quad (\text{for lower wall})$$

$s$  Stands for the wall location.

**Velocity Components:** The velocity components at the surface (wall) are determined as follows [34]:

The velocity vector and unit vector normal to the lines of constant  $\eta$  are given by

$$\begin{aligned} \vec{V} &= u \vec{i} + v \vec{j} \\ \vec{h}_\eta &= \frac{\nabla \eta}{|\nabla \eta|} = \frac{\eta_x \vec{i} + \eta_y \vec{j}}{\sqrt{\eta_x^2 + \eta_y^2}} \end{aligned} \quad (3.38)$$

Using metrics relations

$$\eta_x = -\frac{1}{J} y_\xi, \quad \eta_y = \frac{1}{J} x_\xi$$

where,  $J = x_\xi y_\eta - x_\eta y_\xi$  is the Jacobian.

$$\begin{aligned} y_\eta &= y(i, j) - y(i, j-1) \\ x_\eta &= x(i, j) - x(i, j-1) \\ x_\xi &= x(i, j) - x(i-1, j) \\ y_\xi &= y(i, j) - y(i-1, j) \end{aligned} \quad (3.39)$$

Substituting into (3.38), we obtain:

$$\vec{h}_\eta = \frac{-y_\xi \vec{i} + x_\xi \vec{j}}{\sqrt{x_\xi^2 + y_\xi^2}}$$

Now the normal component  $V_{n\eta}$  is determined as follows:

$$V_{n\eta} = \vec{V} \cdot \vec{h}_\eta = (u \vec{i} + v \vec{j}) \cdot \frac{(-y_\xi \vec{i} + x_\xi \vec{j})}{\sqrt{x_\xi^2 + y_\xi^2}}$$

$$V_{n\eta} = \frac{-u y_\xi + v x_\xi}{\sqrt{x_\xi^2 + y_\xi^2}} \quad (3.40)$$

similarly, the tangential component  $V_{t\eta}$  is obtained as:

$$V_{t\eta} = \left[ \vec{V} \cdot \vec{V} - V_{n\eta}^2 \right]^{1/2} = \left[ (u^2 + v^2) - \frac{(-u y_\xi + v x_\xi)^2}{x_\xi^2 + y_\xi^2} \right]^{1/2} \quad (3.41)$$

Arranging the equation above yields:

$$V_{t\eta} = \frac{u x_\xi + v y_\xi}{\sqrt{x_\xi^2 + y_\xi^2}} \quad (3.42)$$

Equations, (3.40) and (3.42) determine the normal and tangential components of velocity  $\vec{V}$  at the surface. In these equations,  $u$  and  $v$  are evaluated at known interior points, where,  $x_\xi$  and  $y_\xi$  are evaluated at the surface. Solving equations (3.40) and (3.42), the flow velocities  $u$  and  $v$  at the surface are obtained as:

$$u_s = x_\xi V_{t\eta} + y_\xi V_{n\eta}$$

$$v_s = y_\xi V_{t\eta} - x_\xi V_{n\eta}$$

**Pressure:** The wall pressure is typically specified by applying the normal momentum equation in the generalized coordinates. We apply the normal momentum equation in the generalized coordinated to make it valid for orthogonal and non-orthogonal grids also for curved and straight walls.

The pressure is extrapolated using the normal momentum equation is [34]:

$$\frac{\partial p}{\partial \eta} (x_\xi^2 + y_\xi^2) = \frac{\partial p}{\partial \xi} (x_\xi x_\eta + y_\xi y_\eta) + \rho U (x_{\xi\xi} v - y_{\xi\xi} u) \quad (3.43)$$

where,  $U = u y_\eta - v x_\eta$

Solving (3.43), the pressure at the surface is obtained.

Besides the Slip condition that is required for Solving Euler Equation. For Solving Double Mach Reflection Test Case, One requires some special treatment for the wall boundary condition. For Double Mach Reflection (DMR) Problem, reflective wall BC is used. Apart from slip Boundary condition, for reflective boundary condition velocity normal to the wall face is reflected with conserving its direction.

#### 3.9.4. Symmetric Wall Boundary Condition

The symmetric boundary is used for configurations, which are symmetric as shown in the Figure (3.9).

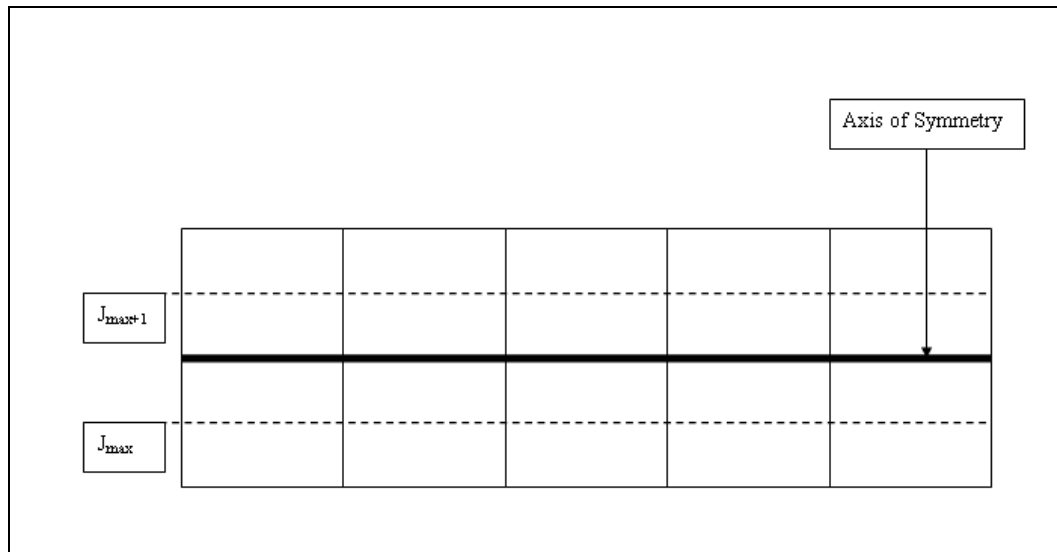


**Figure 3.9.** Symmetric Boundary Condition

The grid line  $j = j_{max}$  is set below the axis of symmetry and the line  $j = j_{max+1}$  is set above the axis of symmetry.

From physical point of view, the following constraints hold for the flow and thermodynamics [29]:

$$\rho_{i,j \max} = \rho_{i,j \max+1}$$

$$u_{i,j \max} = u_{i,j \max+1}$$

$$v_{i,j \max} = -v_{i,j \max+1}$$

$$E_{i,j \max} = E_{i,j \max+1}$$

### 3.9.5. Periodic Boundary Conditions

The periodic boundary conditions are applied in the cascade problem. The cascade is considered as an infinite number of identical blades stacked on top each other.

The periodic boundary conditions are explained as follow:

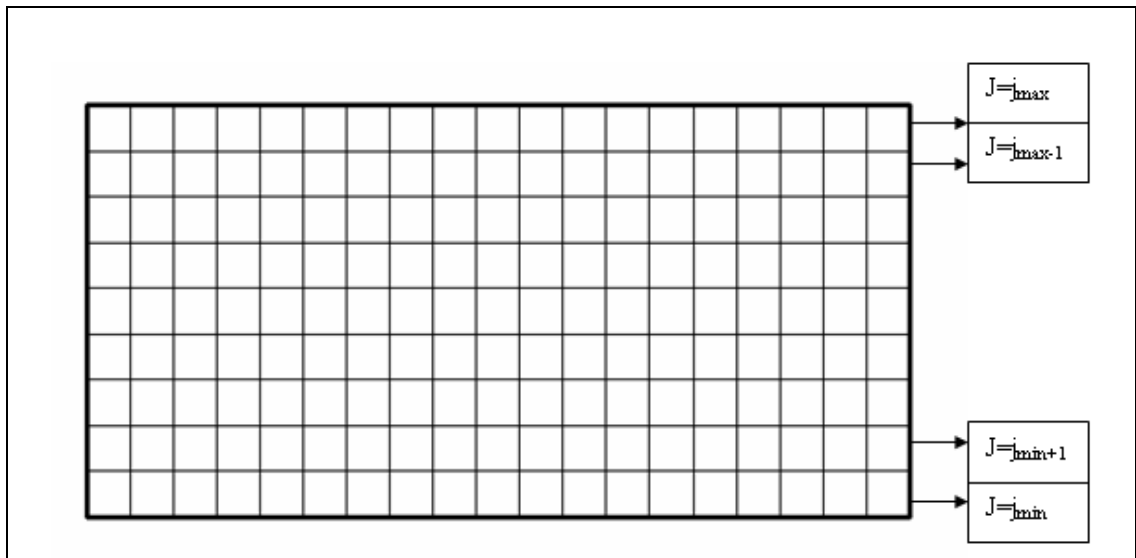


**Figure 3.10.** Periodic boundary condition

$$Q_{i,j \min} = Q_{i,j \max-1}$$

$$Q_{i,j \max} = Q_{i,j \min+1} \quad \text{where} \quad Q = \begin{bmatrix} \rho \\ \rho u \\ \rho v \\ \rho E \end{bmatrix}$$

### 3.9.6. Ghost Points

The most natural way of treating the boundary conditions for the WENO scheme is to use only the available values inside the computational domain when choosing the

stencil. In other words, we only consider convex combination of the all the candidate stencils, which are completely contained inside the computational domain. That's why we set all the necessary ghost points outside the computational domain to make sure that they don't contain any used stencil.

The ghost points needed for the WENO reconstruction are set out side the computational domain. In other words, only stencils completely contained inside the computational domain are used in the computations.

The values at the ghost points are extrapolated from the values at the boundary conditions.

$$Q_g = Q_{bc}$$

where  $g$  denotes for ghost points and  $bc$  denotes for boundary condition.

## CHAPTER 4

### RESULTS AND DISCUSSION

In this chapter, finite volume WENO scheme is tested for different problems using different fluxes. These fluxes are HLLC flux, MUSTA flux, Lax-Friedrich flux and Rusanov Flux. When applied with WENO scheme so they are named as; WENO-HLLC, WENO-MUSTA, WENO-LF and WENO-RUSANOV. The flowchart of the corresponding algorithm is given in Appendix A. The scheme is tested for one and two dimensions. For 1-D, a shock tube problem is used. For 2-D, Double Mach Reflection problem, Supersonic Channel Flow problem and Wedge Cascade problem are used.

#### 4.1 One Dimensional Results

The 1-D Shock Tube Problem [29] involves severe flow structures involving shock wave, contact surface and expansion waves.

##### 4.1.1. Problem Description

A shock tube is a device which is used in the experimental investigation of several physical phenomena such as shock structure and aerothermodynamics of supersonic/hypersonic vehicles.

A shock tube is a relatively long and a constant area tube which is divided into two sections by a diaphragm. The problem is shown in figure 4.1. The section including the high pressure gas is called the driver section and denoted by 2 in figure 4.1. Also the section including low pressure gas is called the driven section and denoted by 1 in figure 4.1.

Complete specification of driver and expansion gases is sufficient to provide the solution for the shock tube problem which is also known as Riemann Problem.

Once the diaphragm is ruptured, a normal shock propagates into the low pressure region 1 and a series of expansion waves propagates into the high pressure region 2.

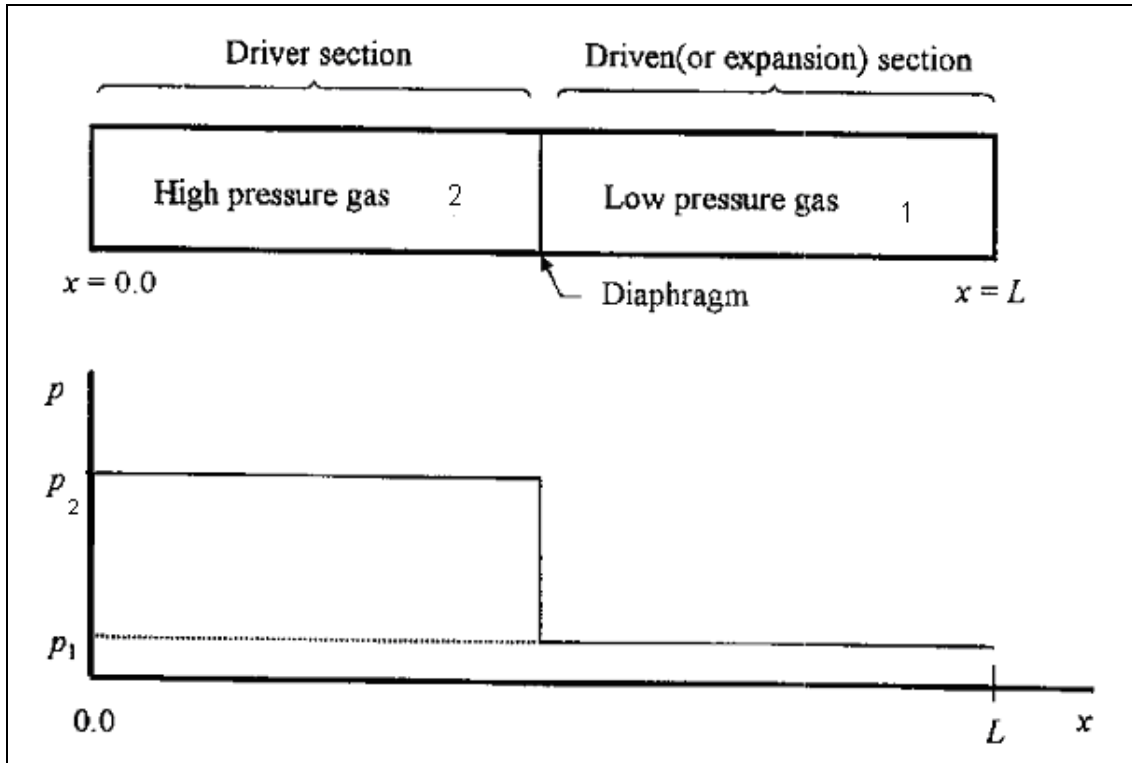


**Figure 4.1.** Shock Tube at the initial state and corresponding pressure distribution [29]

In this thesis two standard tests cases are investigated. These are the Sod's problem [30] and the Lax's Problem [31]. These test cases are using different Riemann Type initial data:

$$Q(x,0) = \begin{cases} Q_L & \text{if } x \leq 0 \\ Q_R & \text{if } x > 0 \end{cases}$$

### 4.1.2. The Sod's Problem

For the Sod's problem the Riemann Type initial data is defined as;

$$Q_L = \begin{bmatrix} \rho_L \\ u_L \\ P_L \end{bmatrix} = \begin{bmatrix} 1.000 \\ 0.000 \\ 1.000 \end{bmatrix}$$

$$Q_R = \begin{bmatrix} \rho_R \\ u_R \\ P_R \end{bmatrix} = \begin{bmatrix} 0.125 \\ 0.000 \\ 0.100 \end{bmatrix}$$

This problem is investigated with Finite Volume WENO scheme with different fluxes. Results can be seen at Figures 4.2-6

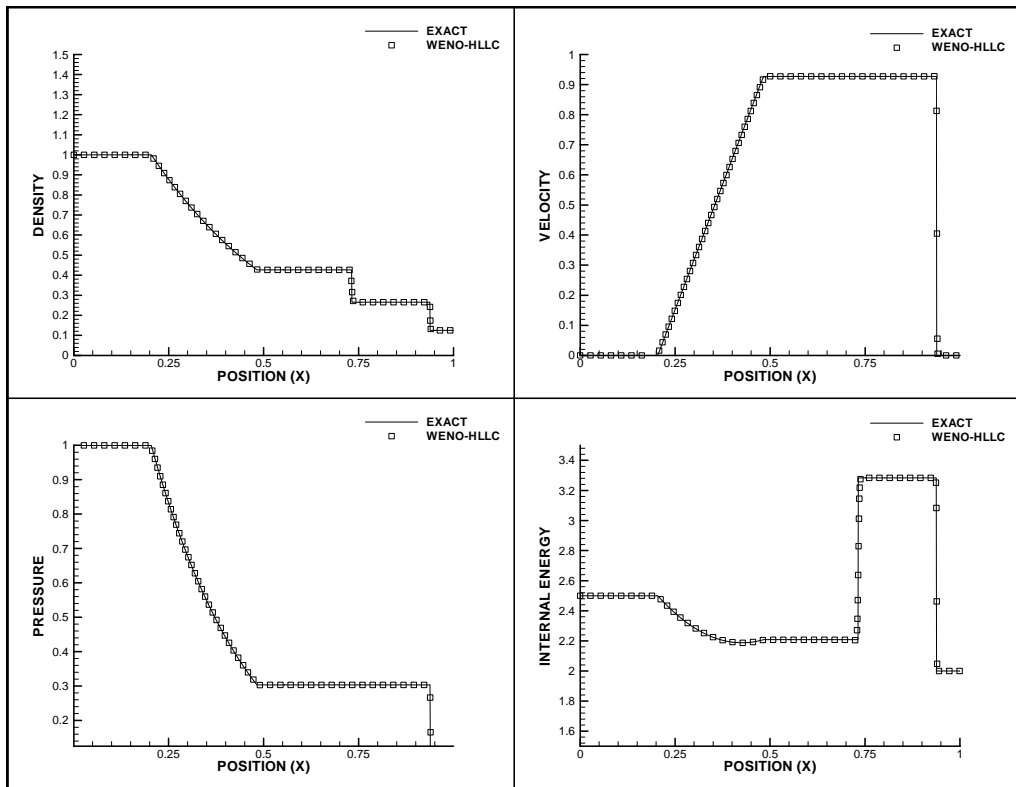


**Figure 4.2.** Solution of Sod's problem with HLLC flux at  $t=0.25$  and  $CFL=0.6$

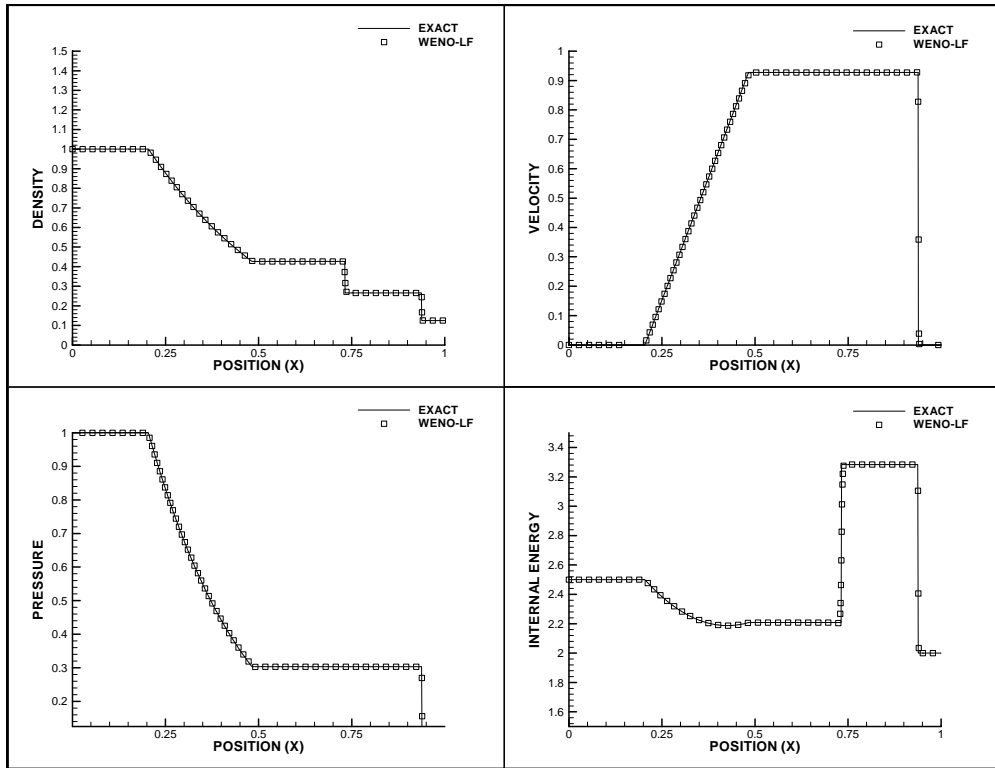


**Figure 4.3.** Solution of Sod's problem with Lax-Friedrich flux at  $t=0.25$  and  $CFL=0.6$

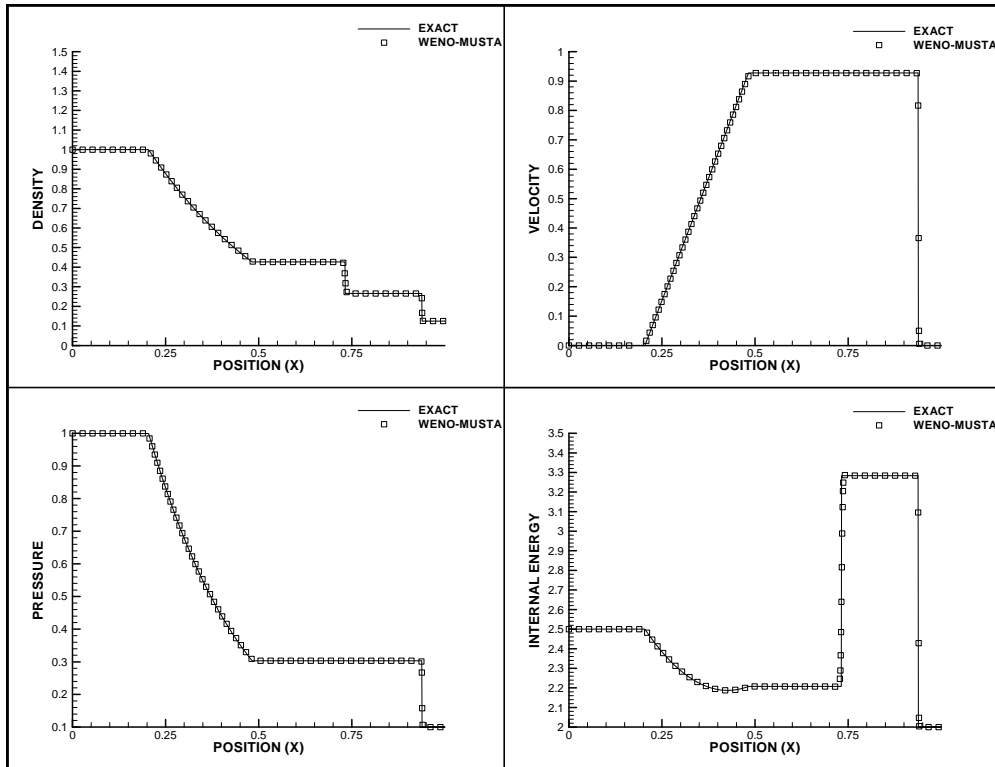


**Figure 4.4.** Solution of Sod's problem with Musta flux at  $t=0.25$  and  $CFL=0.6$  .

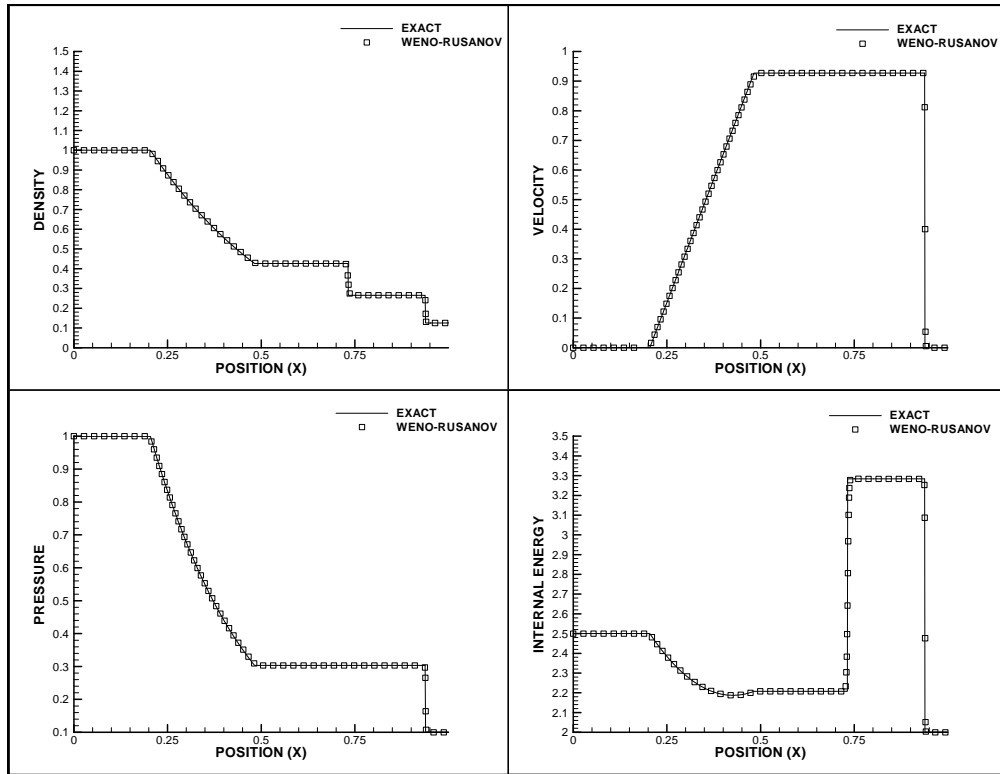


Figure 4.5. Solution of Sod's problem with Rusanov flux at  $t=0.25$  and  $CFL=0.6$ .

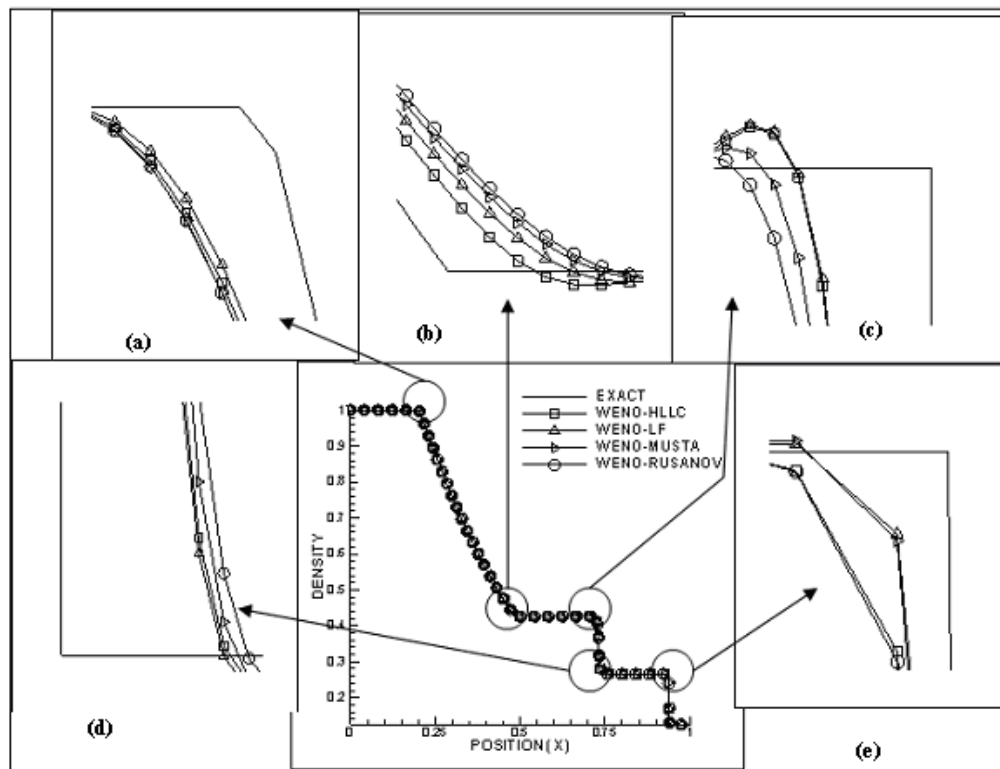


Figure 4.6. Comparison of all the fluxes for Sod's Problem

Figure 4.2-5 shows the solution of the sod's problem. Figures contain density, velocity, pressure and internal energy plots. The solution of the sod's problem consists of a left rarefaction, a contact discontinuity and a right shock wave. These figures show that all the fluxes fit the exact solution of the problem. The decreasing pressure and associated negative slopes are well predicted. In addition Figure 4.6 shows comparison of the fluxes. In at the beginning of the left rarefaction region (Figure 4.6 (a)) all the fluxes behave same while at the end of the region (Figure 4.6 (b)) It can be observed that HLLC flux is the best. Also at the contact surface regions (Figure 4.6 (c) and (d)) HLLC flux and Lax-Friedrich (LF) have more accurate results than Musta and Rusanov fluxes. In the right shock region (Figure 4.6 (e)), Musta and Lax Friedrichs fluxes have better results than other. It can be observed that HLLC flux is good at rarefaction region while Lax Friedrichs is good at shock wave region.

#### 4.1.3. The Lax 's Problem

For the Sod's problem the Riemann Type initial data is defined as;

$$Q_L = \begin{bmatrix} \rho_L \\ u_L \\ P_L \end{bmatrix} = \begin{bmatrix} 0.445 \\ 0.698 \\ 3.528 \end{bmatrix}$$

$$Q_R = \begin{bmatrix} \rho_R \\ u_R \\ P_R \end{bmatrix} = \begin{bmatrix} 0.500 \\ 0.000 \\ 0.571 \end{bmatrix}$$

This problem is again investigated with Finite Volume WENO scheme with different fluxes. Results can be seen at Figures 4.7-11

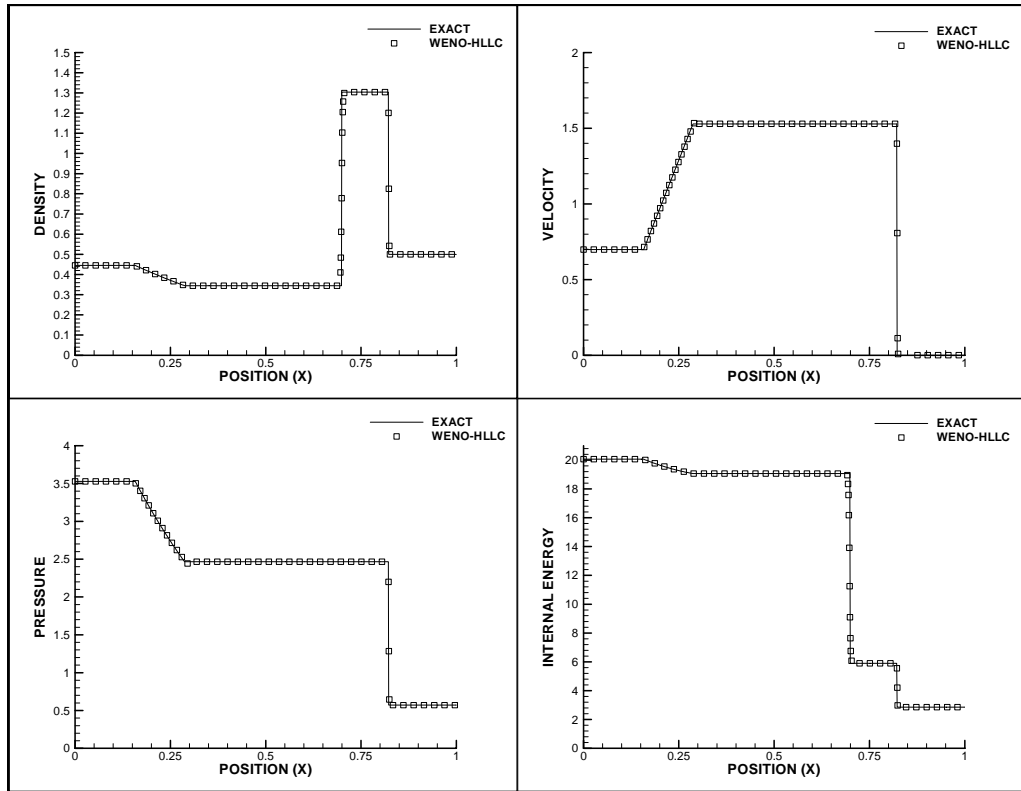


Figure 4.7. Solution of Lax's problem with HLLC flux at  $t=0.13$  and  $CFL=0.6$ .

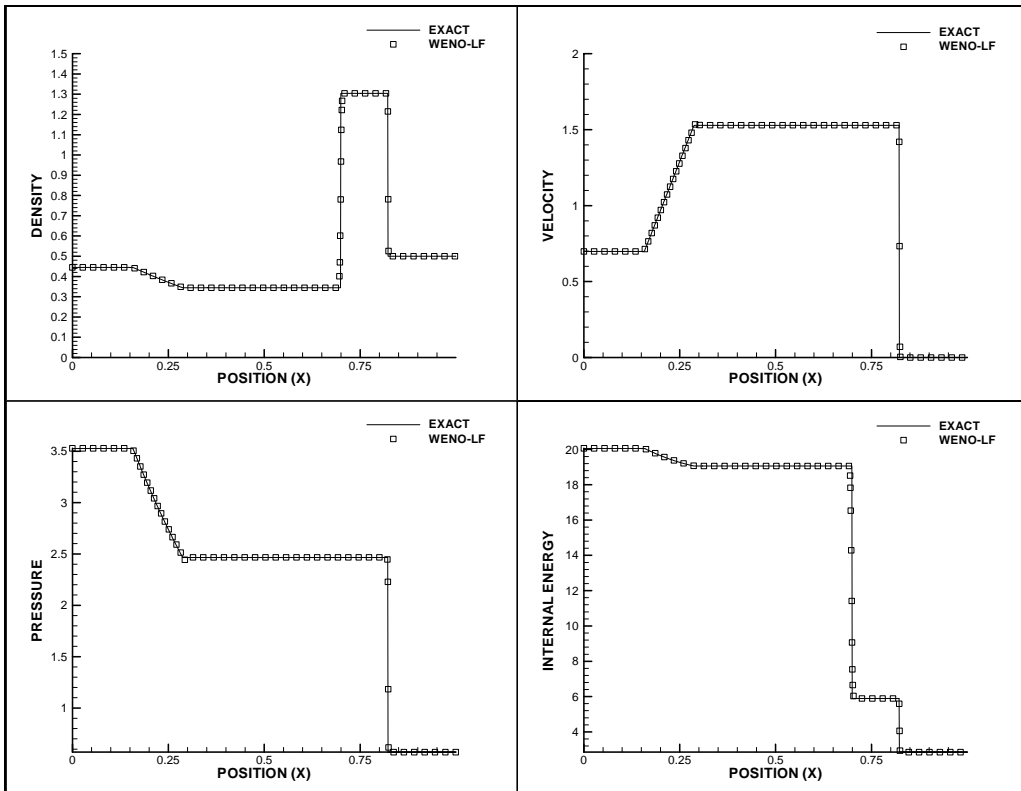
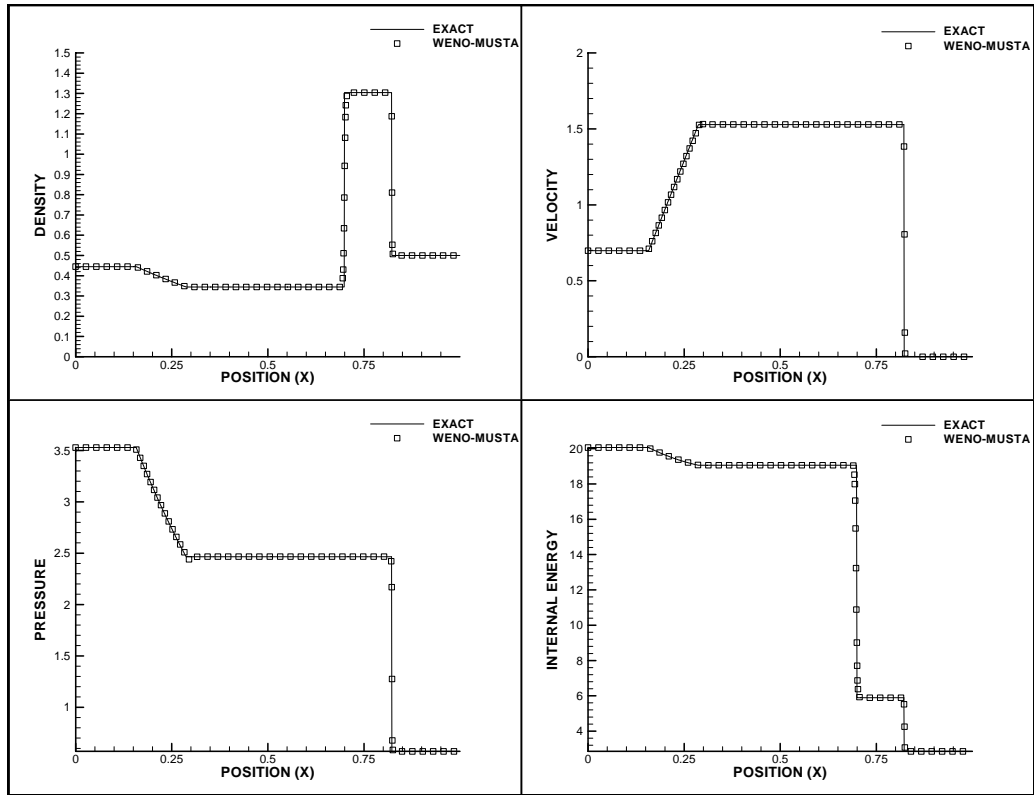
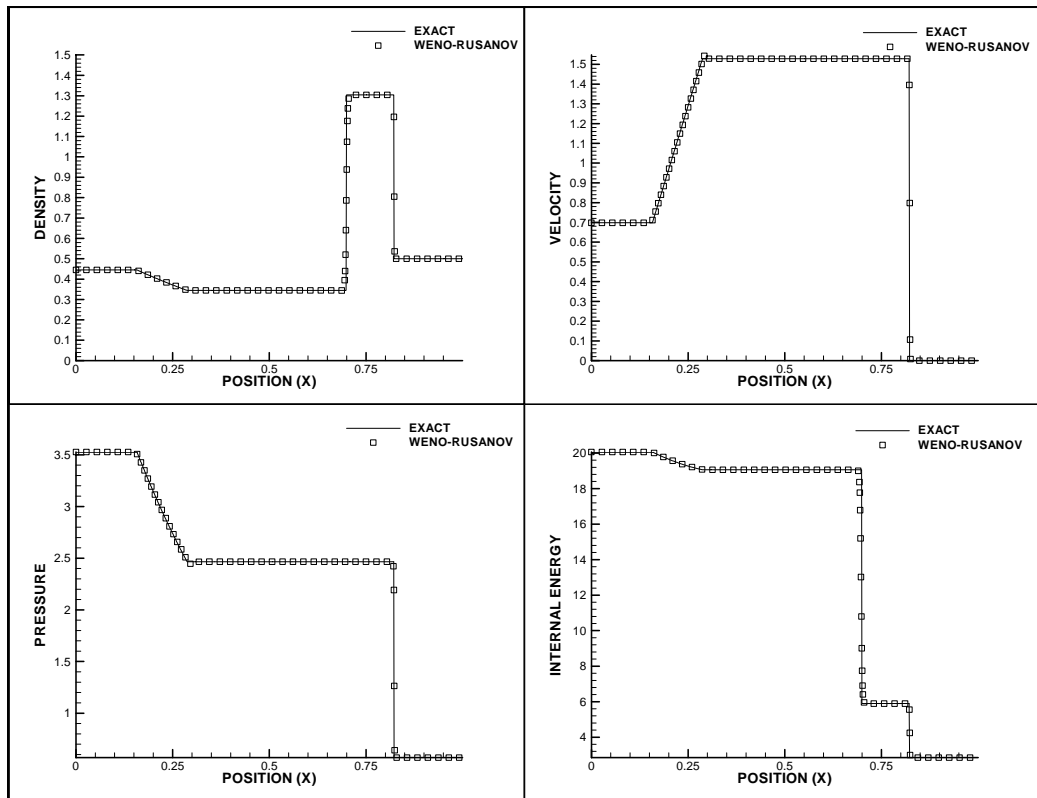


Figure 4.8. Solution of Lax's problem with Lax-Friedrich flux at  $t=0.13$  and  $CFL=0.6$ .



**Figure 4.9.** Solution of Lax's problem with Musta flux at  $t=0.13$  and  $CFL=0.6$ .



**Figure 4.10.** Solution of Lax's problem with Rusanov flux at  $t=0.13$  and  $CFL=0.6$ .

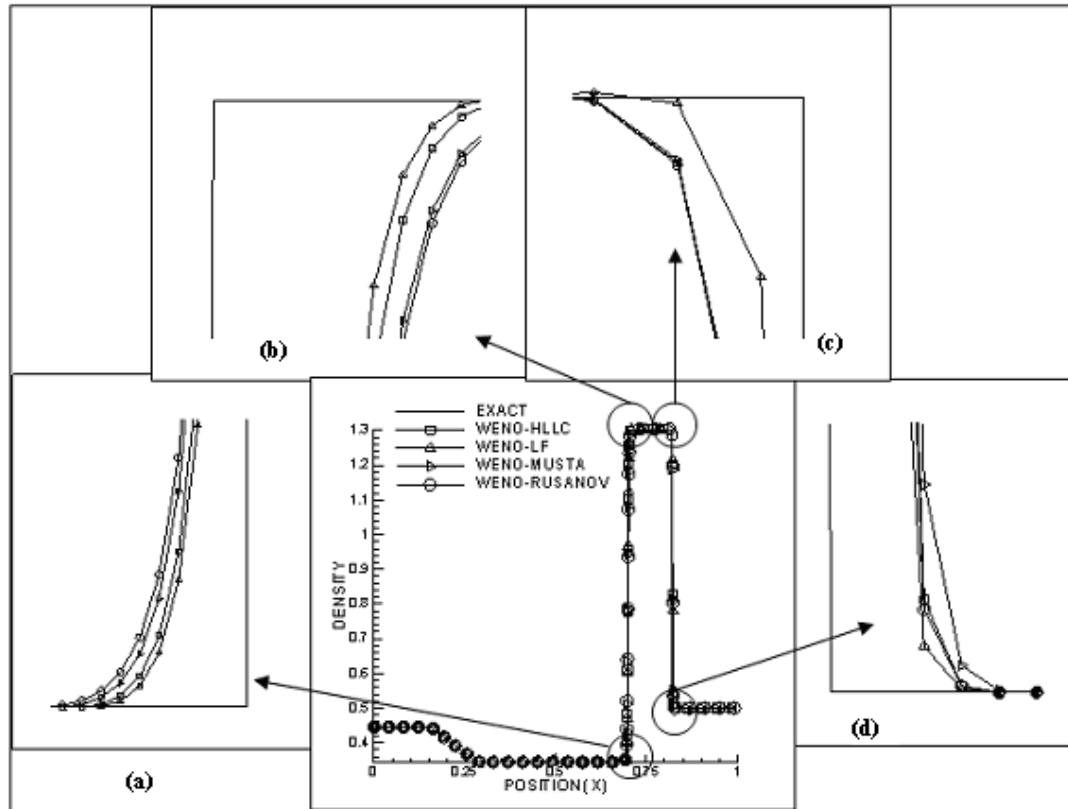


**Figure 4.11.** Comparison of all the fluxes for Lax's Problem

Figure 4.7-10 shows the solution of the Lax's problem. Figures contain density, velocity, pressure and internal energy plots. This problem is a very severe test problem with sharp density gradients increase and decrease. The solution of the Lax's problem consists of a left rarefaction, a contact discontinuity and a right shock wave. These figures show that all the fluxes fit the exact solution of the problem. In addition, Figure 4.11 shows a comparison of the fluxes. In the rarefaction fan, all the fluxes behave the same. Due to the short rarefaction region, the behaviour of the HLLC flux cannot be observed clearly. But the difference in the fluxes can be seen at the contact end and shock wave regions. In the beginning of the contact region (Figure 4.11 (a)), Lax-Friedrich and HLLC fluxes give more accurate results. Also at the end of the contact region (Figure 4.11 (b)), Lax-Friedrich flux is becoming more accurate than others. As stated before, in shock wave regions (Figure 4.6 (c) and (d)), Lax-Friedrich Flux is the best.

## 4.2 Two Dimensional Results

The First 2-D problem is Double Mach Reflection problem . The second one is the 2-D channel problem. Also in this problem Grid refinement study is carried out. The final one is the 2-D turbomachinery cascade problem.

In this section the contour plots of flow regions, pressure and mach number plots and the convergence history of the problems are showed. The convergence is calculated by the logarithm of the max. Residual.

$$Convergence = \log(|RESIDUAL_{max}|)$$

### 4.2.1 Double Mach Reflection (DMR)

This is a standart test case problem for high resolution schemes and first introduced by Woodward and Colella [32]. The flow can be set up experimentally by driving a shock down a tube which contains a wedge . At first the simple planar shock meets the walls of the tube at right angles but when wall begins a complicated shock reflection occurs [32].

This test problem involves a Mach 10 shock in air ( $\gamma=1.4$ ) which initially makes  $60^\circ$  angle with a reflecting wall. Also, the undisturbed air ahead of the shock has a density of 1.4 and a pressure of 1. The computational domain for this problem is chosen to be a rectangle  $[0, 4] \times [0, 1]$  (figure 4.12)

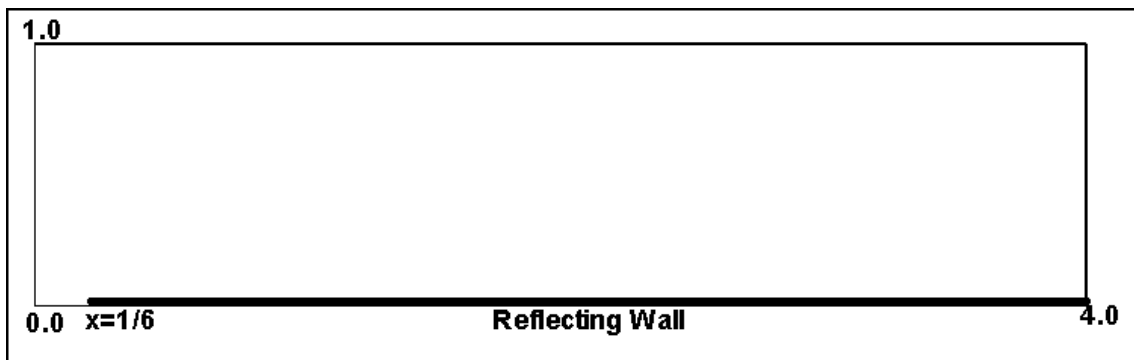


**Figure 4.12.** The Computational Domain

The reflecting wall lies along the bottom of the problem domain, starting at  $x=1/6$ . The shock makes  $60^\circ$  angle between the x-axis and extends to the top of the

problem domain at  $y=1$ . The short region from  $x=0$  and  $x=1/6$  along the bottom boundary at  $y=0$  always assigned values for the initial post-shock flow. This flow conditions are calculated by Rankine-Hugoniot equations [33]. That boundary condition attaches the reflected shock to the lower wall. Initially, the left side of the shock is also assigned values for post-shock flow whereas the right side of the shock is assigned values to enable all gradients zero. The values along the top boundary are set to give the exact motion of initial 10 Mach shock. That is boundary is assigned to values which does not dissipate the initial  $60^\circ$  incoming 10 Mach shock.

For this test problem two different sizes of the grids are tested. One of them is with 120 x 30 sizes where the other one is with 480 x 120 sizes. Solutions are obtained with same CFL number ( $CFL=0.6$ ) and at time  $t=0.2$ .

### Results with 120 x 30 Grid sizes

The results of four fluxes for 120x30 grid size are presented. The computational domain and the mesh used in calculations can be seen at figure 4.13. The mesh is uniform with  $\Delta x=\Delta y=1/30$ . Near this domain ghost cells are used in computations. They are used with symmetric type boundary conditions. Density plots can be seen in figures 4.14.

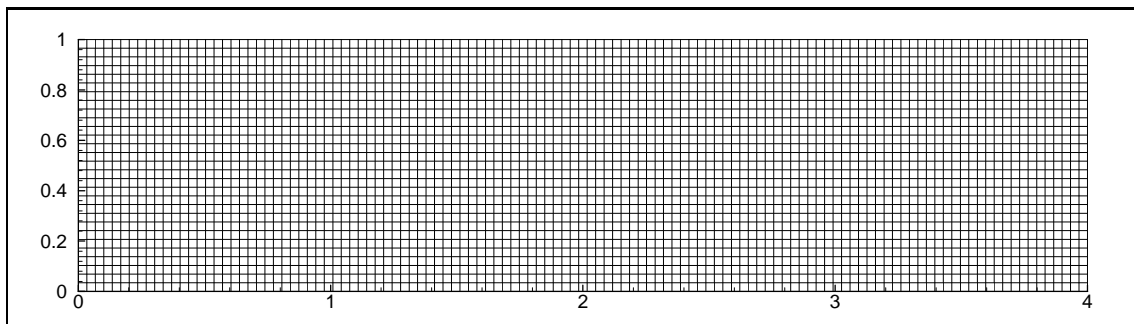
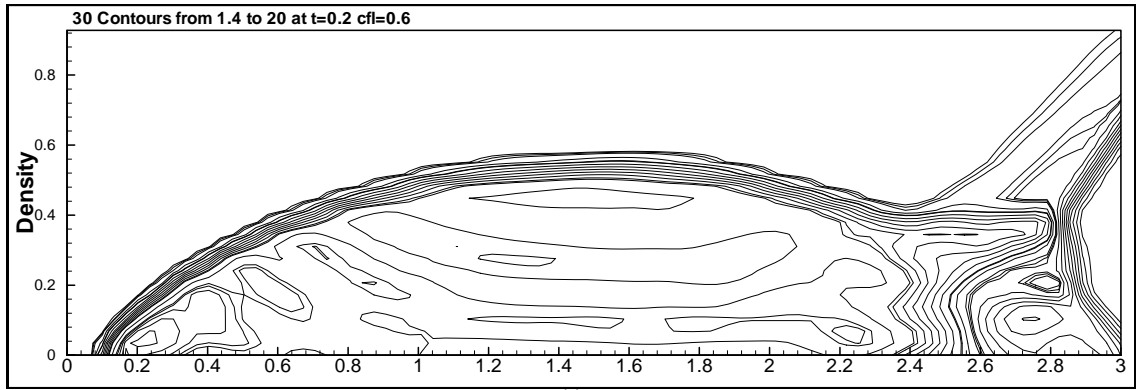
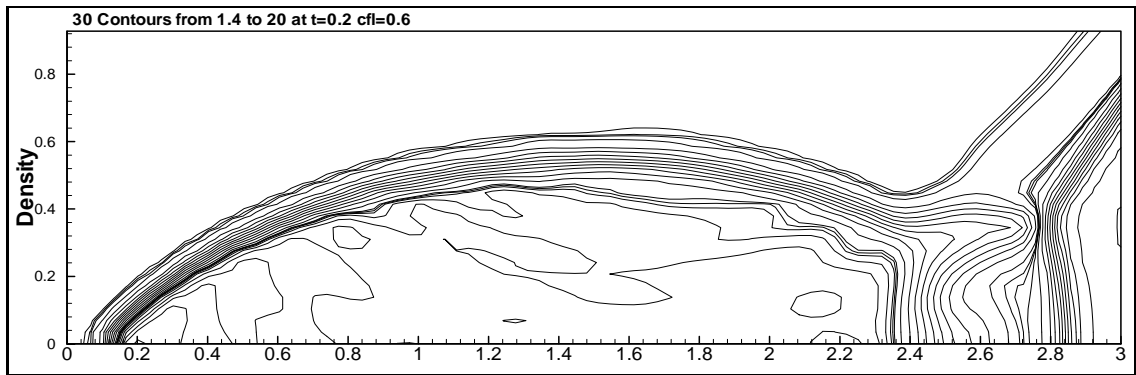


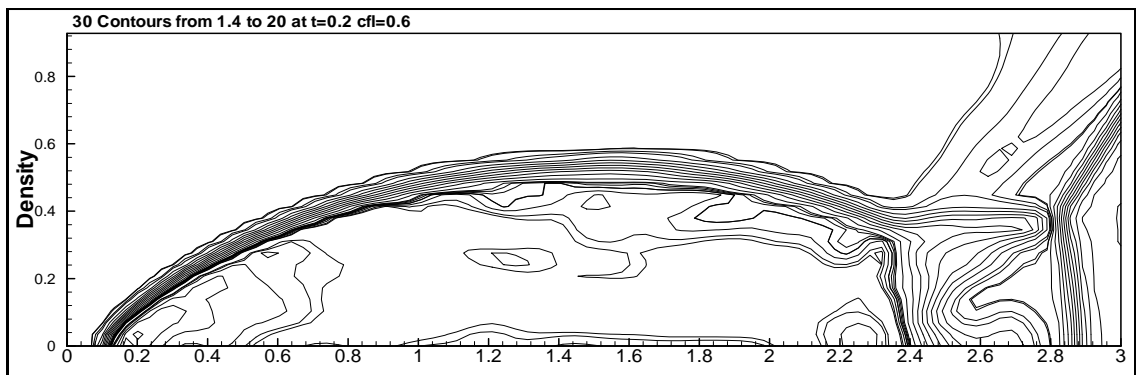
**Figure 4.13.** The computational domain and grid used in computations



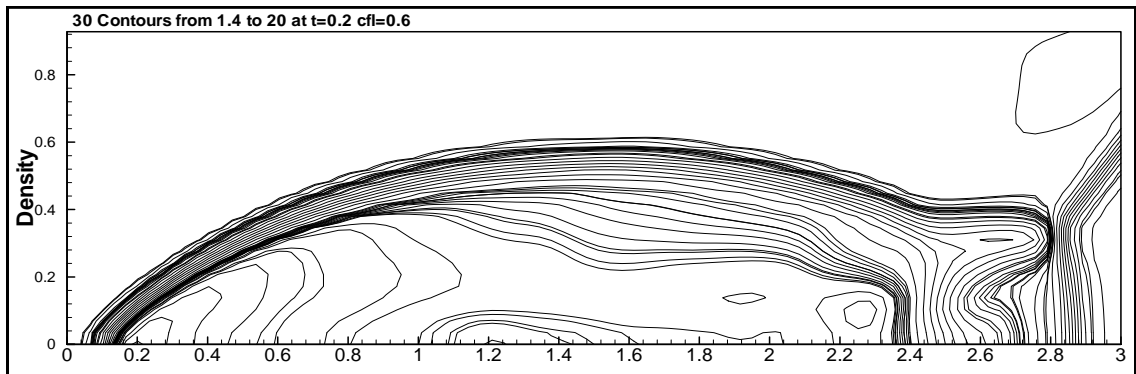
(a)



(b)



(c)



(d)

**Figure 4.14.** The Result of DMR problem with 120x30 grid size: (a) HLLC Flux, (b) Lax-Friedrich Flux, (c) WENO5 Flux and (d) Rusanov flux

This is a test problem which clearly shows the resolution of the scheme. As can be observed from the figure 4.14 the HLLC flux (figure 4.14 (a)) and musta flux (figure 4.14 (c)) shows higher resolution than other flux algorithms. Also, It is noted that appearance of the Kelvin-Helmholtz instability (rolling) of the slip surface is physically unstable features of the flow. That depends on the mesh and the scheme used. For the same sizes of the meshes the schemes can be compared by that region. That region shows the numerical dissipation of the scheme. The more instability means less numerical dissipation when same mesh sizes considered. Therefore, The HLLC flux shows the least numerical dissipation. Whereas the Lax-Friedrichs flux shows the most numerical dissipation.

### Results with 480 x 120 Grid sizes

In this section, the results of four fluxes for 480x120 grid sizes are presented. The computational domain and the mesh used in calculations can be seen at figure 4.15. The mesh is uniform with  $\Delta x = \Delta y = 1/120$ . Also density plots can be seen in figures 4.16. and figures 4.17.

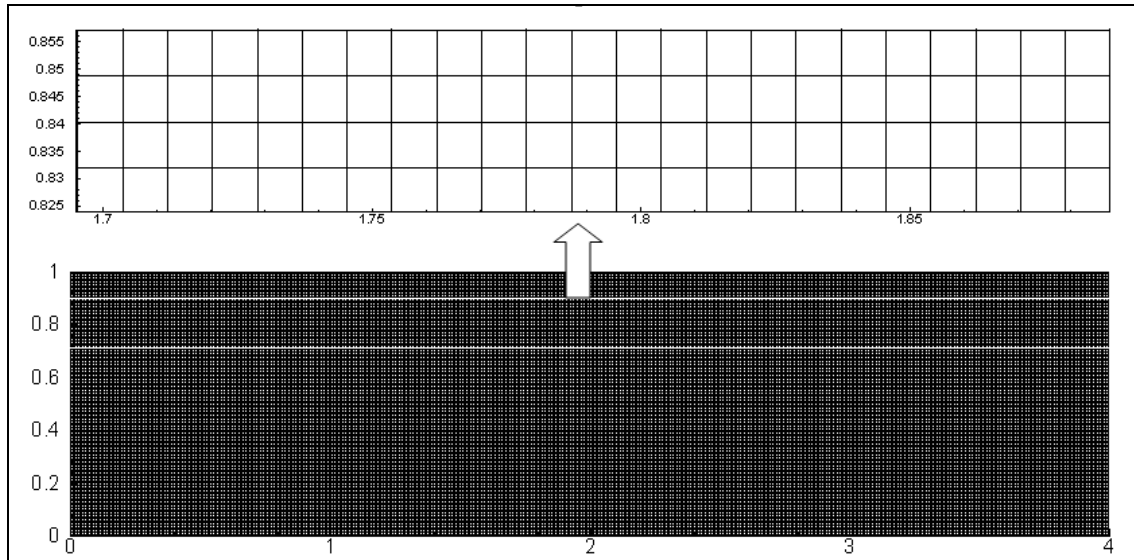
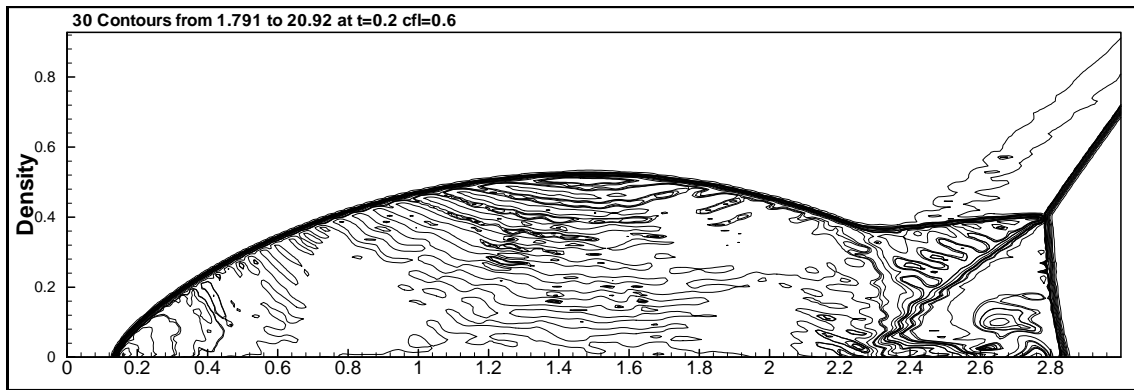
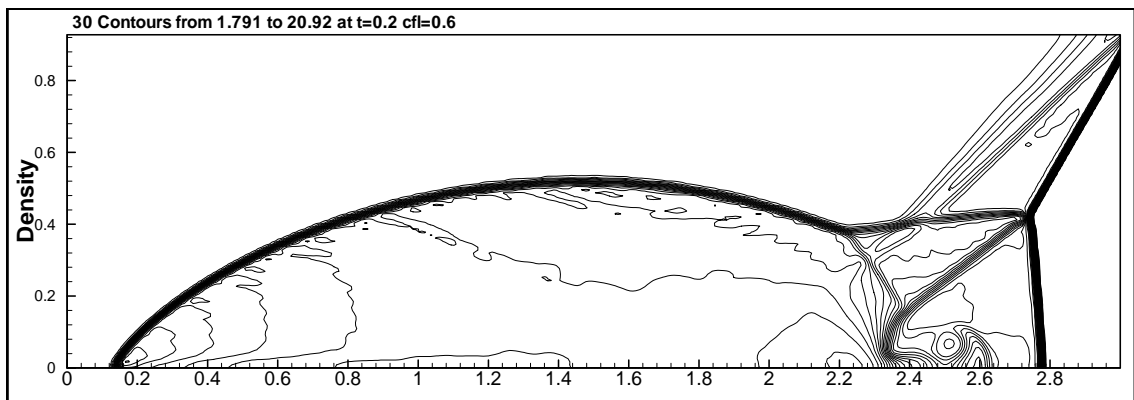


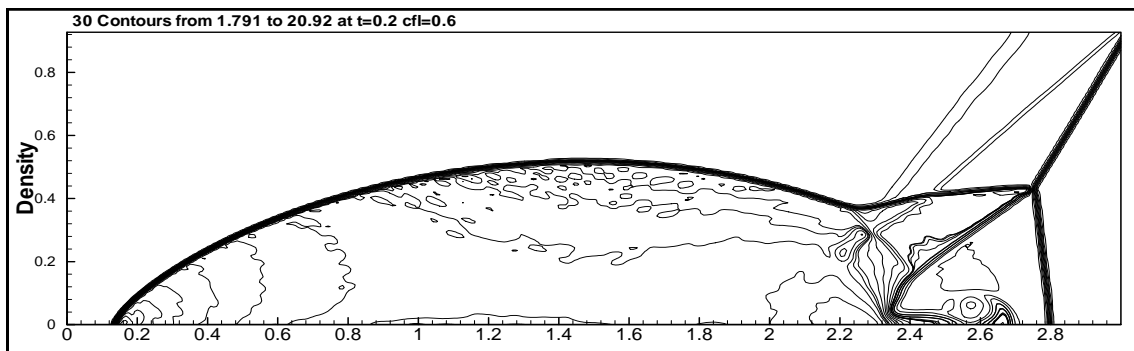
**Figure 4.15.** The computational domain and grid used in computations



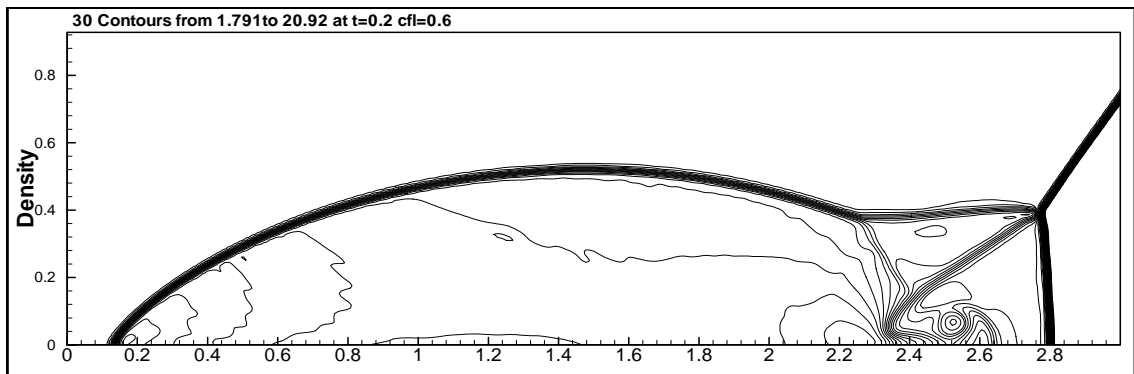
(a)



(b)



(c)



(d)

**Figure 4.16.** The Result of DMR problem with  $480 \times 120$  grid size (a) HLLC Flux, (b) Lax-Friedrich Flux, (c) Musta Flux and (d) Rusanov flux

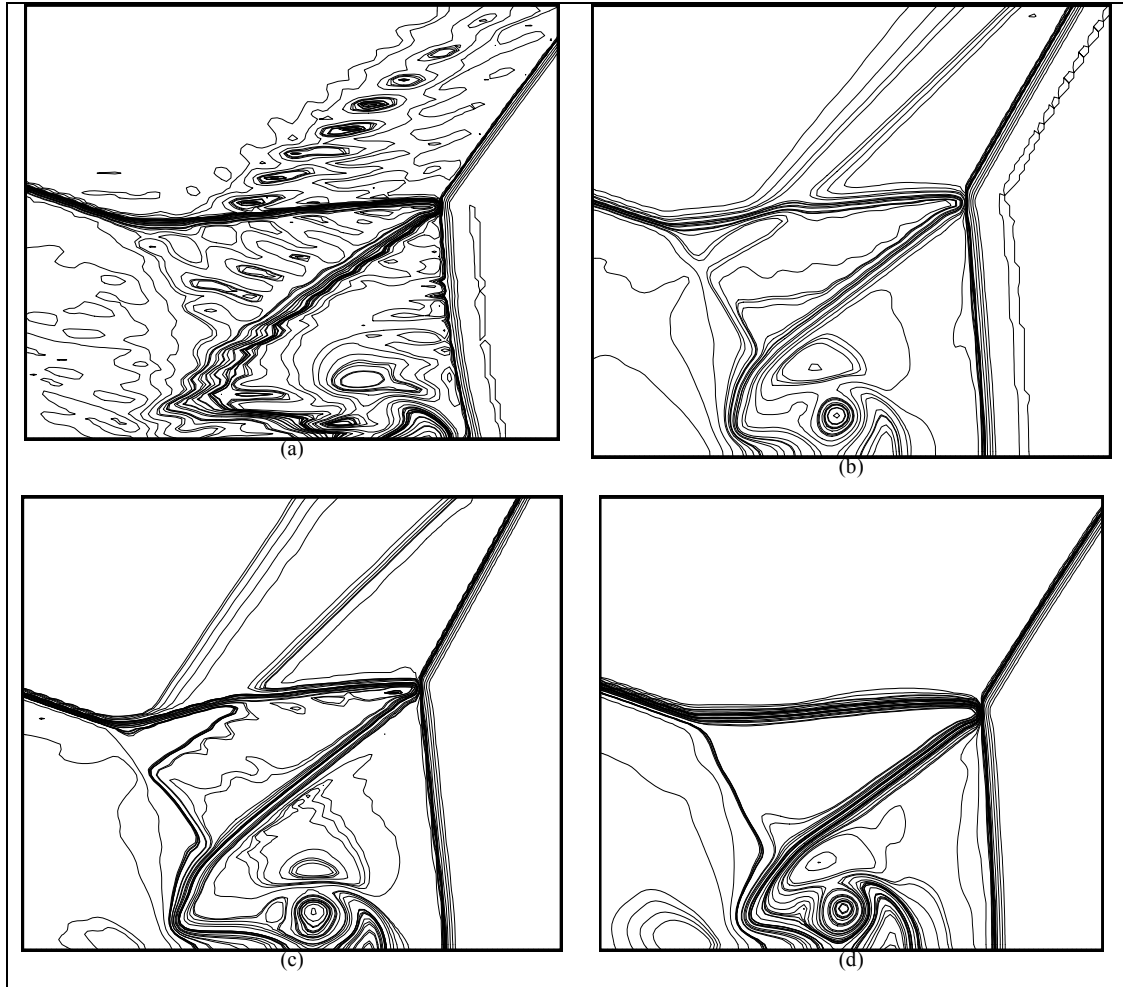


**Figure 4.17.** Zoomed area of the figure 4.16 : a) HLLC Flux, (b) Lax-Friedrich Flux, (c) Musta Flux and (d) Rusanov flux

The dependency of the problem on mesh density can easily be determined by comparing figures 4.15 and 4.16. The increase of the mesh size also does increase the instability. So that increasing the mesh sizes increase the resolution of the problem. Closer views of the instabilities are considered for higher mesh sizes. (Figure 4.17.) Some comments can be made on numerical scheme. As concluded before HLLC flux has the least numerical dissipation. However it reflects the most oscillatory behaviors. After HLLC Musta scheme has less numerical dissipation than the others. Most dissipative scheme is the Lax-Friedrich scheme.

## 4.2.2 Supersonic Channel Flow

Supersonic channel flow problem has a more elaborated domain than Double Mach Reflection problem. This problem is defined in [29]. The supersonic channel flow domain is showed at figure 4.18.

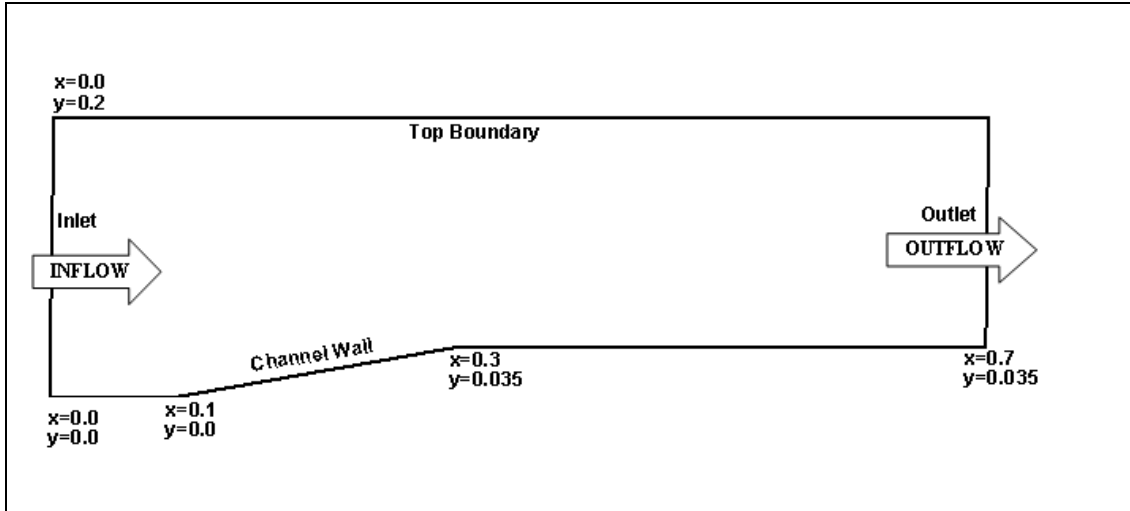


**Figure 4.18.** Geometry of the channel

The existence of the compression and expansion corners will lead to the formation of oblique shock and expansion waves. The reflection and interaction of the shock and expansion waves will be illustrated in the results.

The flow enters the channel from the left at supersonic speed. The flow is assumed air (specific heat ratio  $\gamma=1.4$ ) with free stream pressure  $p=1.0$  and density  $\rho=1.0$ . The solution is obtained for  $M=2.0$ . The flow initial conditions are specified as the free stream conditions over the entire domain.

Since the flow is full supersonic for each Mach number, the properties at the inlet boundary are all assigned to the free stream values, whereas the properties at the exit boundary are extrapolated from the interior of the domain. The wall boundary condition is applied to the lower surface (channel wall) where for the upper surface (top boundary) symmetric boundary conditions are used.

For this test problem the grid refinement study is carried out. Four grids densities are used in calculations. These grids can be seen at figures 4.19 – 22.

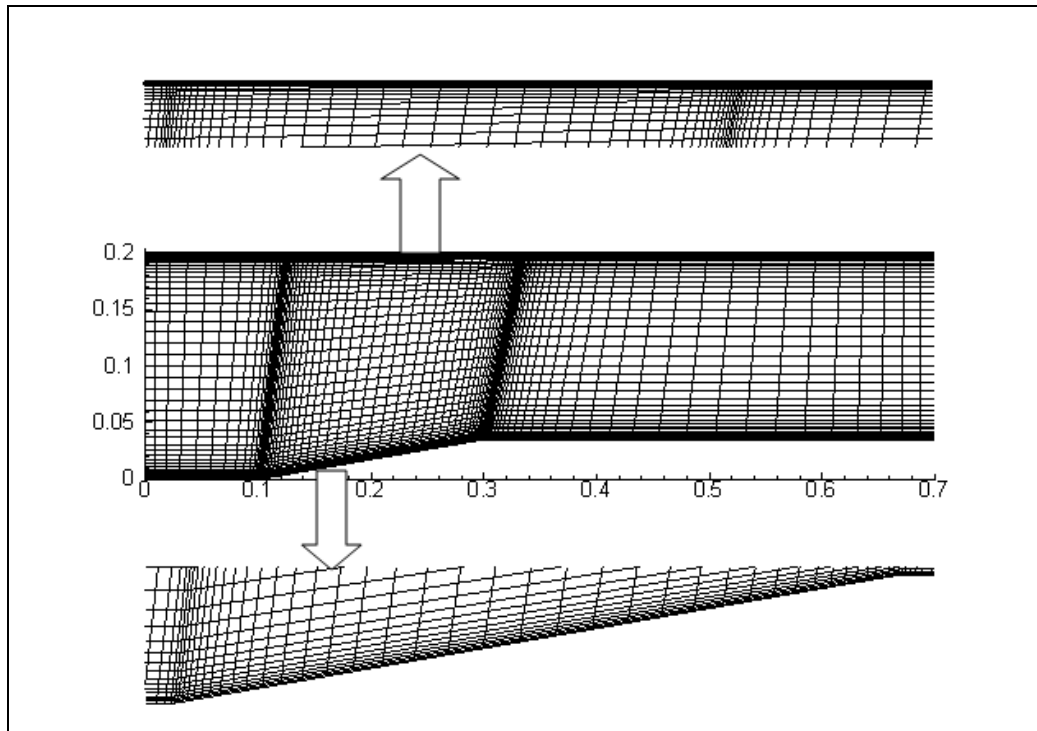


**Figure 4.19.** The Grid#1 with size 82x45

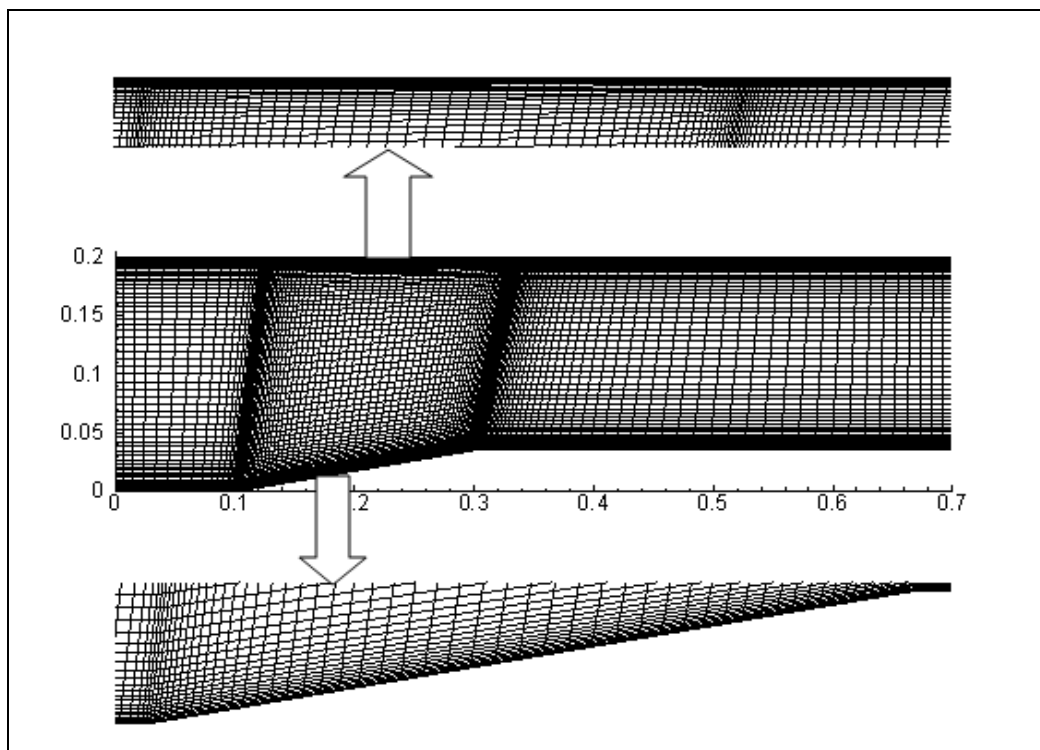


**Figure 4.20.** The Grid#2 with size 119x65

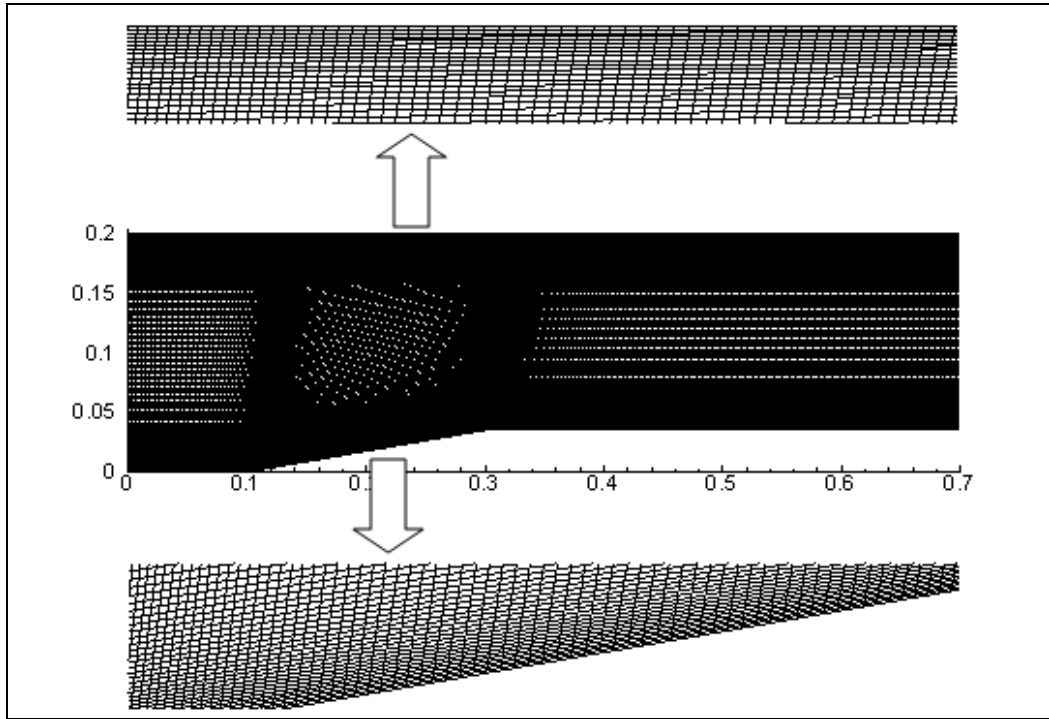


**Figure 4.21.** The Grid#3 with size 241x131

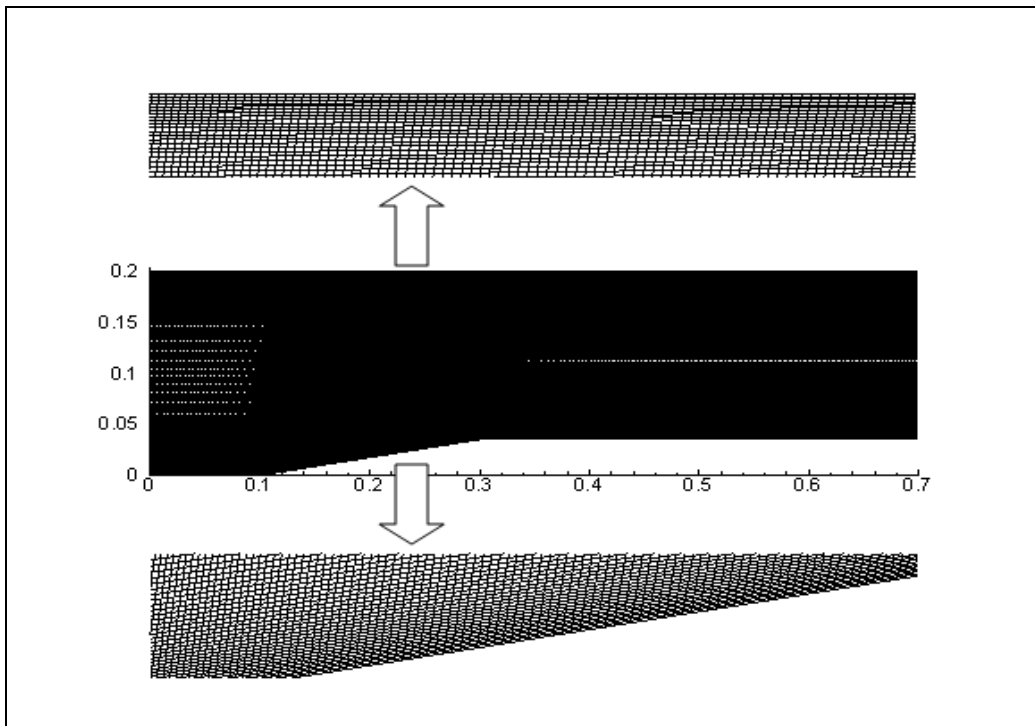


**Figure 4.22.** The Grid#4 with size 318x150

Results are obtained for four grid sizes and these results are compared. So, the results are presented for each flux with different sizes of the grid. Then, the behavior of fluxes for each grid is also presented.

#### 4.2.2.1 WENO-HLLC results

The pressure contours of the results are shown at figures 4.23-26.

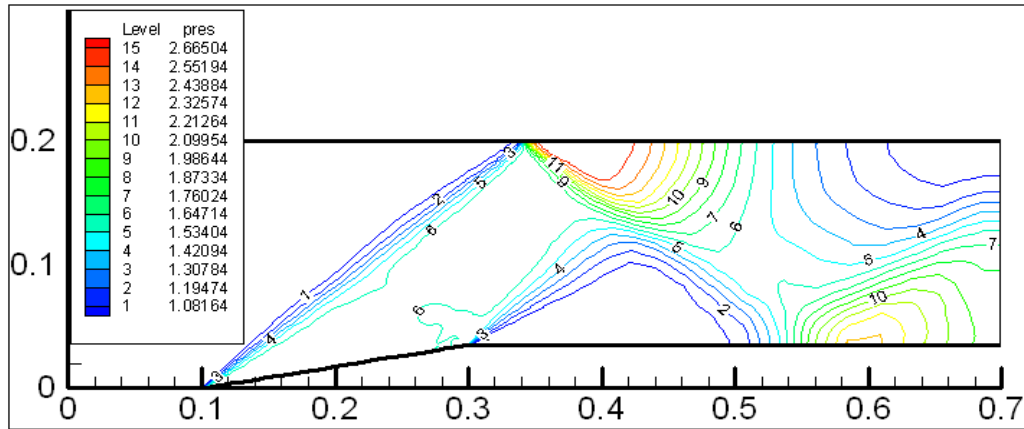


Figure 4.23. Pressure contours for grid#1 (82x45) for Weno-HLLC

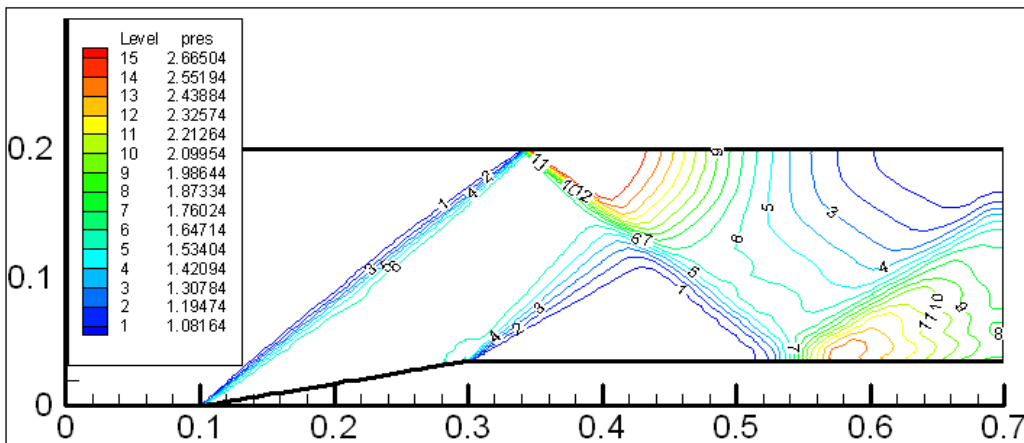
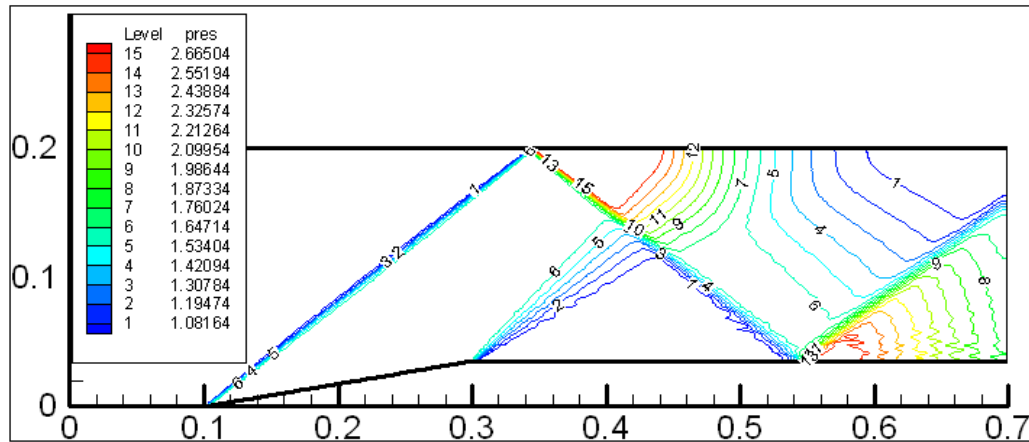
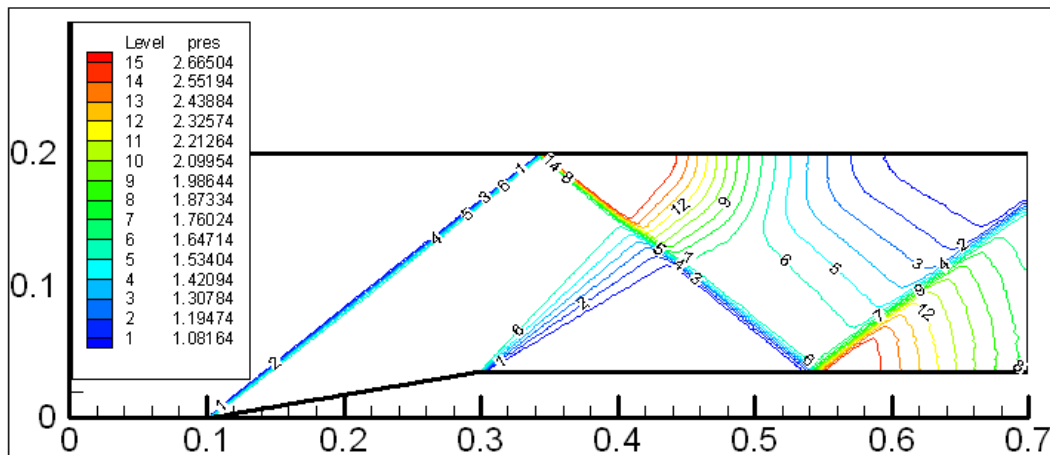


Figure 4.24. Pressure contours for grid#2 (119x65) for Weno-HLLC



**Figure 4.25.** Pressure contours for grid#3 (241x131) for Weno-HLLC



**Figure 4.26.** Pressure contours for grid#4(318x150) for Weno-HLLC

It can be observed clearly from pressure contours that the mesh size affect the resolution of the solution. At the biggest mesh size, the thinnest shock wave can be seen. However grid#3 has also good results when resolution is considered. Figure 4.27 shows the pressure distribution along the channel wall. Figure 4.28 shows the convergence histories of the results.

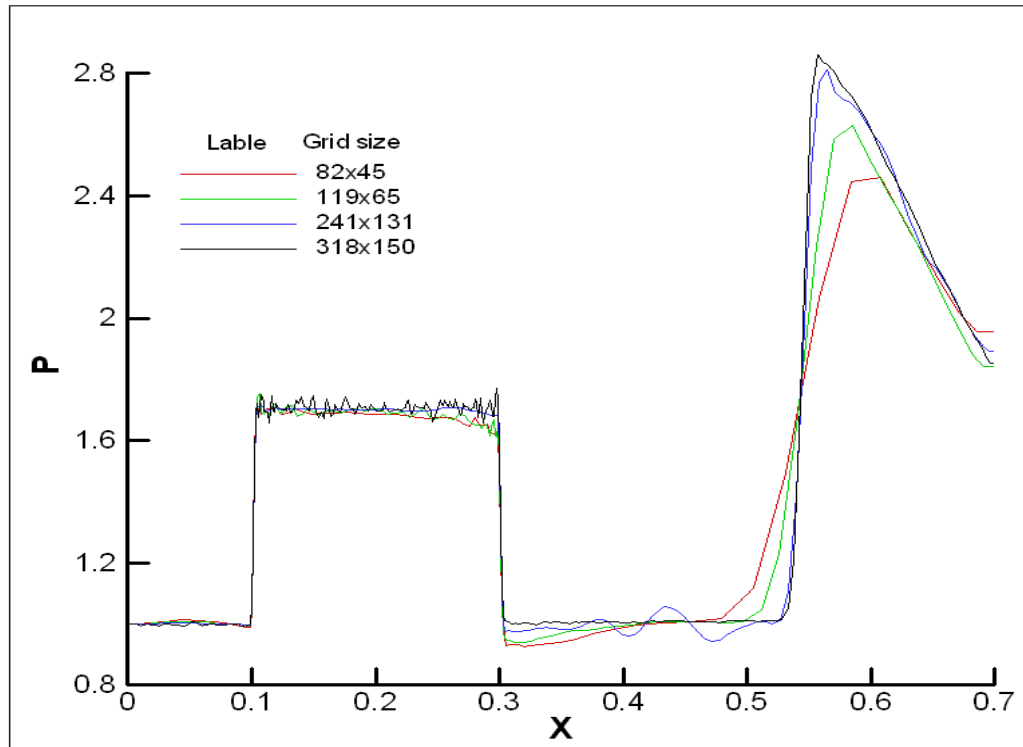


**Figure 4.27.** Pressure distribution on channel wall for Weno-HLLC

Figure 4.27 shows that when mesh size increased, the resolution is also increased but with the resolution oscillations are included to the solution. These oscillations can be damped with more grid clustering. In the grids used all the grid clustering parameters are kept constant.

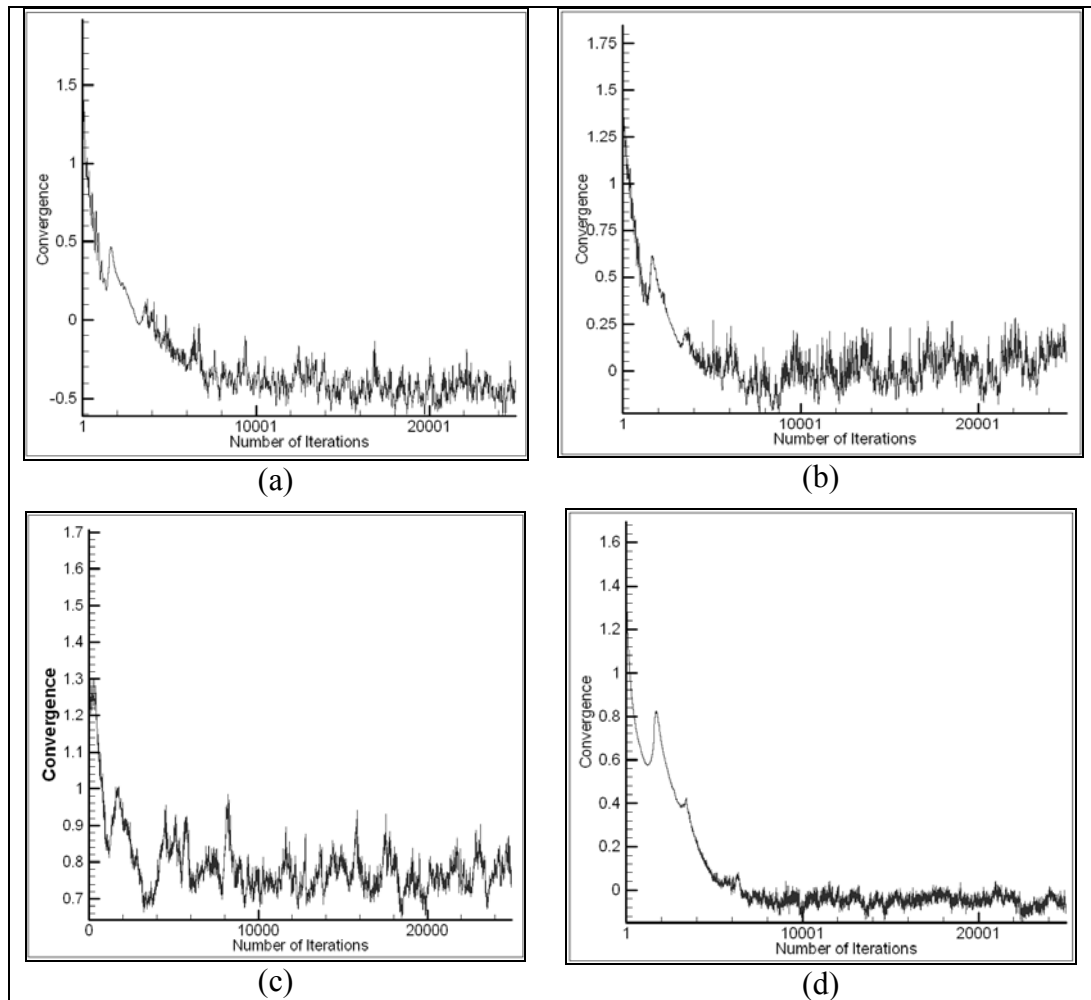


**Figure 4.28.** The convergence history of the WENO-HLLC scheme with different mesh sizes (a) Grid#1, (a) Grid#2, (a) Grid#3 and (a) Grid#4

When the convergence history of the scheme is shown in Figure 4.28. It is concluded that the scheme does not have strong convergence Maximum 1 order of convergence is obtained. This is a drawback of the WENO scheme, convergence of the WENO scheme is very poor. [1].

### 4.2.2.2 WENO-Lax-Friedrichs results

Figures 4.29-32 shows the pressure contours of the results. Figure 4.33 shows the pressure distribution along the channel wall whereas figure 4.34 shows the convergence history of the scheme.

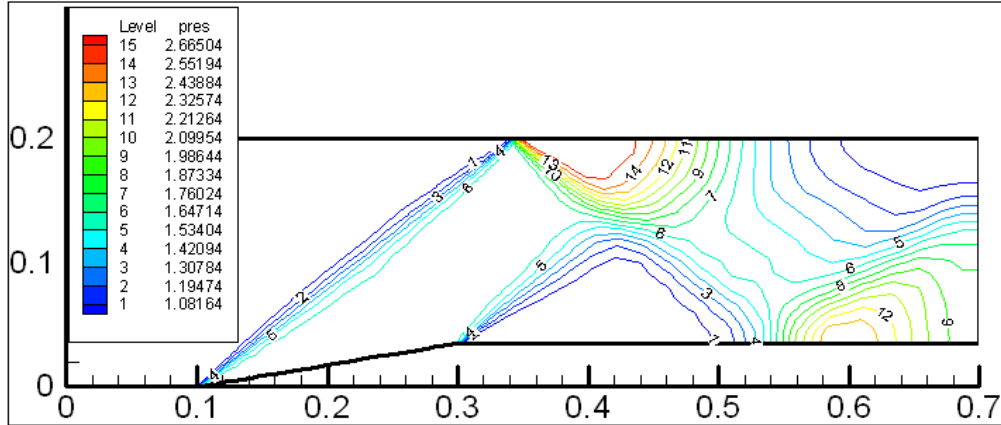


Figure 4.29. Pressure contours for grid#1 for Weno-LF

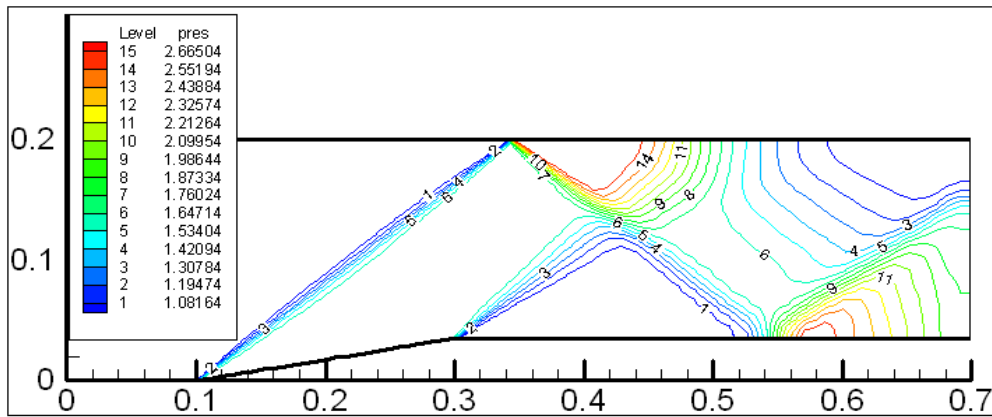


Figure 4.30. Pressure contours for grid#2 for Weno-LF

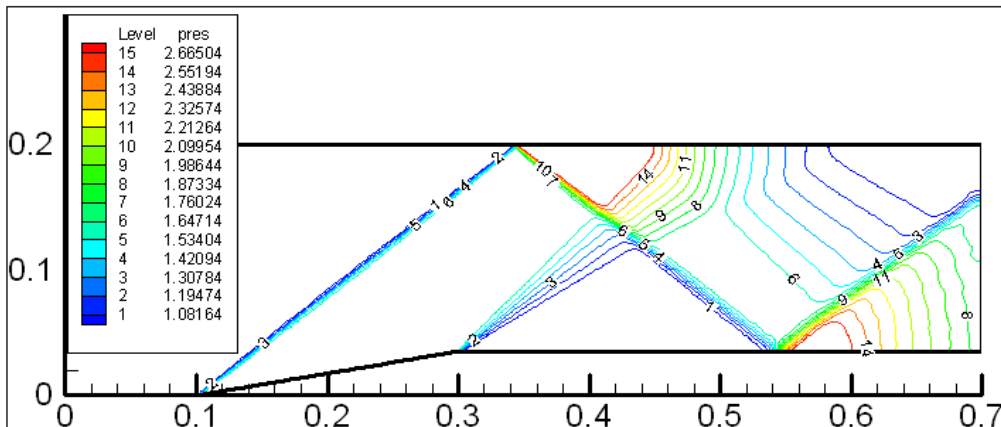
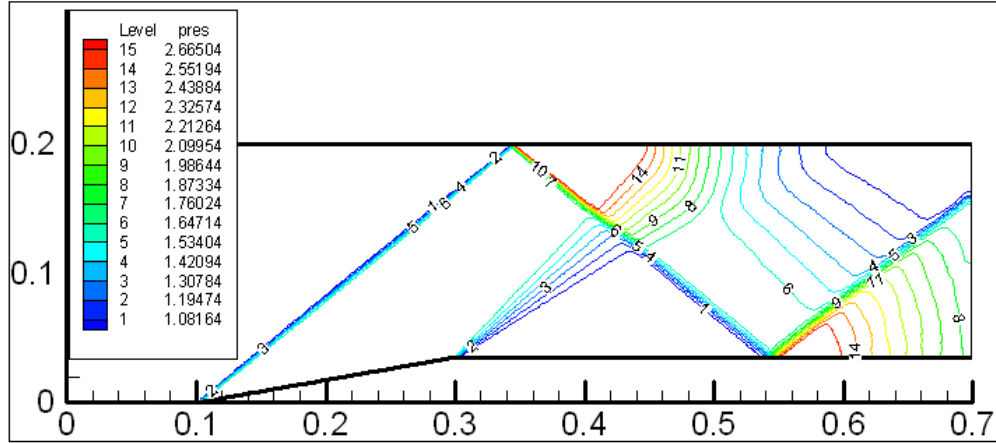
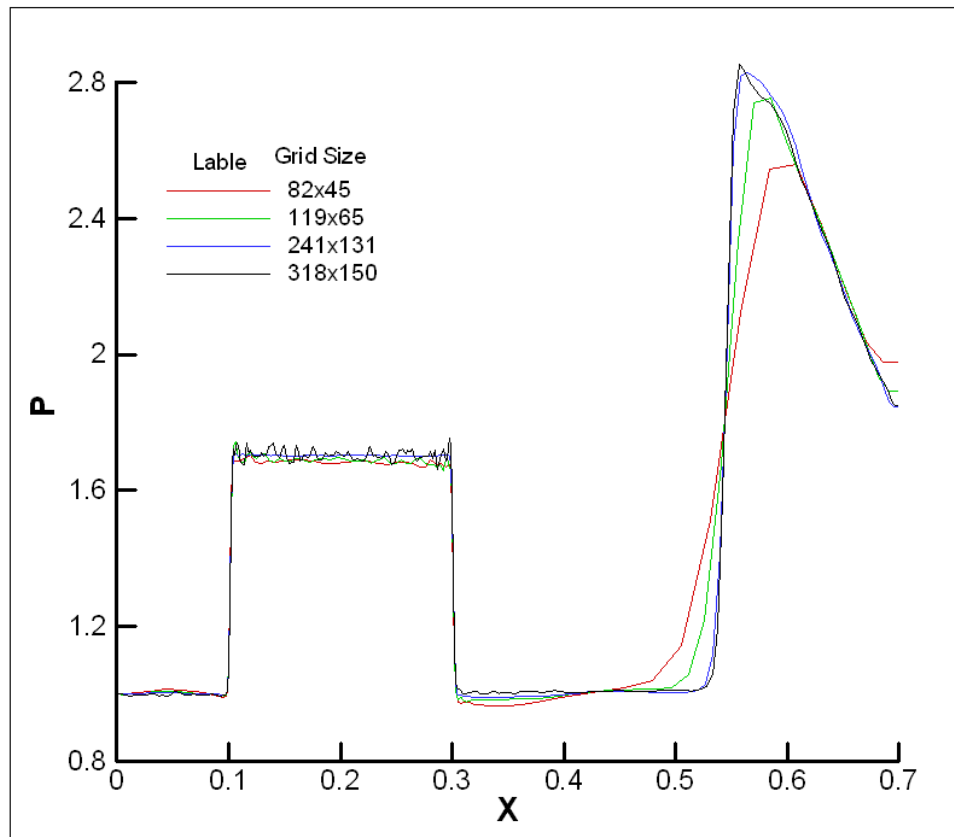


Figure 4.31. Pressure contours for grid#3 for Weno-LF



**Figure 4.32.** Pressure contours for grid#4 for Weno-LF



**Figure 4.33.** Pressure distribution on channel wall for Weno-LF

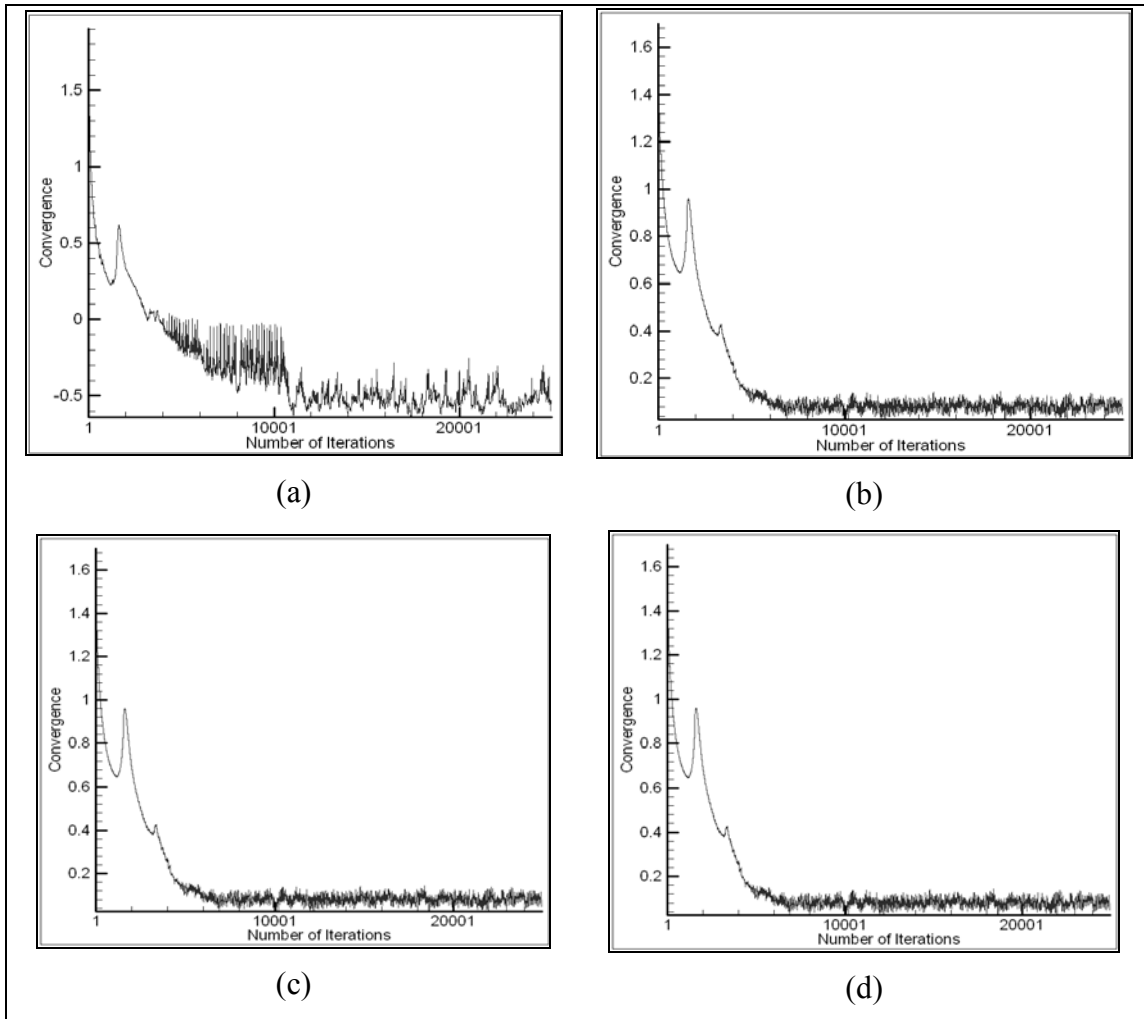


**Figure 4.34.** The convergence history of the WENO-LF scheme with different mesh sizes (a) Grid#1, (a) Grid#2, (a) Grid#3 and (a) Grid#4

When pressure contours (Figures 4.29 -32) ,and pressure distribution (Figure 4.33) are considered It is seen that Lax-Friedrich scheme is less sensitive to the mesh size than HLLC flux .Also the convergence history , figure 4.34 , shows that Lax-Friedrich converges faster than HLLC .

### 4.2.2.3 WENO-MUSTA results

Figures 4.35-38 shows the pressure contours of the results. Figure 4.39 shows the pressure distribution along the channel wall whereas figure 4.40 shows the convergence history of the scheme.

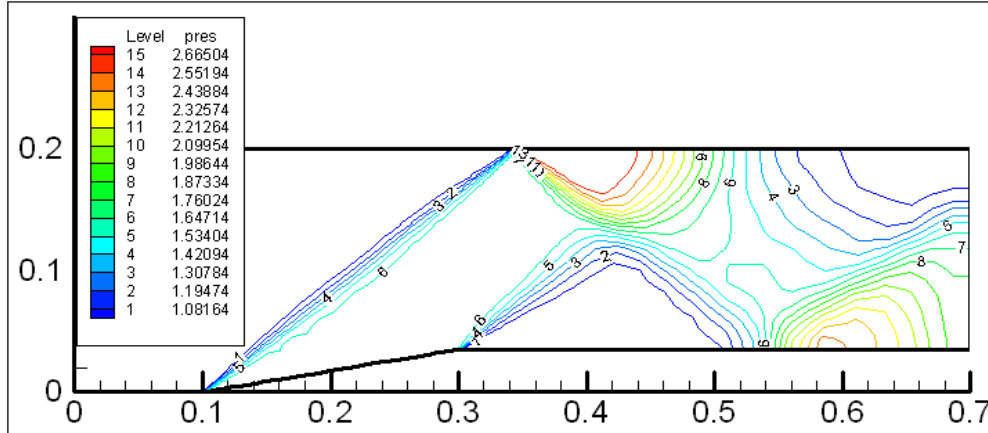


Figure 4.35. Pressure contours for grid#1 for Weno-MUSTA

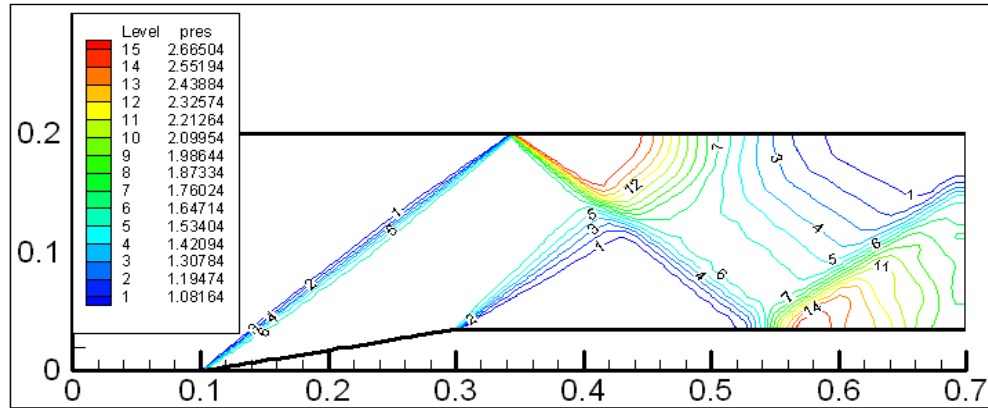


Figure 4.36. Pressure contours for grid#2 for Weno-MUSTA

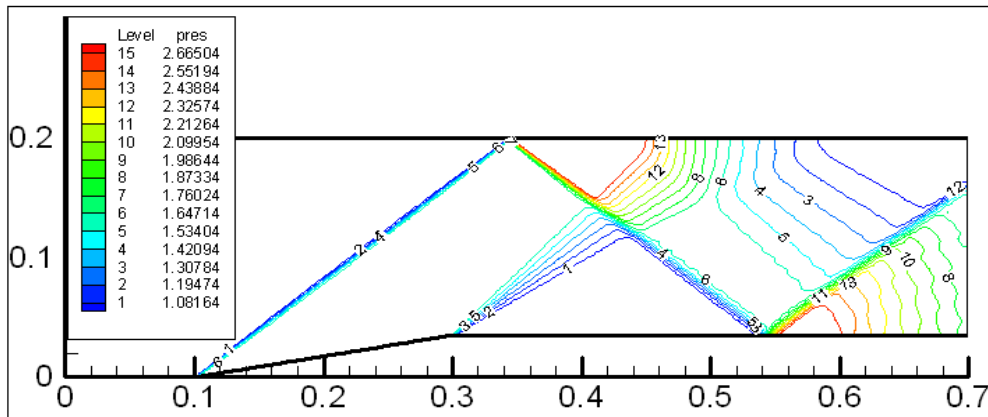
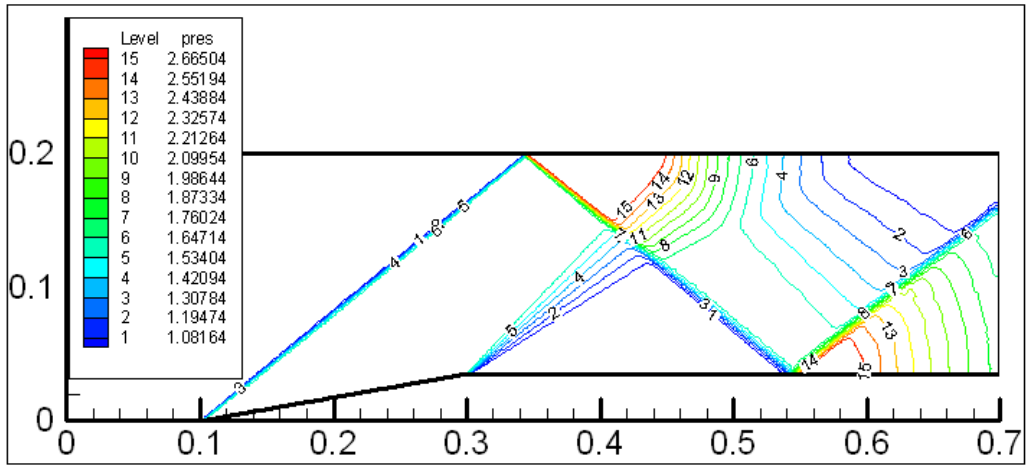
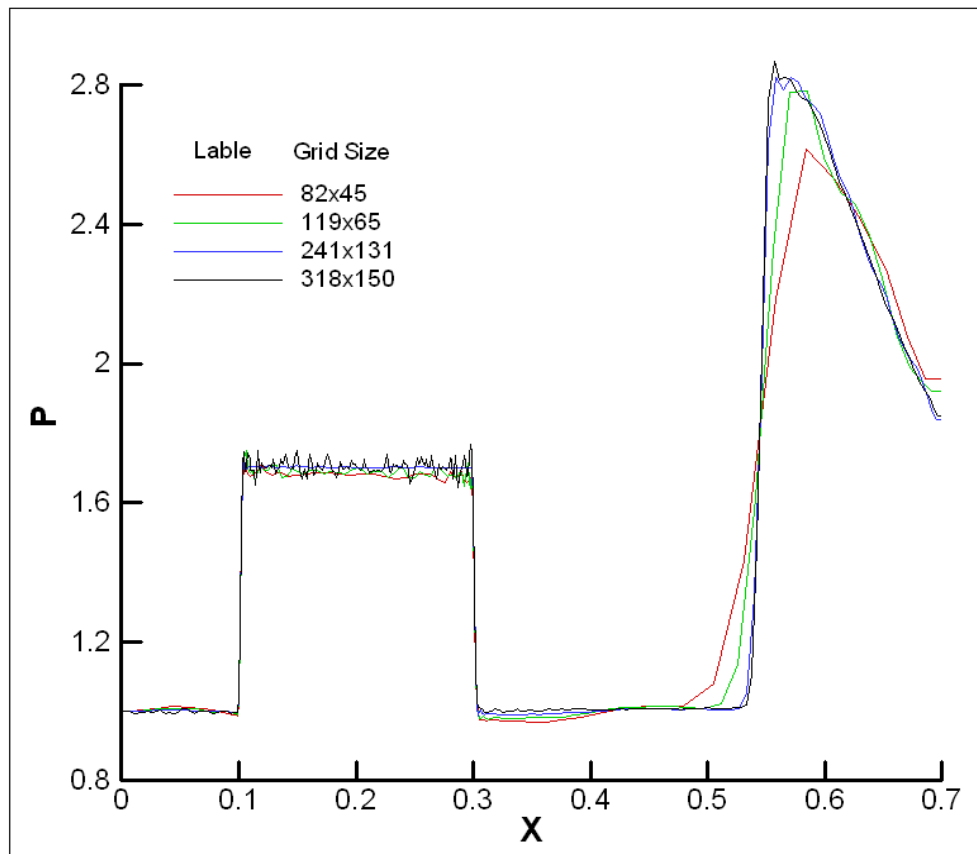


Figure 4.37. Pressure contours for grid#3 for Weno-MUSTA



**Figure 4.38.** Pressure contours for grid#4 for WENO-MUSTA



**Figure 4.39.** Pressure distribution on channel wall for WENO-MUSTA

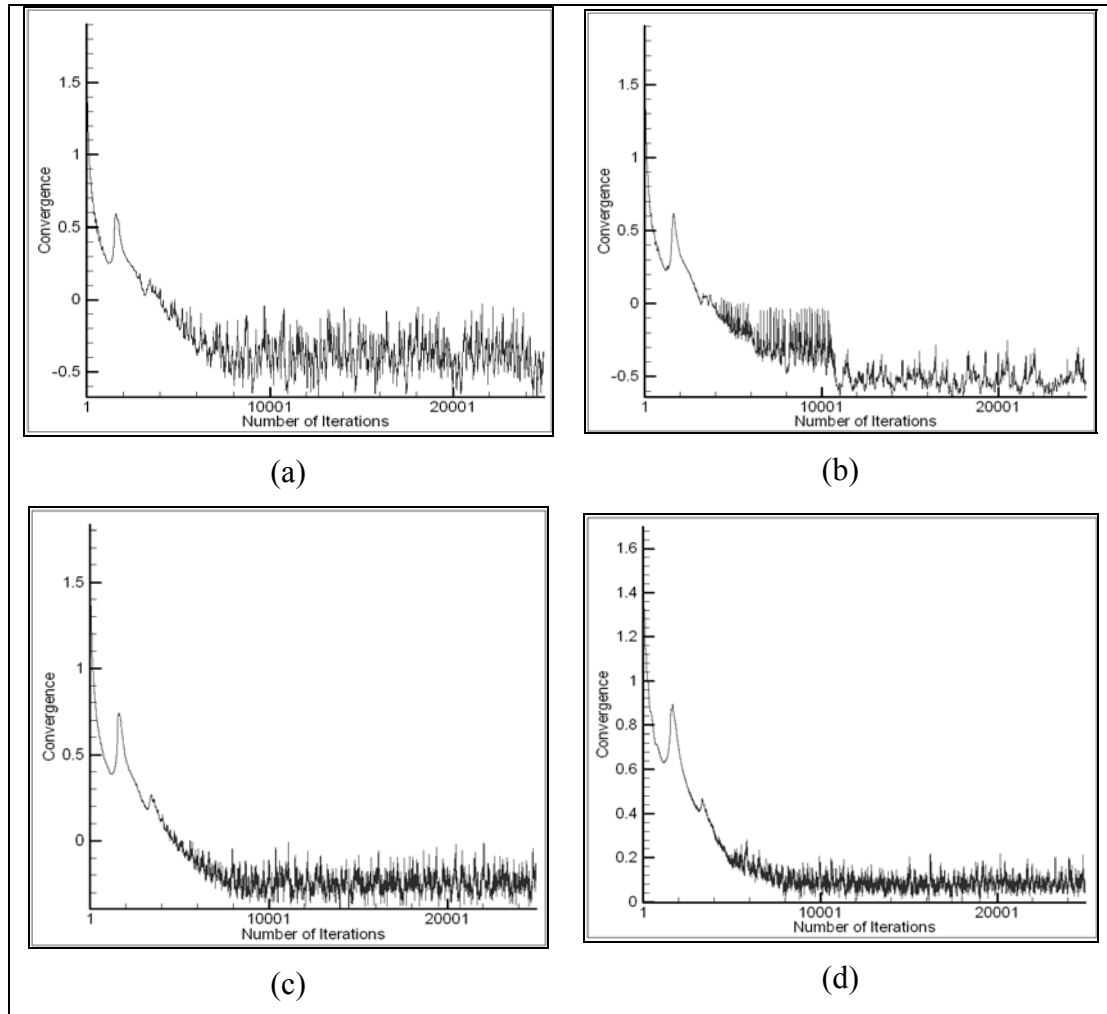


**Figure 4.40.** The convergence history of the WENO-MUSTA scheme with different mesh sizes (a) Grid#1, (a) Grid#2, (a) Grid#3 and (a) Grid#4

The figures showed that WENO-MUSTA scheme does also behaves like the other schemes (HLLC and MUSTA). However, Musta flux bring much oscillations to the solutions compared with Lax-Friedrichs flux. The convergence histories are approximately same. Musta flux hardly converges for coarse grids whereas Lax-Friedrichs flux converges well.

#### 4.2.2.4 WENO-RUSANOV results

Figures 4.41-44 shows the pressure contours of the results. Figure 4.45 shows the pressure distribution along the channel wall whereas figure 4.46 shows the convergence history of the scheme.

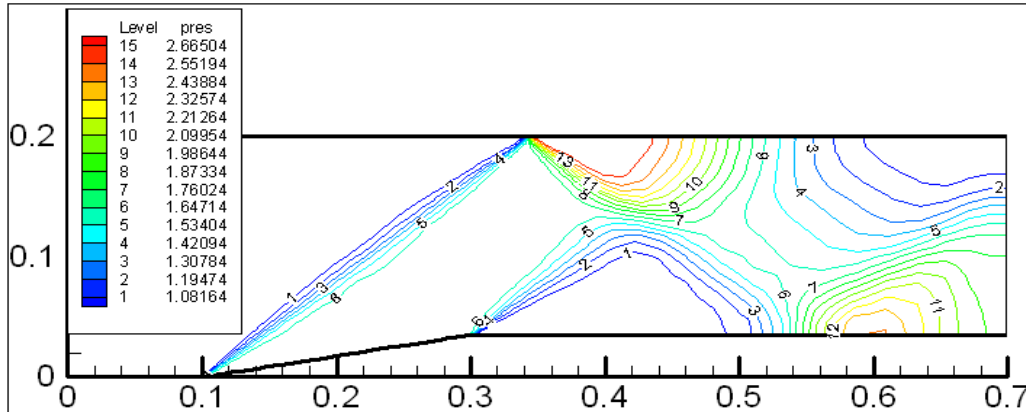


Figure 4.41. Pressure contours for grid#1 for Weno-RUSANOV

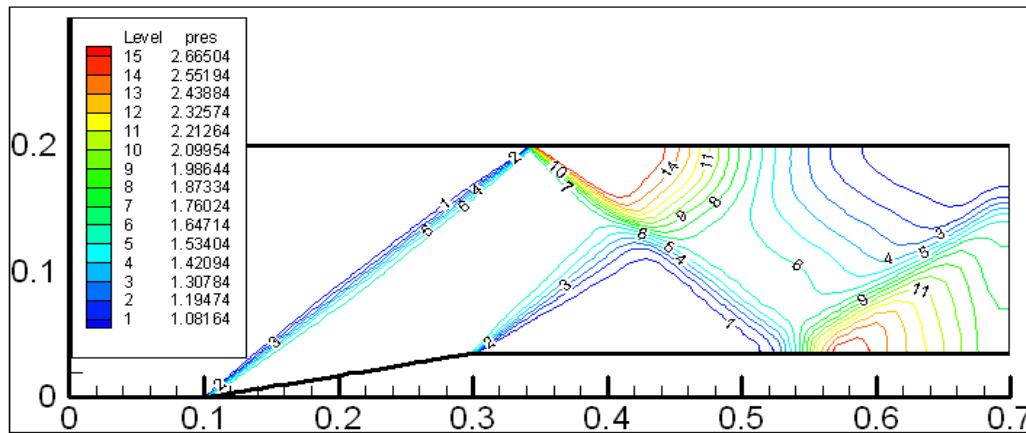


Figure 4.42. Pressure contours for grid#2 for Weno-RUSANOV

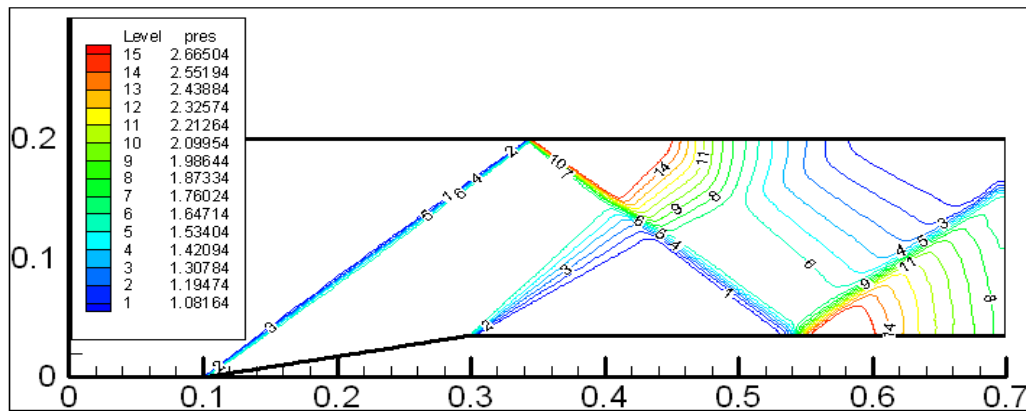
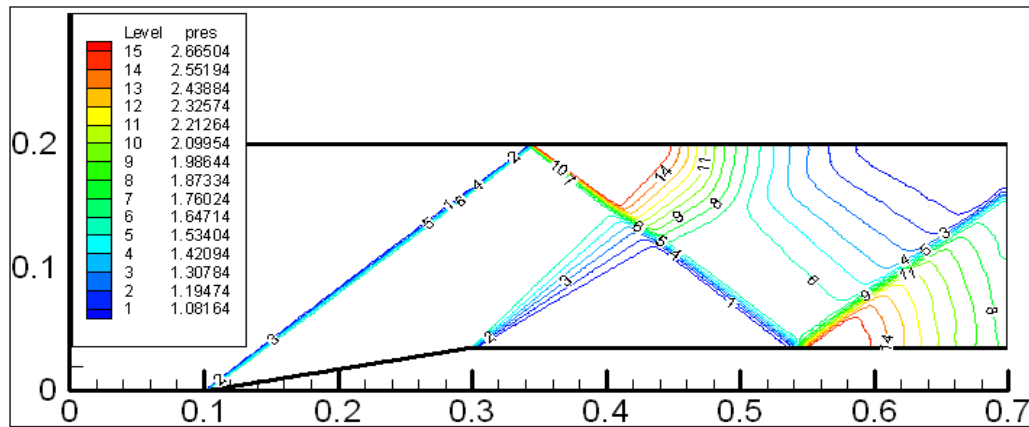
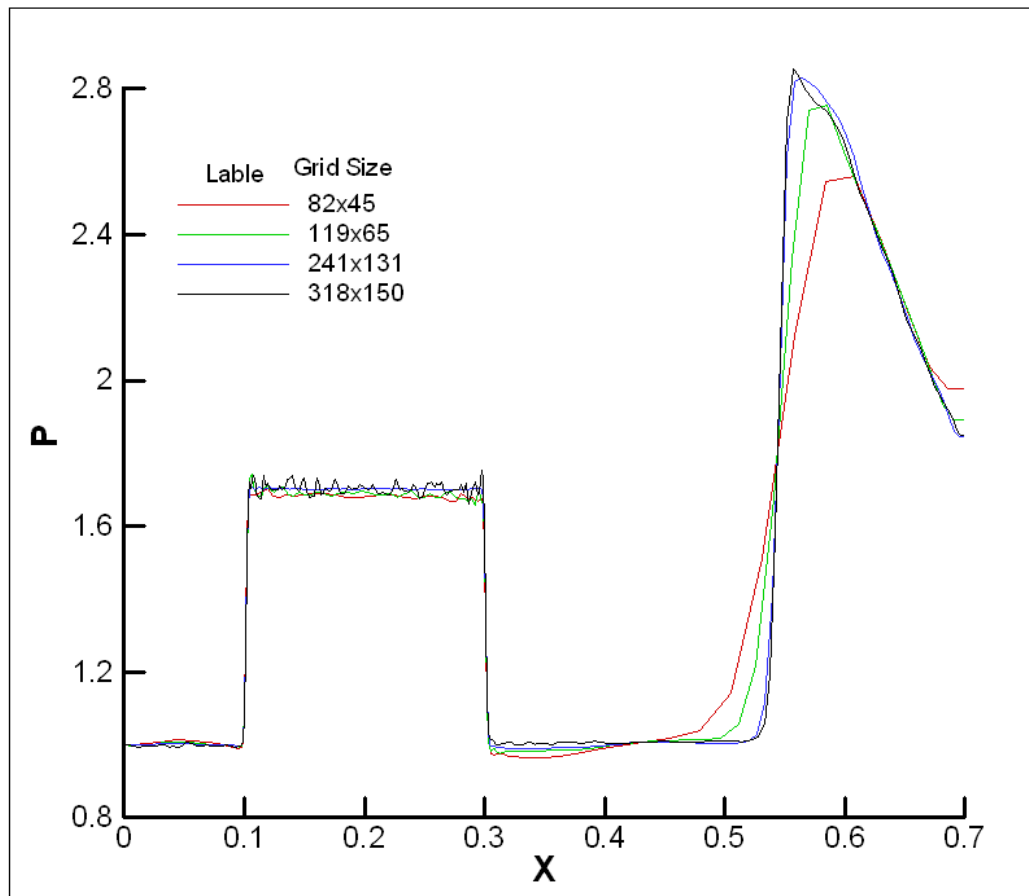


Figure 4.43. Pressure contours for grid#3 for Weno-RUSANOV



**Figure 4.44.** Pressure contours for grid#4 for Weno-RUSANOV



**Figure 4.45.** Pressure distribution on channel wall for Weno-RUSANOV

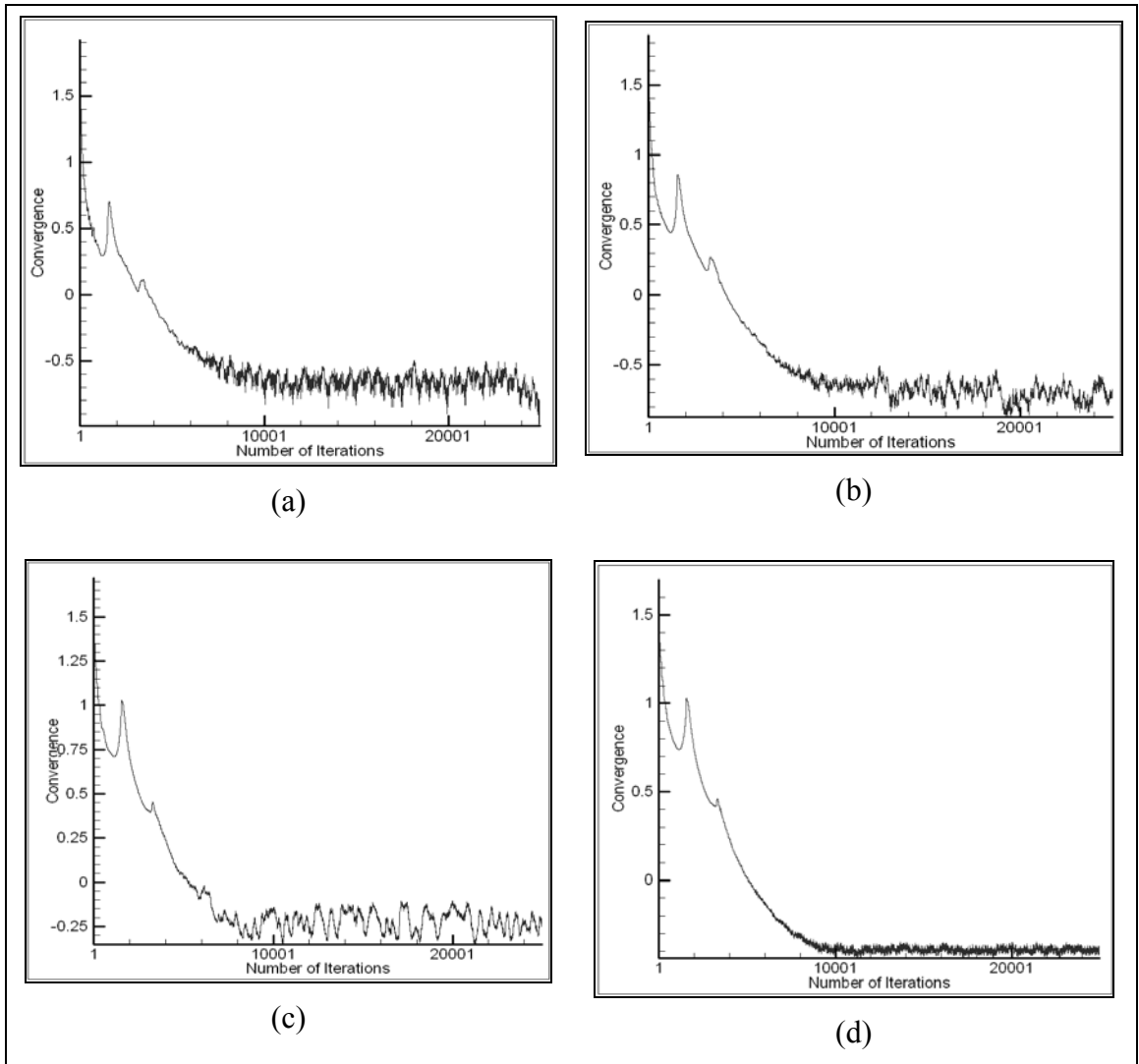


**Figure 4.46.** The convergence history of the WENO-RUSANOV scheme with different mesh sizes (a) Grid#1, (a) Grid#2, (a) Grid#3 and (a) Grid#4

Result for the Rusanov scheme is like the other schemes which has been explained before. However , The convergence history of the Rusanov scheme is worse.

#### 4.2.2.5 Result of the Grid Refinement Study

For grid refinement study four fluxes are tested with four grid sizes. The result of each flux is considered separately. Figures 4.47-50 shows all the results obtained for each grid.

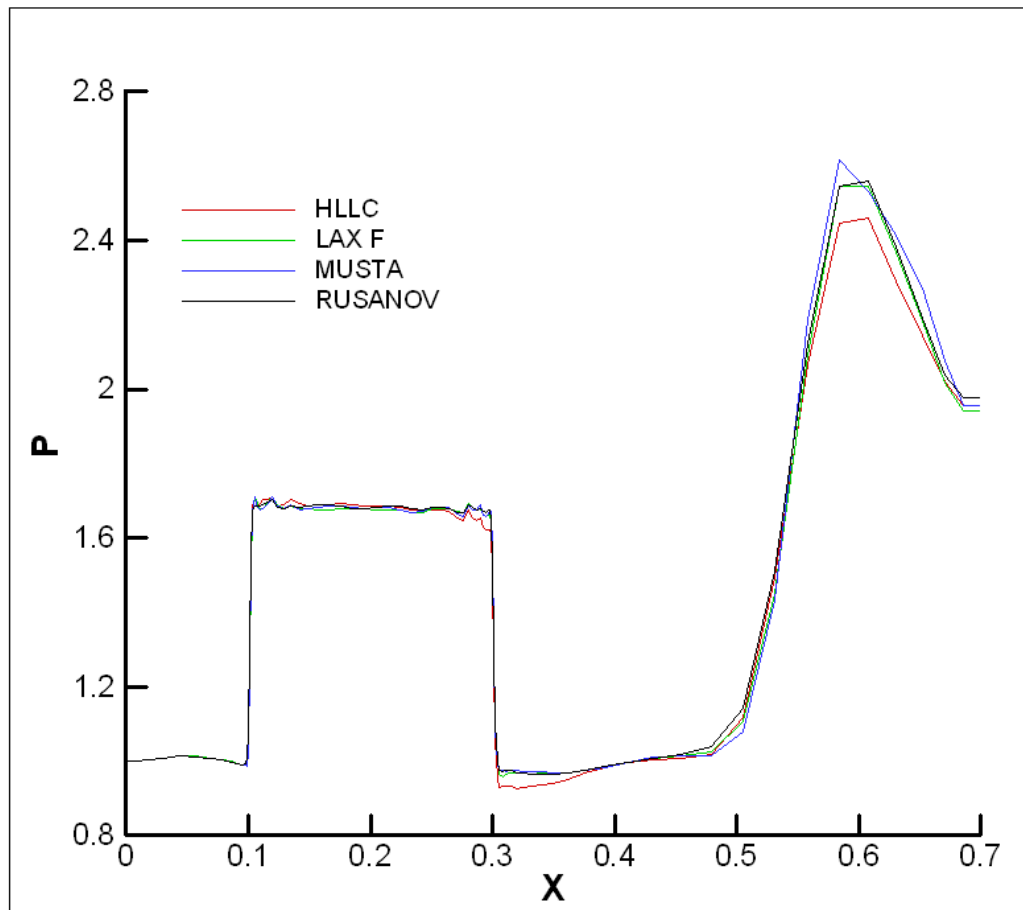


**Figure 4.47.** The pressure distribution on channel wall for all the fluxes and with grid#1 (82x45)

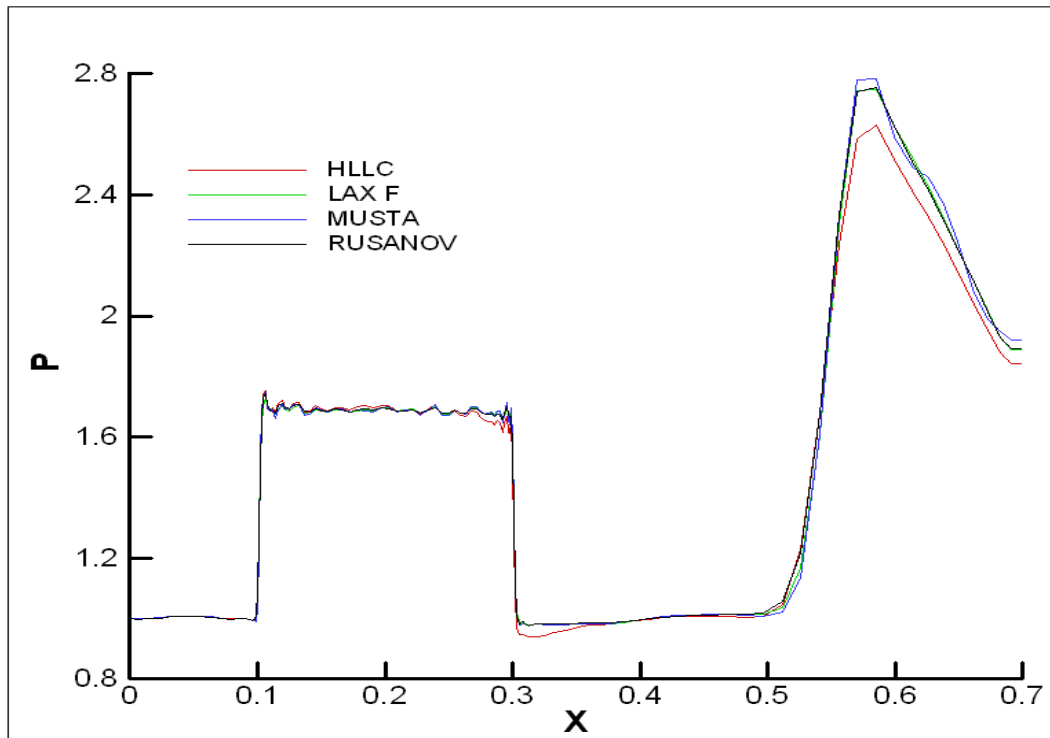


**Figure 4.48.** The pressure distribution on channel wall for all the fluxes and with grid#2 (119x65)

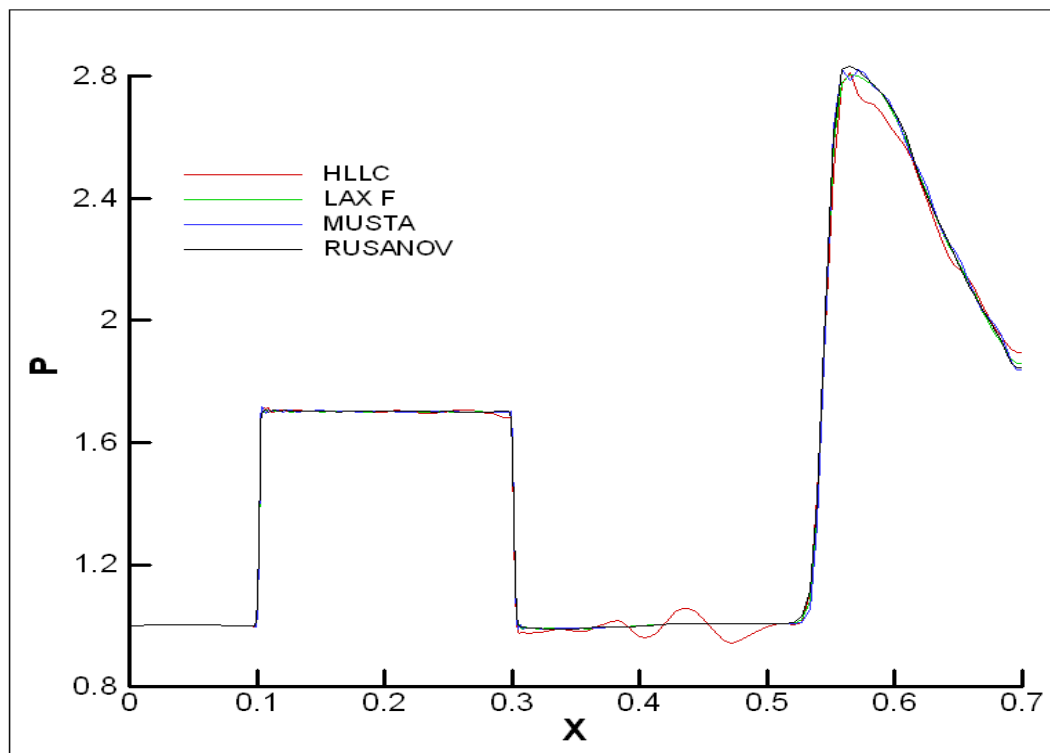


**Figure 4.49.** The pressure distribution on channel wall for all the fluxes and with grid#3 (241x131)

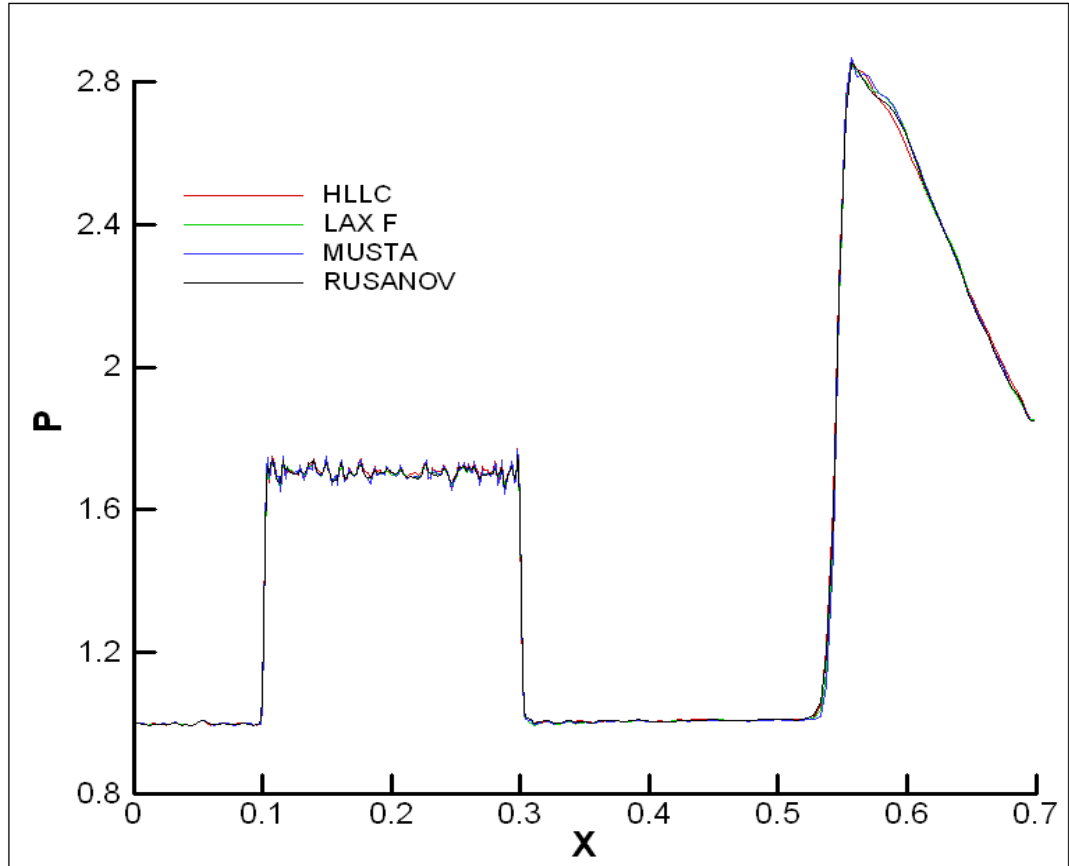


**Figure 4.50.** The pressure distribution on channel wall for all the fluxes and with grid#4 (318x150)

It can be considered from the figures 4.47-50 that if the mesh used in computations is coarser than it would affect resolution of the solution and solution would have some oscillations near discontinuity. If mesh used is finer than solution would be oscillatory. But the difference of these oscillations is in the magnitude. For coarser grid oscillations are bigger in magnitude whereas for finer grid oscillation would be higher in frequency.

For 2-D supersonic channel problem the best results are obtained by grid#3 (241x131). All the fluxes except HLLC flux fits the analytical solution very well.

### 4.2.3 Supersonic Wedge Cascade Results

The supersonic wedge cascade test case is first introduced in [34]. Four flux schemes are tested with this test case and also two different grids are used. The difference of the grids is the skewness of the grid along the boundary of the cascade. The geometry of the cascade is shown at figure 4.51.

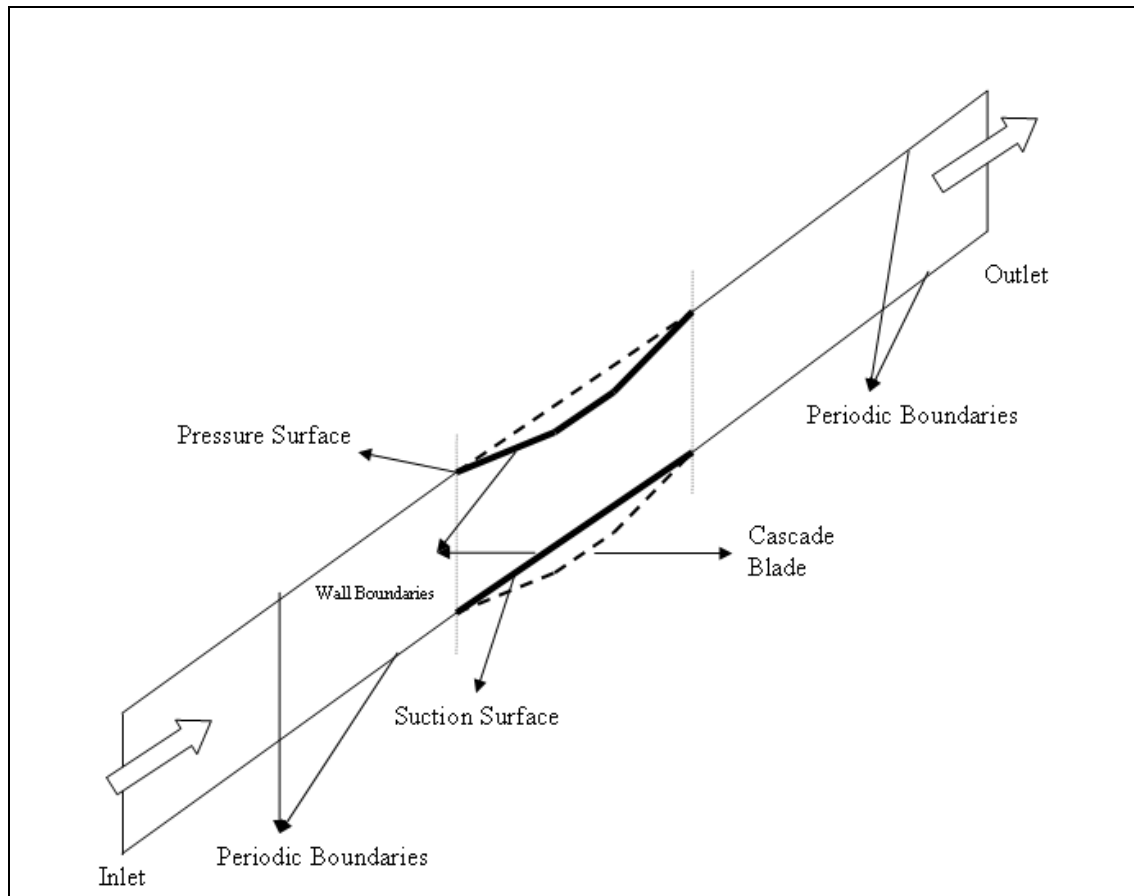


**Figure 4.51.** The supersonic wedge cascade geometry and boundary conditions.

The flow at the inlet of the cascade control volume is supersonic with  $M=1.6$ . The outflow is also supersonic. Therefore supersonic inlet and outlet boundary conditions are employed. In cascade blade walls, classical wall boundary conditions are employed. In the periodic surfaces, shown at figure 4.51, periodic boundary conditions are employed.

The analytical solution of this problem is obtained by Hirsh in [34] using the oblique shock relations and the characteristic theory. The structure of this cascade allows

for shock reflection and shock suppression through the pressure and suction surfaces of the cascade blade. The leading edge of the cascade wedge leads to an oblique shock attached to the nose of the upper blade with a  $45^\circ$  inclination to the incoming flow. Then, the shock reflects from the lower blade with  $48.2^\circ$  reflection angle. This reflected shock is suppressed with the wall inclination of the pressure side. The analytical (Exact) solution of this cascade blade can be viewed in figures 4.52-53.

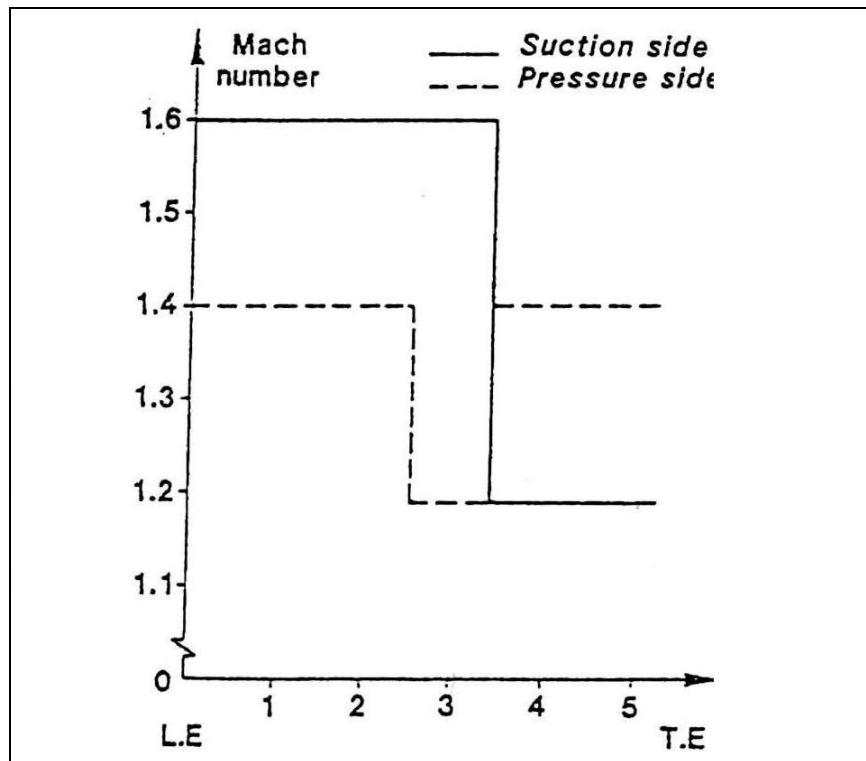


**Figure 4.52.** Analytical (Exact) Mach number distribution on the blade pressure and suction sides [34]

The flow variables at the inlet are assumed as;  $M=1.6$ ,  $\rho=1$ , and  $P=1$ . Initially All the computational domain is set to these variables.

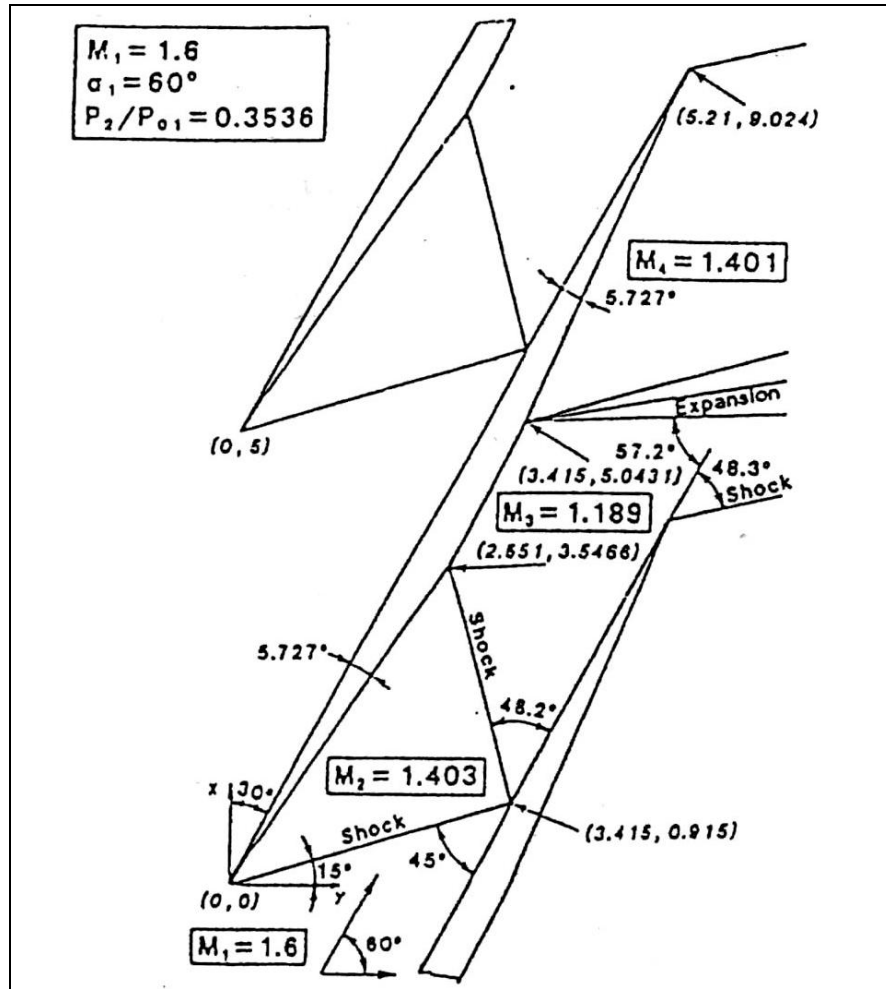


**Figure 4.53.** Shock structure that is found by Analytical solution [34]

The results of the solution are presented as follows. First the results that are obtained by the grid (grid #1) with more skewed geometry near the blade wall boundary are presented. For the first grid case two CFL numbers are tested to see the effect of the CFL number on the solutions. Then the results that are obtained by the grid (grid #2) with less skewed geometry near the blade wall boundary is presented.

#### 4.2.2.6 Results obtained by grid#1

The computational domain and the mesh used can be viewed in figure 4.54. As can be observed from the figure grid lines near the cascade blade wall boundaries are highly skewed. Also the mesh size is 464 x 50.

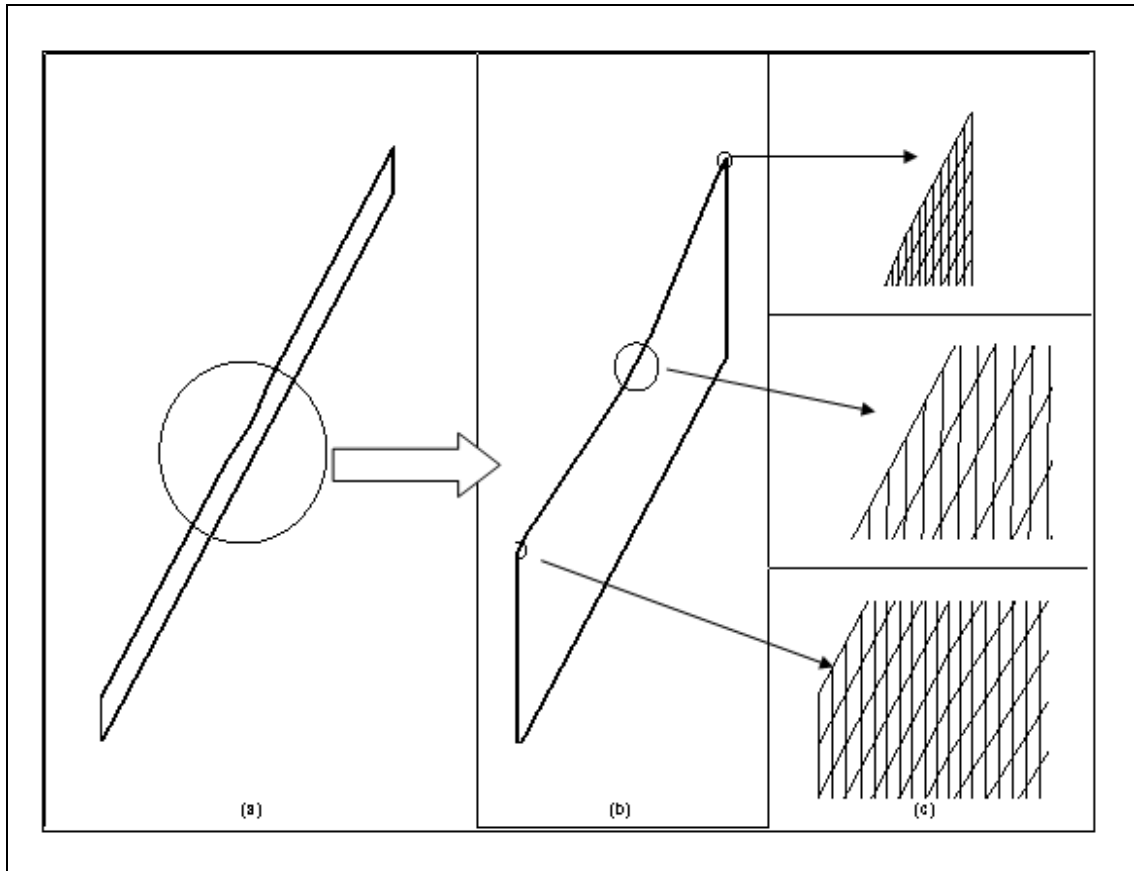


**Figure 4.54.** The Grid#1 for wedge cascade geometry

The results for this case are obtained for four different fluxes. Also the effect of the CFL number on the fluxes is investigated. Two different CFL numbers (0.2 and 0.6) are used. These four fluxes are also checked for the sensitivity of CFL numbers.

The result of HLLC flux can be viewed at figures 4.55-58 . Figures 4.55 and 4.56 shows the mach number contours of the results at CFL number 0.2 and 06 respectively. Figure 4.57 shows Mach number distributions at blade walls. Figure 4.58 shows Convergence histories of the results.

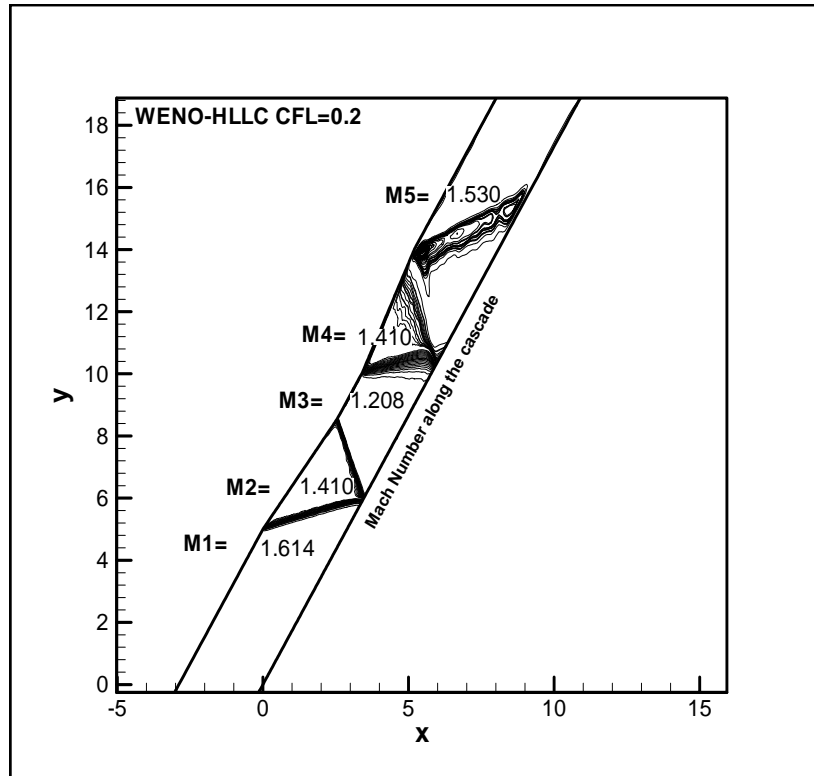


**Figure 4.55.** Mach number contour obtained by WENO HLLC scheme for CFL=0.2

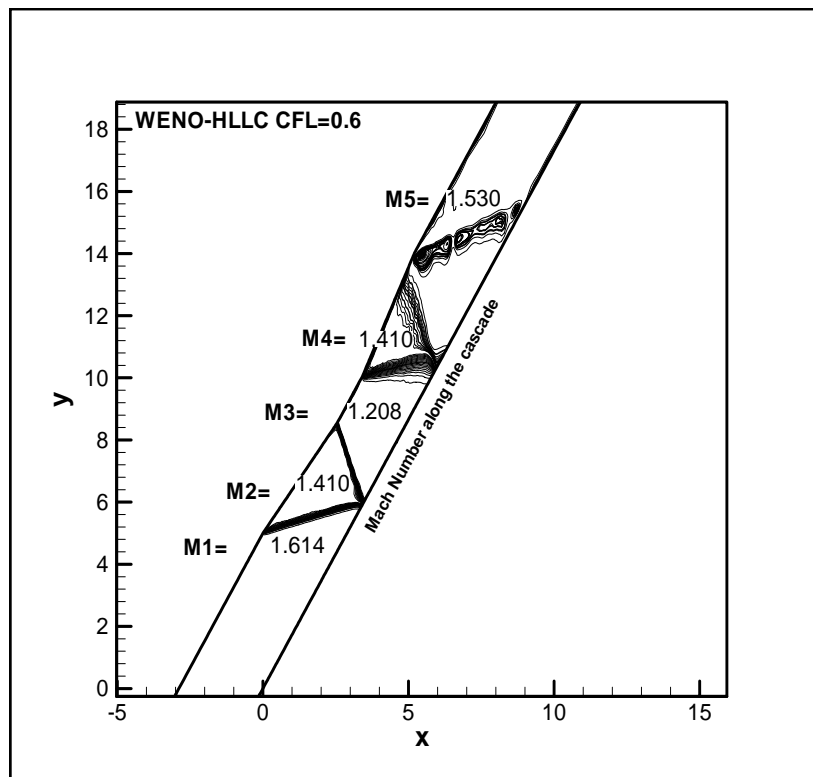


**Figure 4.56.** Mach number contours obtained by WENO HLLC scheme for CFL=0.6

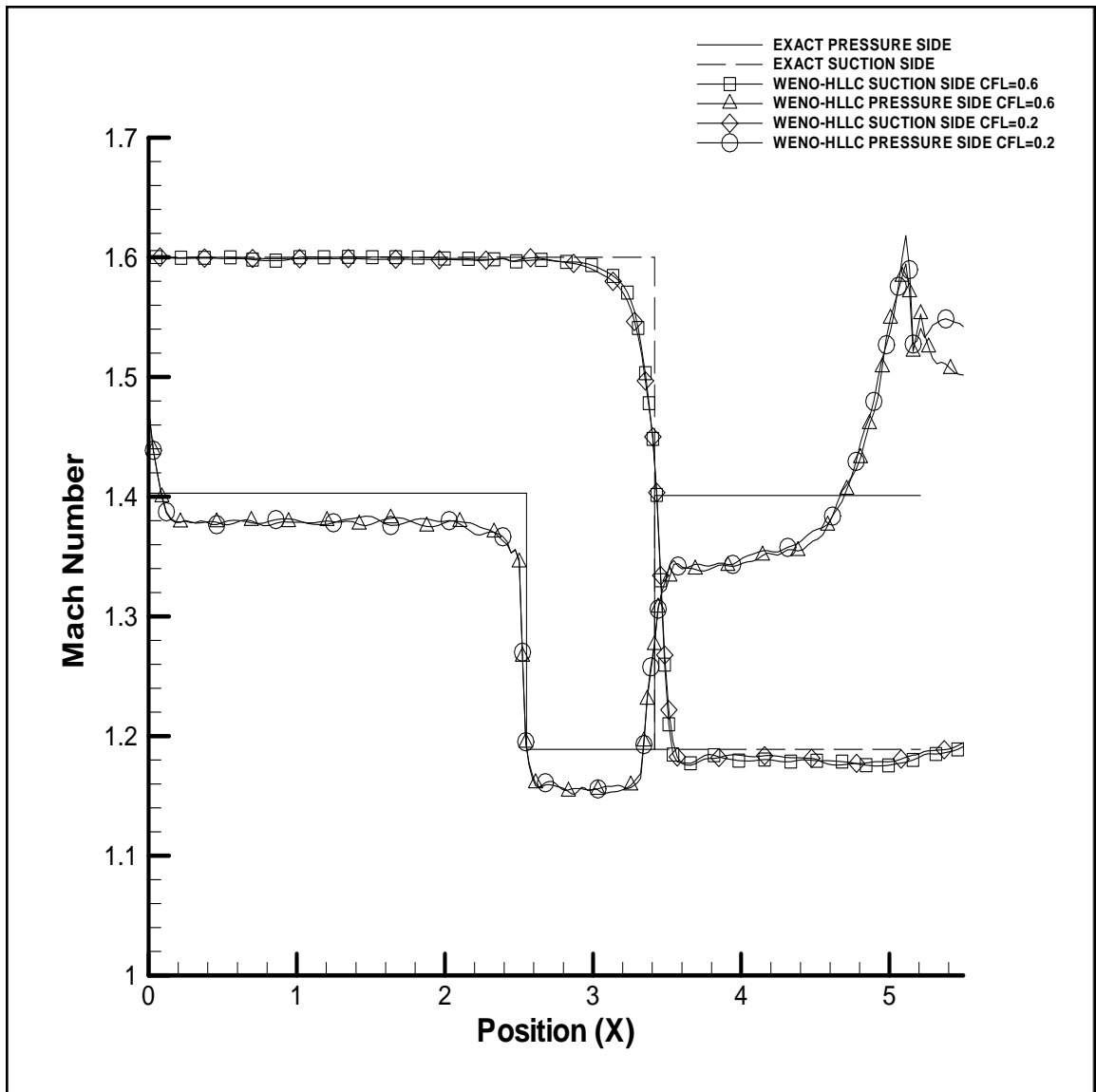


**Figure 4.57.** Mach Number distributions along the wedge cascade walls for both CFL numbers

When compared with Figure 4.53, it is seen that Figures 4.55 and 4.56 have reasonable shock wave structures. Also the mach numbers after each shock wave agree closely with the analytical ones. Some comments can be made about the resolution of the scheme. It can be concluded that the resolution of first two shock waves are very well. But the resolution of expansion fan is not so good.

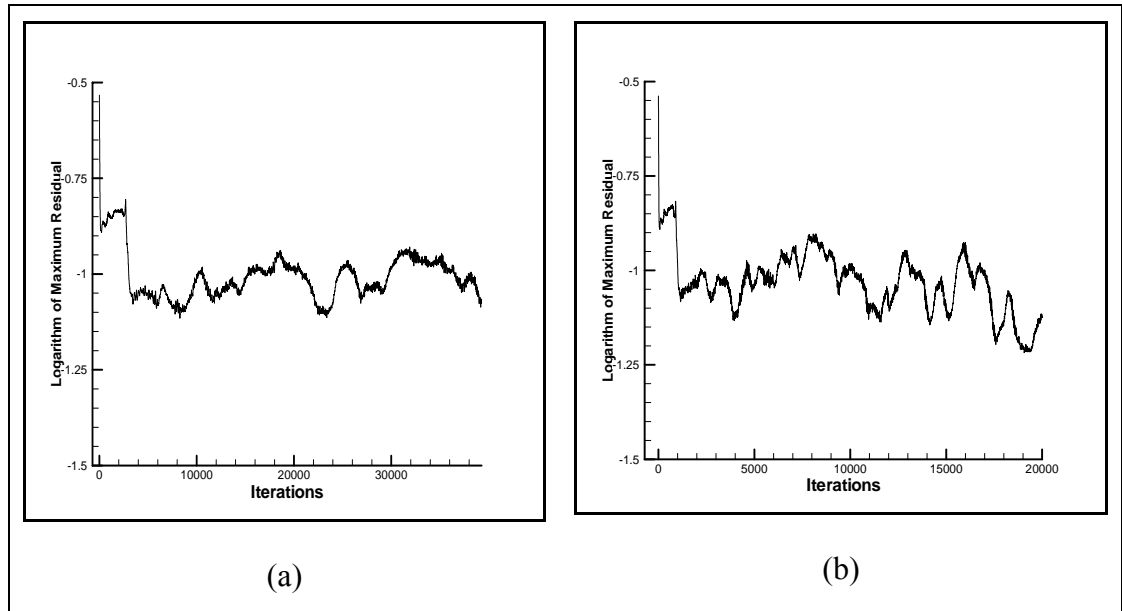


**Figure 4.58.** Convergence History graphs for WENO-HLLC scheme (a) CFL =0.2 ,(b) CFL=0.6

Due to the periodic boundary condition, there is an artificial discontinuity which originates from the end of the suction side. That disturbs the solution and affects the exit portion of the cascade.

The mach number distributions that are shown at figure 4.57 show that there is not so much difference between the two CFL numbers. However low CFL number result in mach contours with less oscillations and better resolution.

When the convergence graphs are investigated it can be concluded that WENO – HLLC scheme has very weak convergence and also low CFL numbers converges better than high CFL number.

The result of Lax Friedrichs flux can be viewed at figures 4.59-62

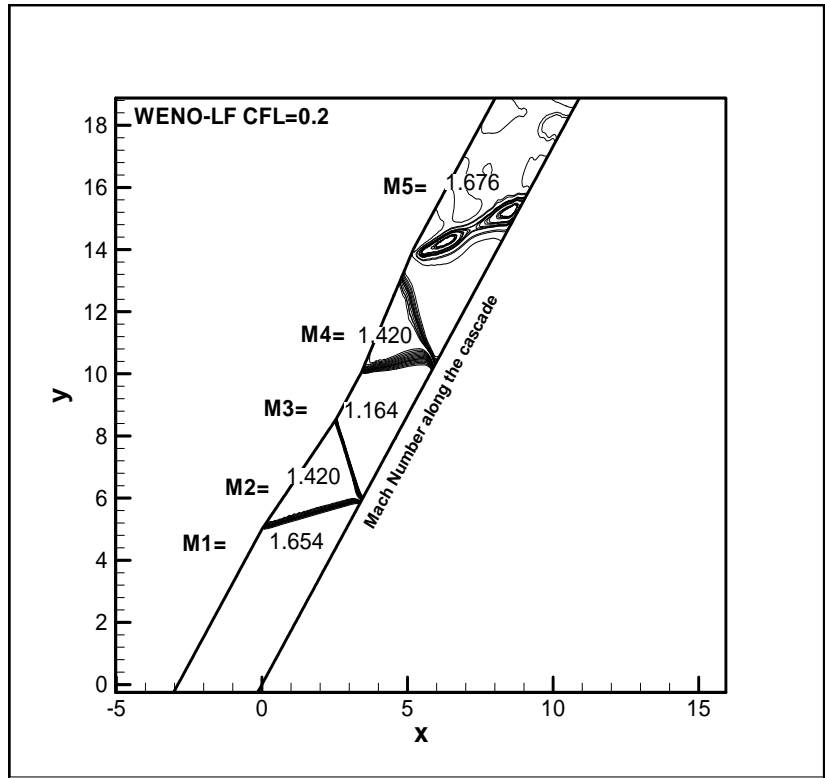


Figure 4.59. Mach number contour obtained by WENO LF scheme for CFL=0.2

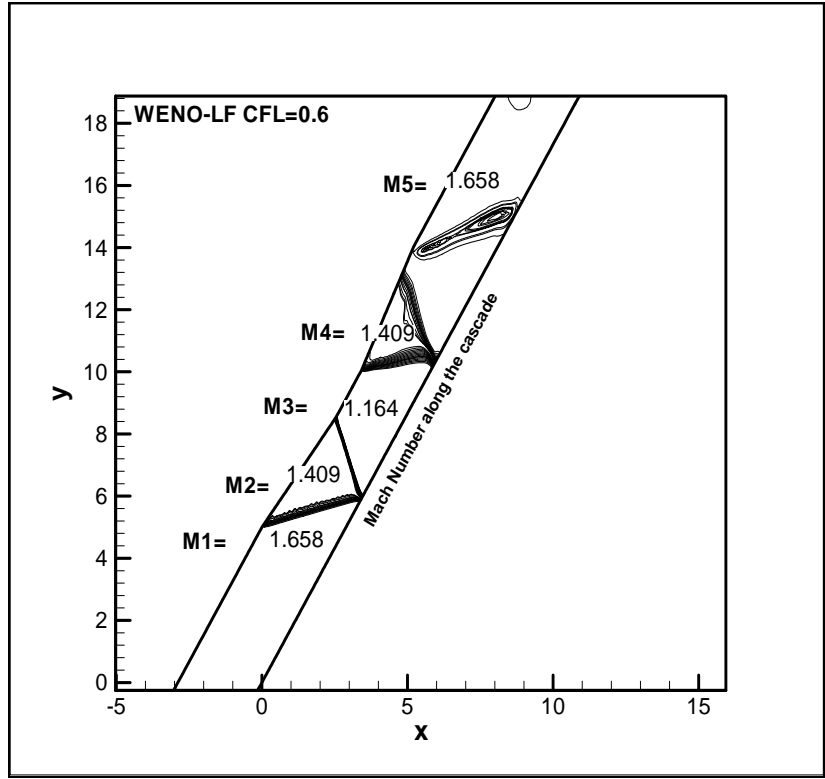
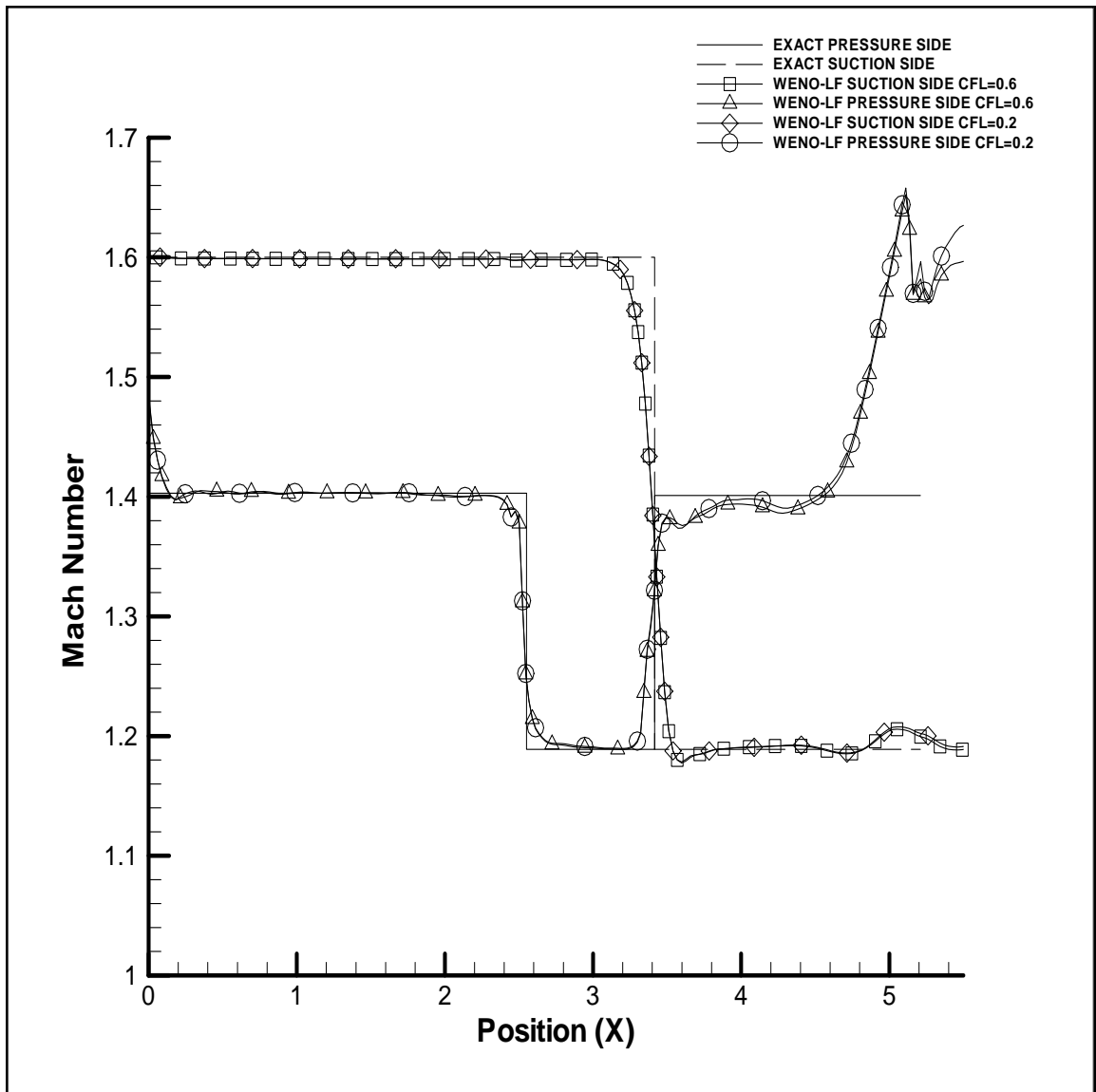
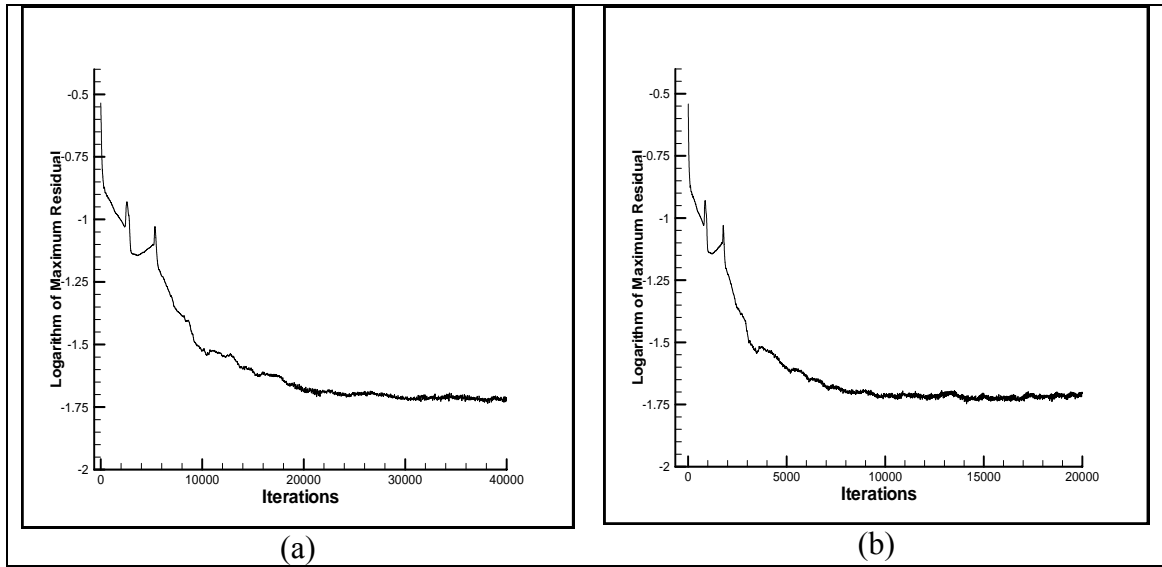


Figure 4.60. Mach number contour obtained by WENO LF scheme for CFL=0.6



**Figure 4.61.** Mach Number distributions along the wedge cascade walls for both CFL numbers

The shock structure obtained by Lax-Friedrich scheme is also acceptable when compared with analytical results. However resolution of the scheme is not as high as the WENO-HLLC scheme. When mach numbers are taken into account, The Lax-Friedrich flux is more accurate than HLLC flux.



**Figure 4.62.** Convergence History graphs for WENO-LF scheme (a) CFL =0.2 ,(b) CFL=0.6

The Mach number distributions given in figure 4.61 shows a good agreement of the results with the analytical ones. The scheme has exactly same behavior for two CFL numbers but the convergence history graphs shows that CFL number of 0.2 is a better choice for Lax-Friedrich flux.

The result of MUSTA flux can be viewed at figures 4.63-66

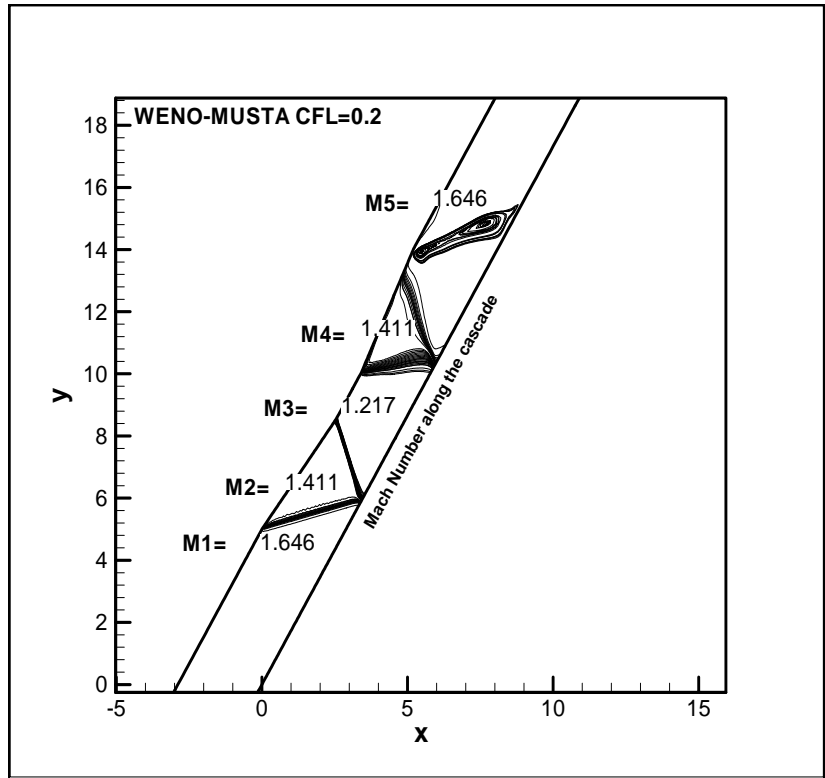


**Figure 4.63.** Mach number contour obtained by WENO-MUSTA scheme for CFL=0.2

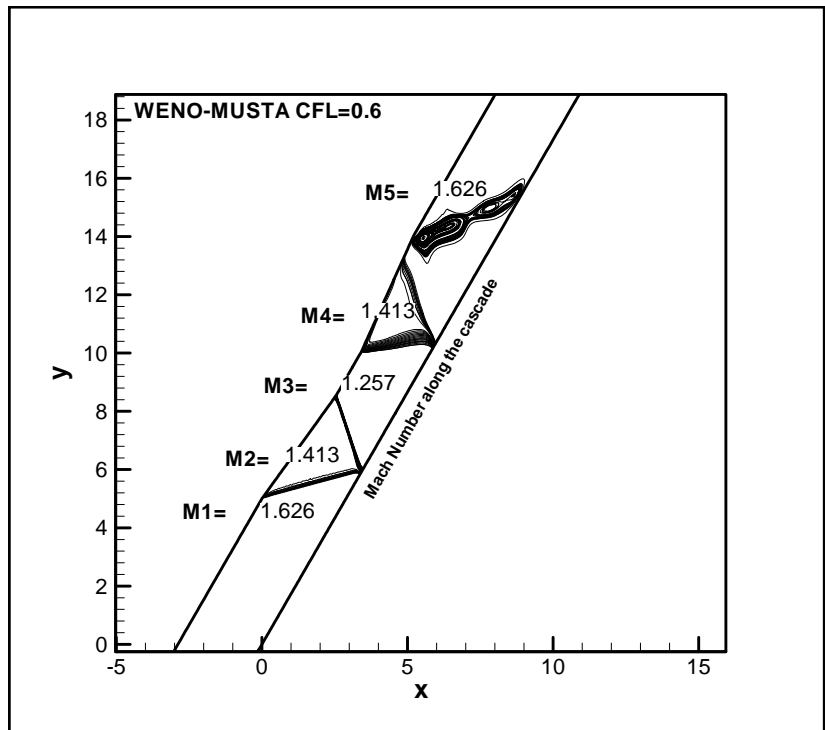


**Figure 4.64.** Mach number contour obtained by WENO-MUSTA scheme for CFL=0.6

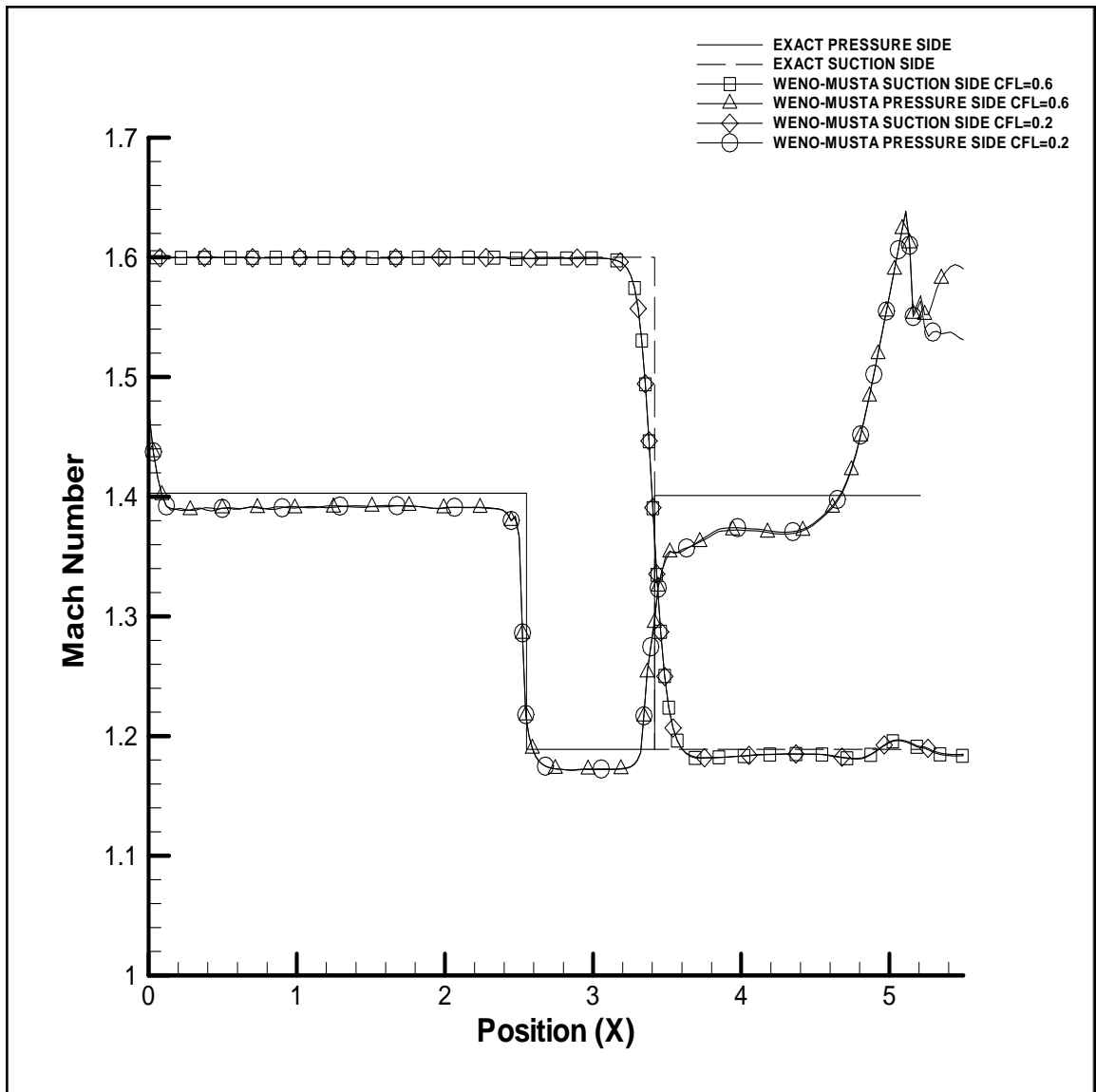


**Figure 4.65.** . Mach Number distributions along the wedge cascade walls for both CFL numbers

The results presented in figures 4.63 and 4.64 present very reasonable shock structure. Also the mach numbers after each shock wave is quite good when compared to the figure 4.53 . If Musta flux is compared to HLLC , Musta flux attains more accurate results but Hllc flux can presents results with higher resolution .

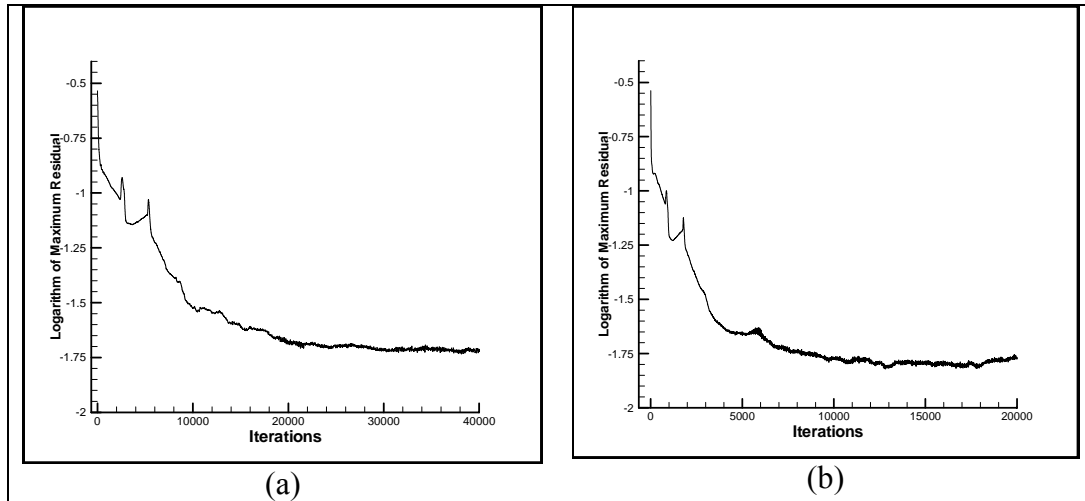


**Figure 4.66.** Convergence History graphs for WENO-MUSTA scheme

(a) CFL =0.2, (b) CFL=0.6

Figure 4.65 shows the comparison of results obtained by MUSTA flux with the analytical solution of the problem. WENO-MUSTA scheme fits the analytical results for suction side of the cascade but for the pressure side of the cascade, the obtained results are not so good as the suction side's. When the results are compared with the Lax – Friedrichs and HLLC fluxes, It can be observed that results obtained by MUSTA flux is better than the one by HLLC flux and worse than the one obtained by Lax-Friedrich.

Like the other fluxes, MUSTA flux has a low sensitivity to the CFL number. The convergence history graphs obtained by WENO-MUSTA scheme shows that lower CFL number would have more stable results.

The last flux is Rusanov flux, the result of RUSANOV flux can be viewed at figures 4.67-70.

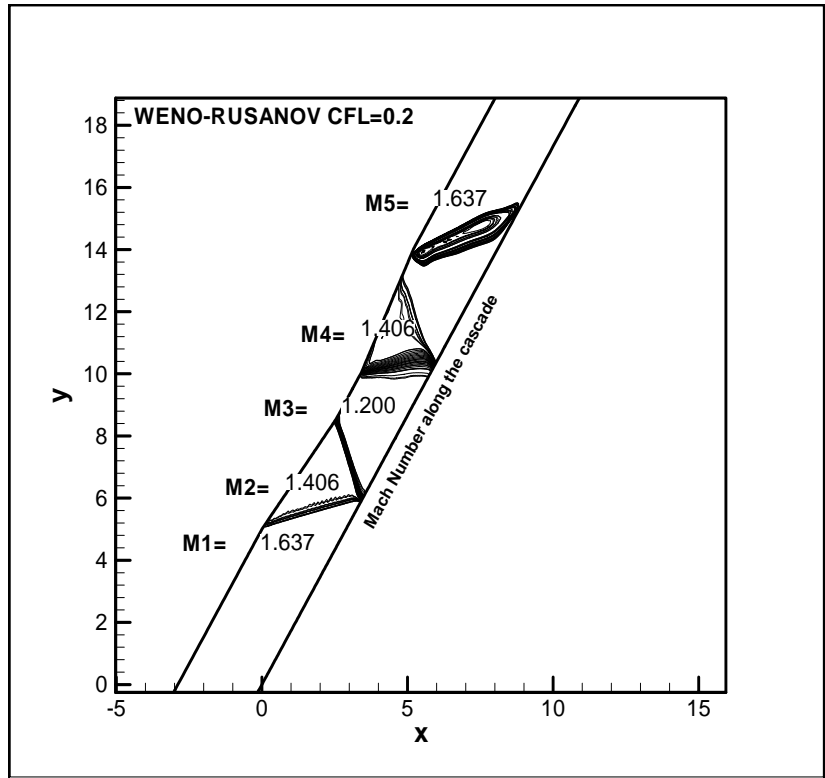


**Figure 4.67.** Mach number contour obtained by WENO-RUSANOV scheme for CFL=0.2

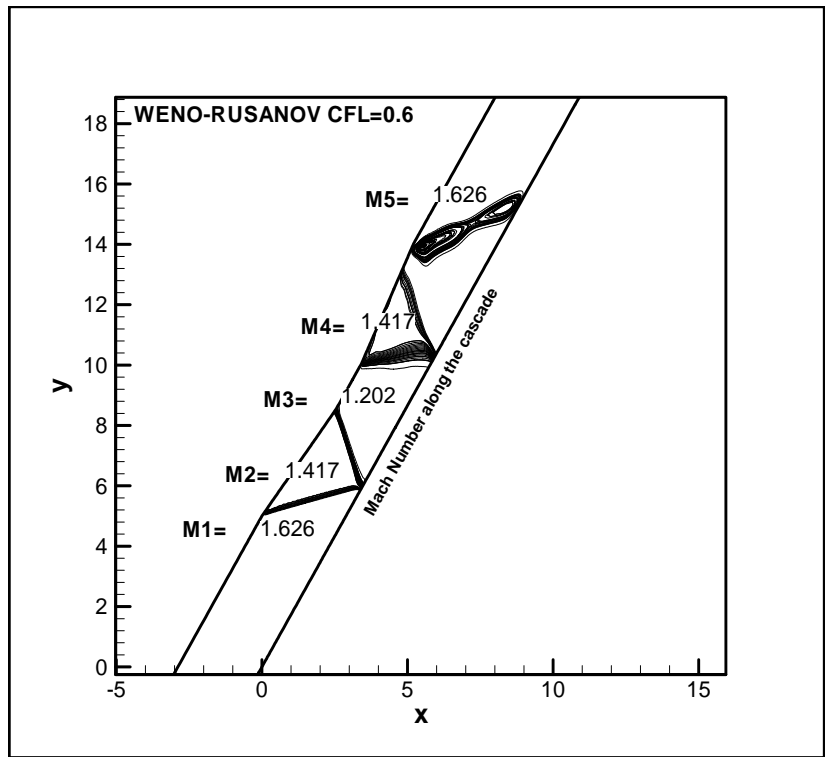


**Figure 4.68.** Mach number contour obtained by WENO-RUSANOV scheme for CFL=0.6

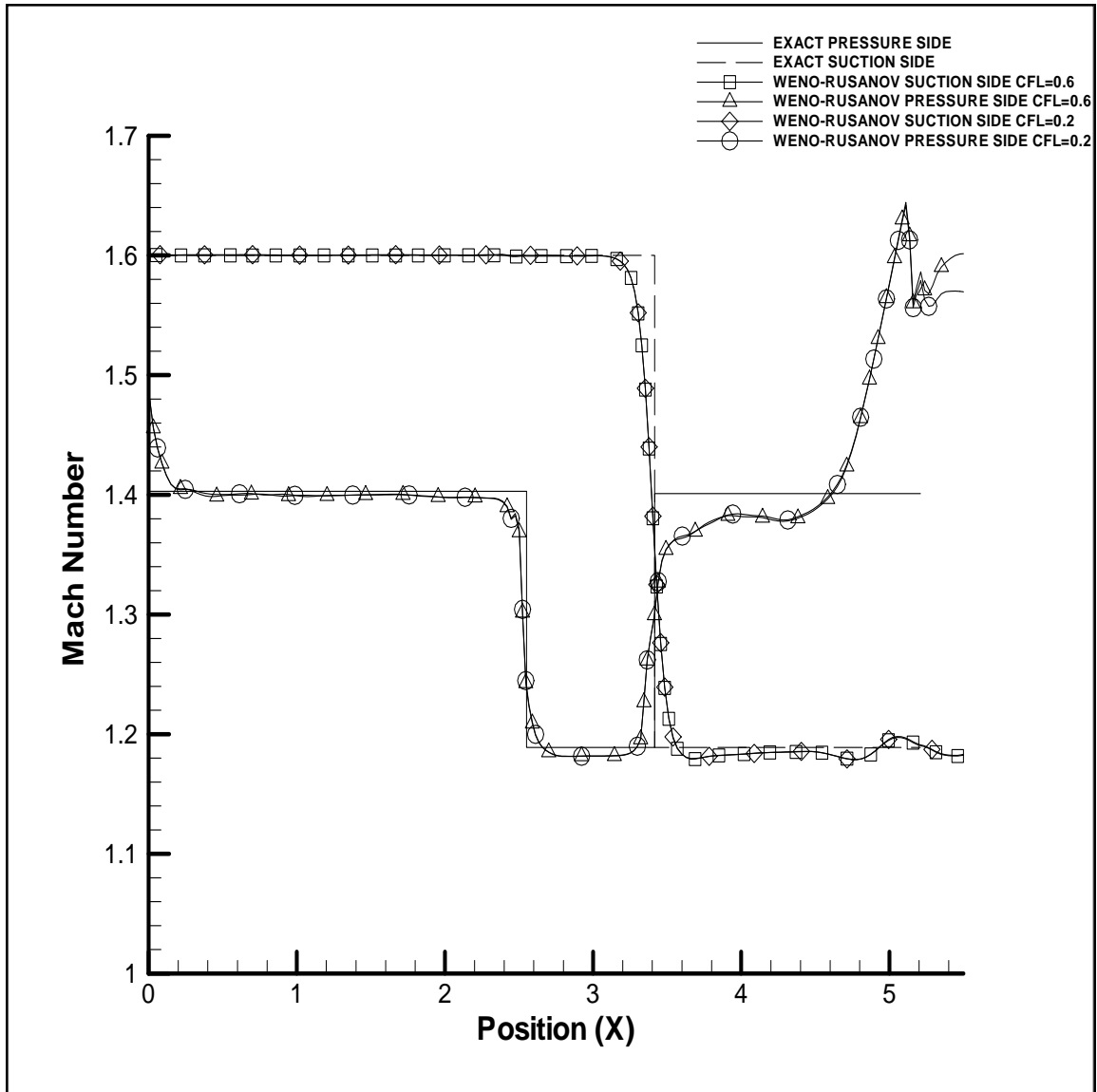


**Figure 4.69.** Mach number distributions along the wedge cascade walls for both CFL numbers

Figures 4.67 and 4.68 show the mach contours of the results obtained by WENO-RUSANOV scheme. If the results are compared with the other results, It can be observed that there is not so much difference on the structure of the shock waves and the distribution of the mach numbers.

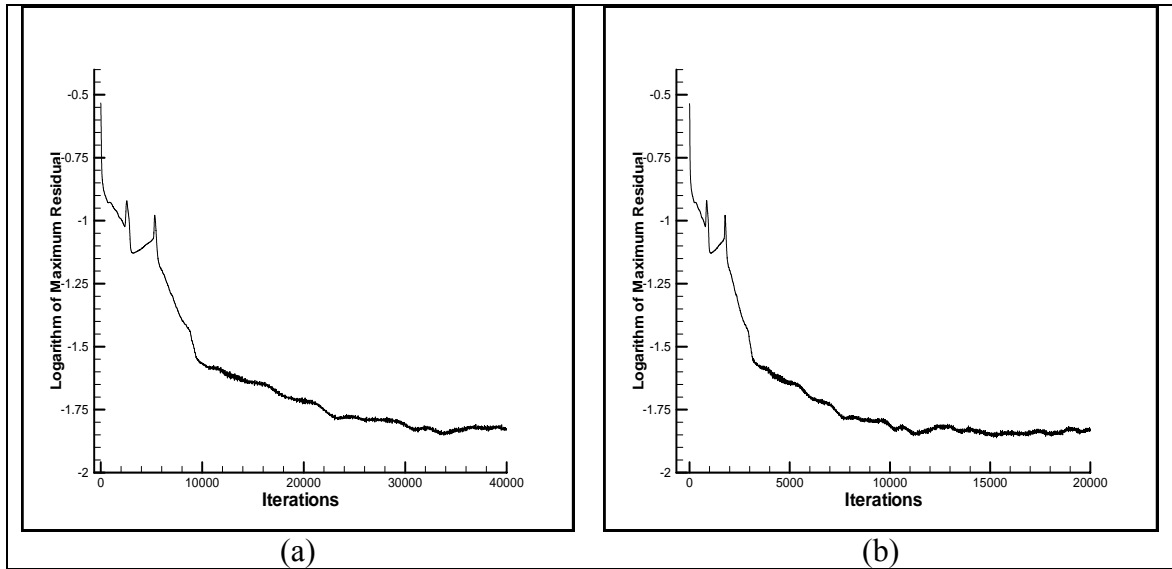


**Figure 4.70.** Convergence History graphs for WENO-LF flux (a) CFL =0.2,  
(b) CFL=0.6

Figure 4.69 shows the Mach number distribution on the pressure and suction sides of the cascade blade. Distribution of the Mach number along the pressure side of the blade agrees with the analytical solution of the problem. However mach number distribution along the suction side does not fit as close as the pressure side. As the other schemes, there is no effect of the CFL number.

Also, figure 4.70 shows the convergence history graphs of the scheme. It can be observed that WENO-RUSANOV scheme is more stable than other schemes. Moreover, choosing low CFL number increases the stability very little.

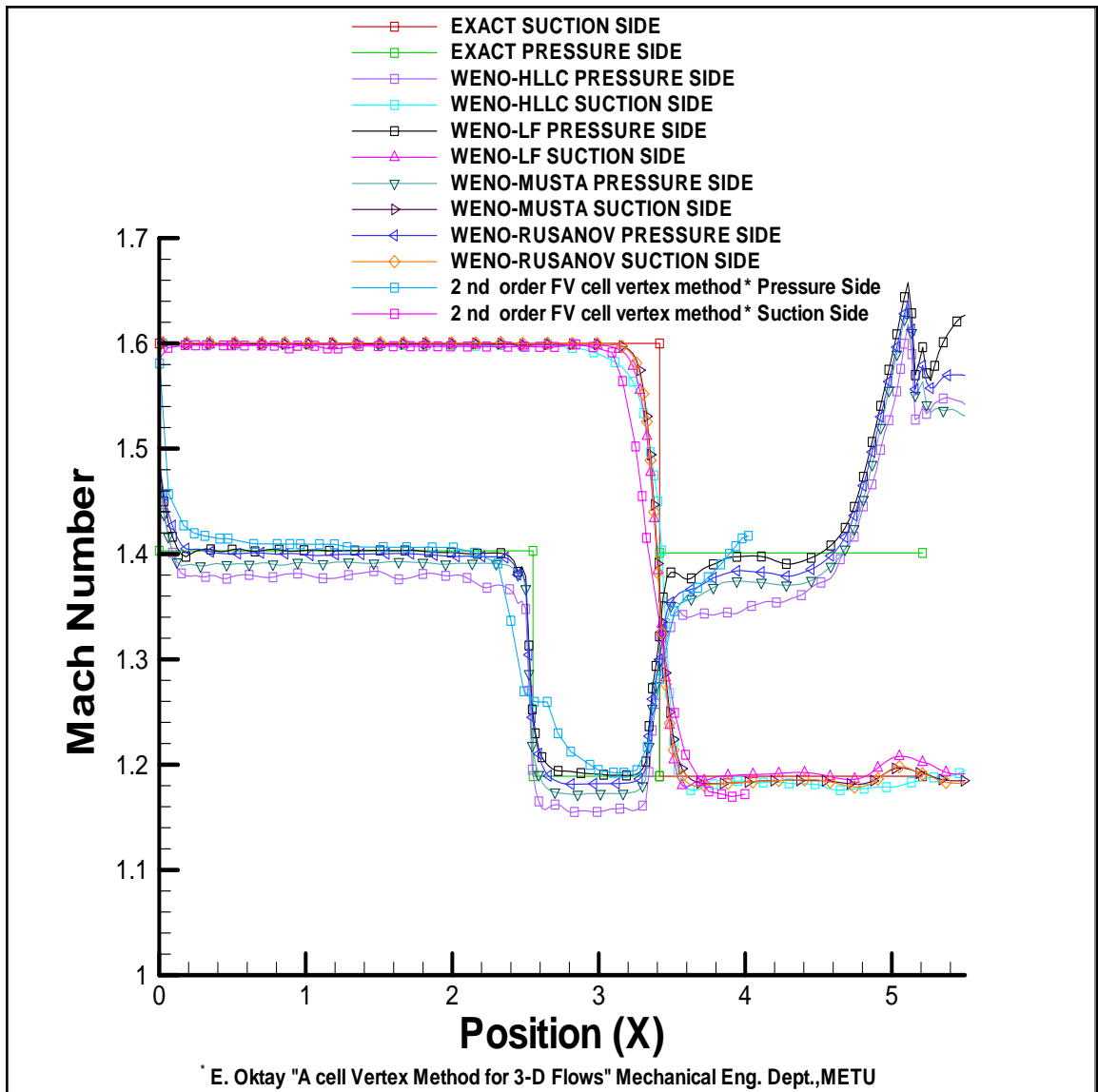


**Figure 4.71.** Comparison of the Mach number distribution of all the fluxes for grid#1 and for CFL=0.2

Figures 4.71 and 4.72 shows the effect of the fluxes on the Mach number distribution along the pressure and suction side of the cascade blade.

It can be concluded that for the pressure side MUSTA flux gives the best agreement with the analytical results. Actually, all the fluxes gives very similar results .

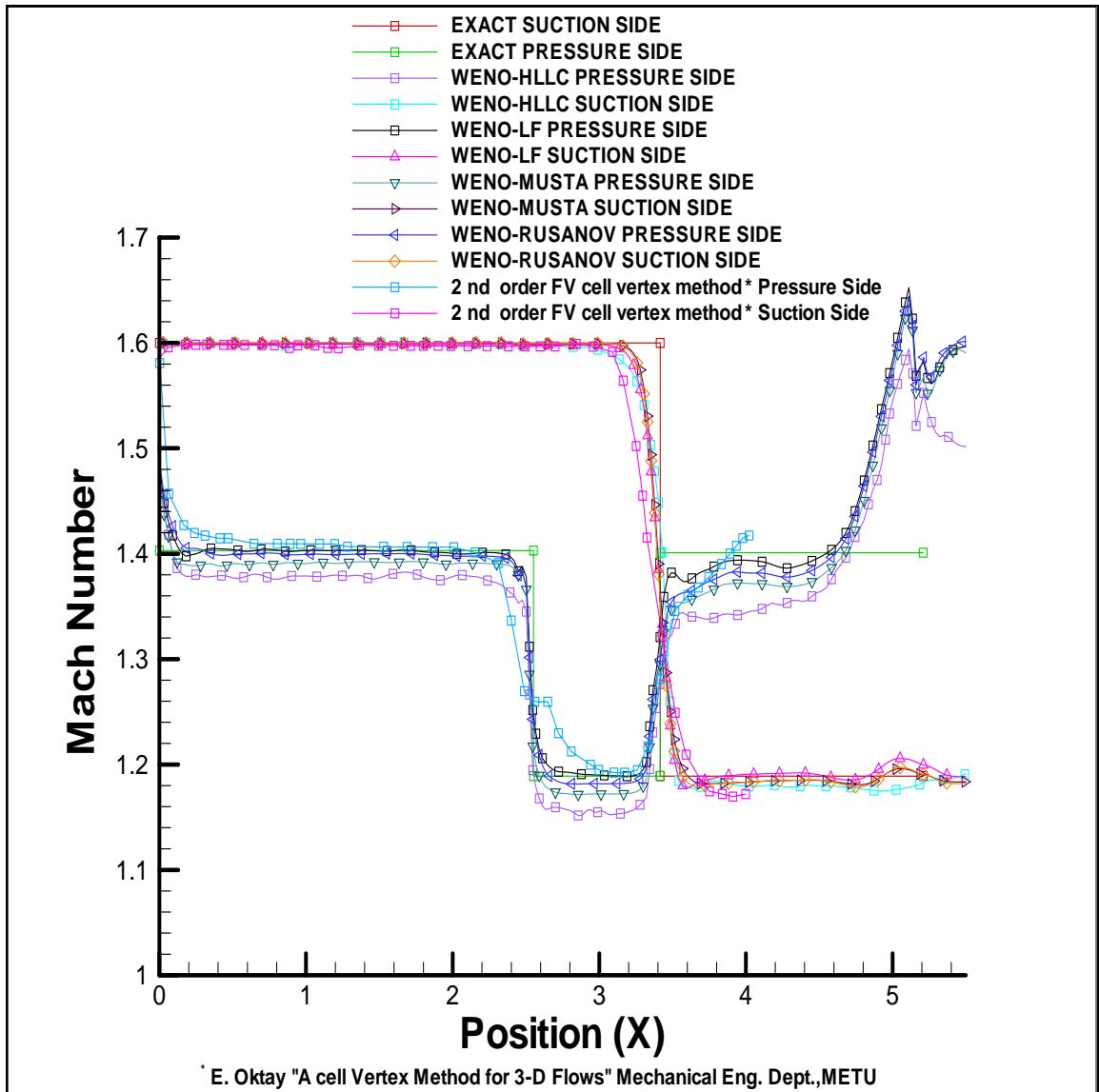


**Figure 4.72.** Comparison of the Mach number distribution of all the fluxes for grid#1 and for CFL=0.6

Because of very complicated shock wave structure, it is hard to obtain acceptable results for suction side of the cascade. Results of the fluxes are more distinguished for suction side. The best fit with analytical result is obtained with Lax-Friedrich flux. Other fluxes except HLLC flux have also very similar results. HLLC flux has underestimated the mach numbers after the shock waves. Moreover, increase in the CFL number can only be sensed by WENO-HLLC scheme.

#### 4.2.2.7 Result obtained by grid#2

The computational domain and the mesh used can be viewed in figure 4.73. As can be observed from the figure grid lines near the cascade blade wall boundaries are not highly skewed as grid#1. The aim is to see the effect of the mesh near wall boundary to the solution. The mesh size used is 464 x 70.

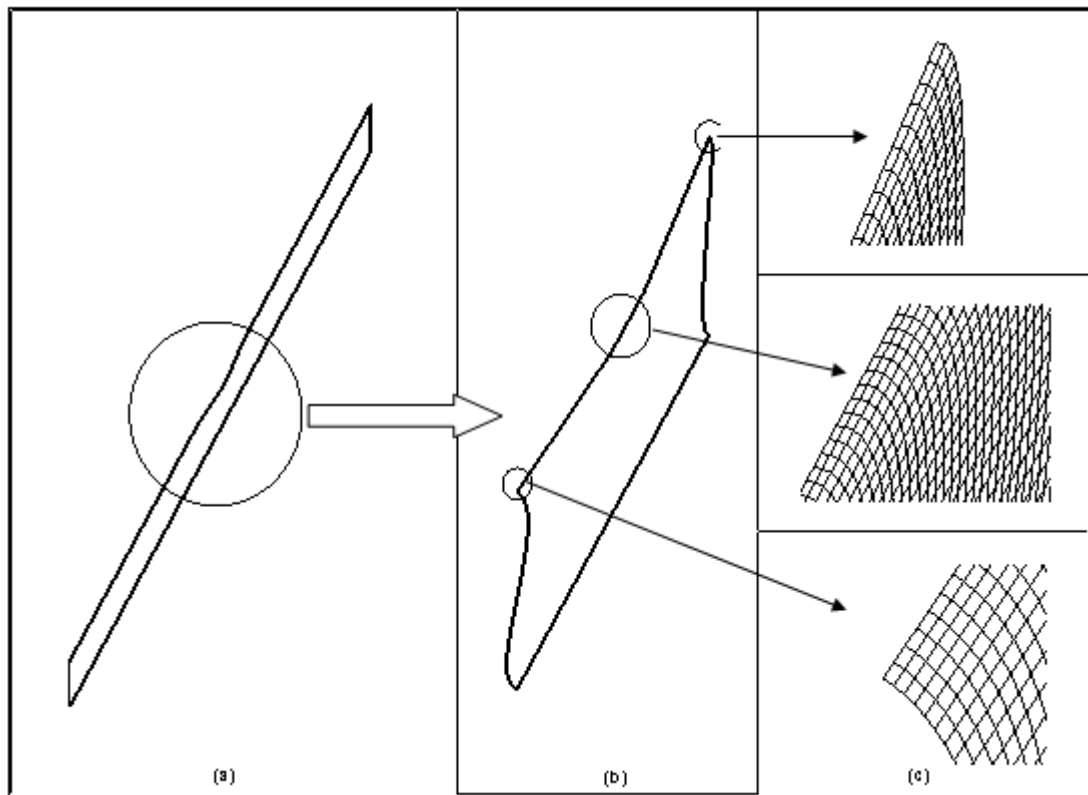


**Figure 4.73.** The Grid#2 for wedge cascade geometry

The results for this case are obtained for four different fluxes. Constant CFL number (CFL=0.6) is used in results. The results are presented in following figures.

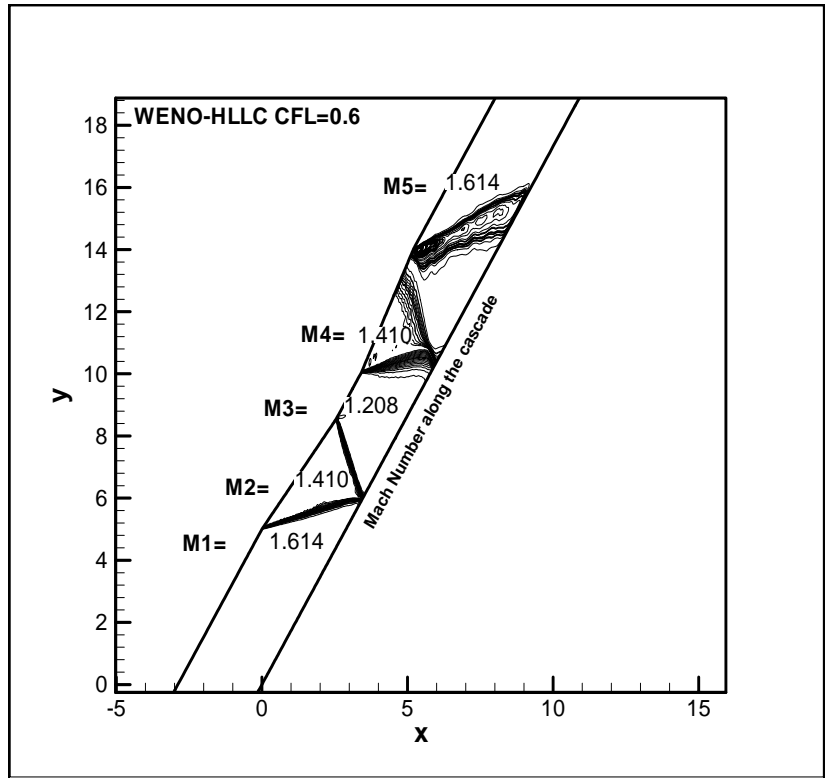


Figure 4.74. Mach number contour obtained by WENO-HLLC scheme

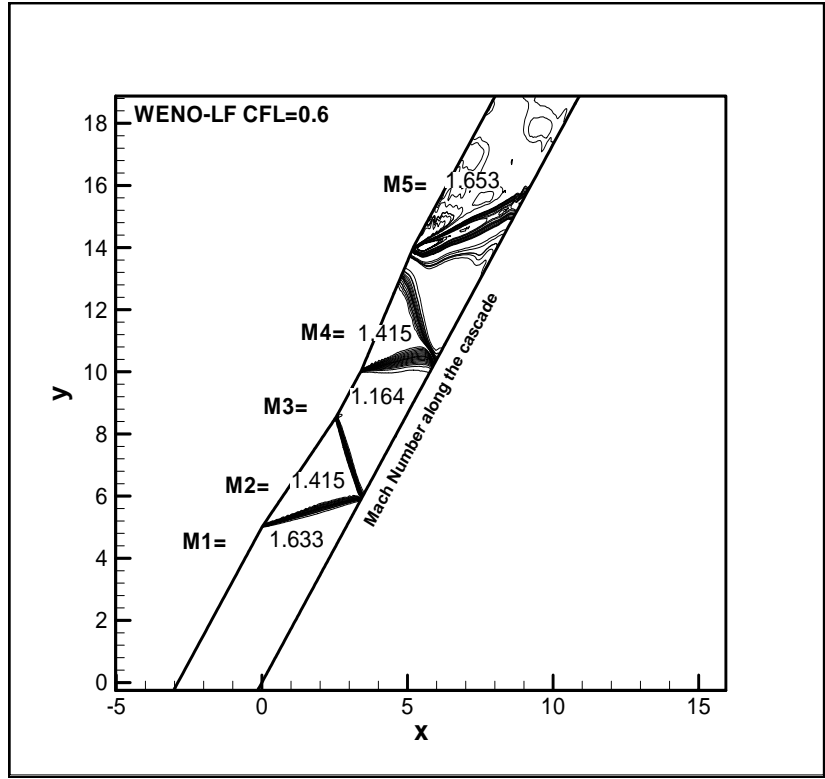


Figure 4.75. Mach number contour obtained by WENO-LF scheme

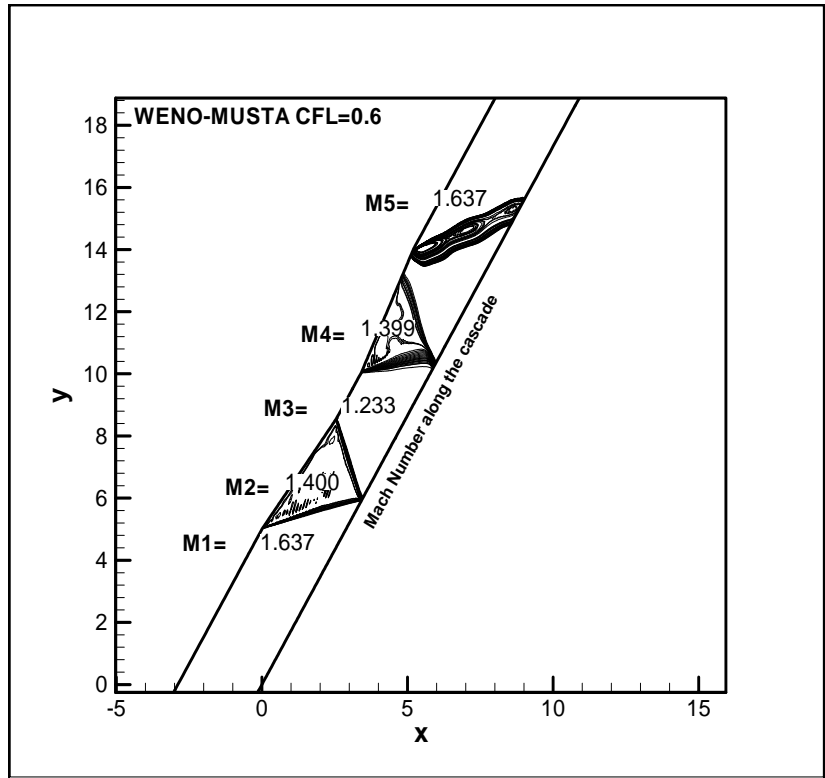


Figure 4.76. Mach number contour obtained by WENO-MUSTA scheme

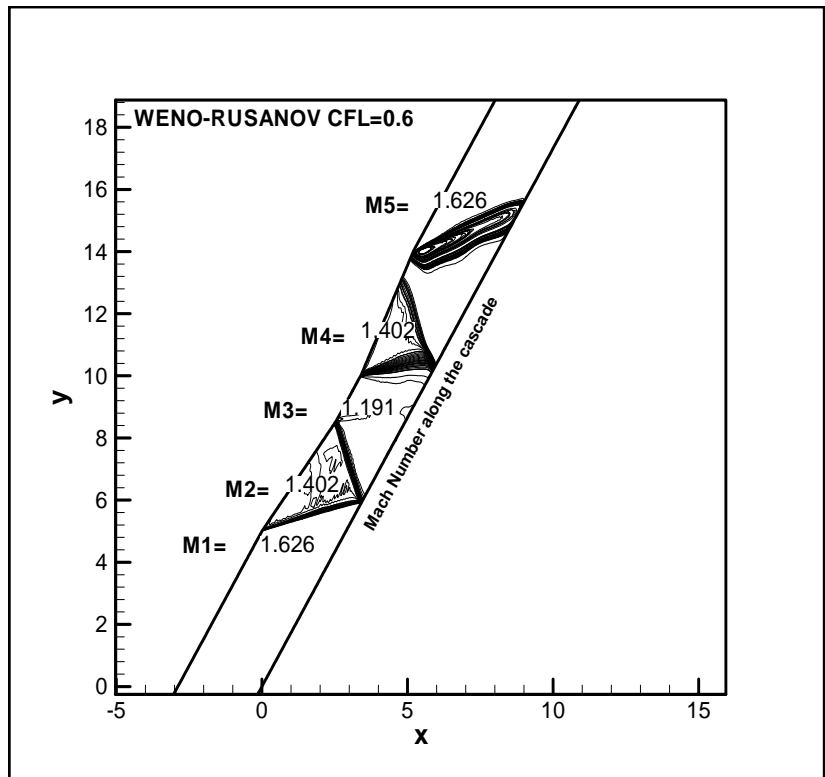
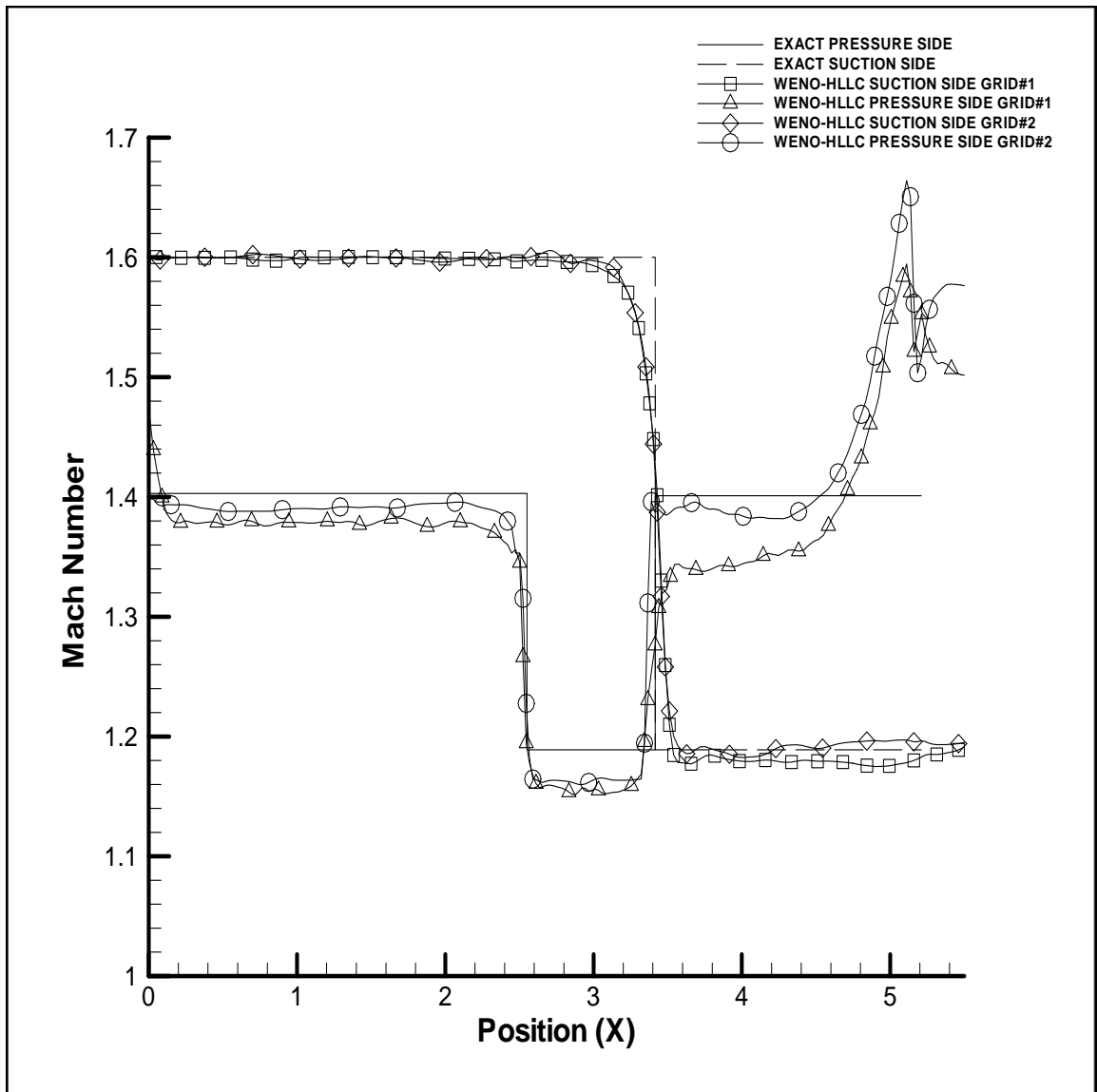
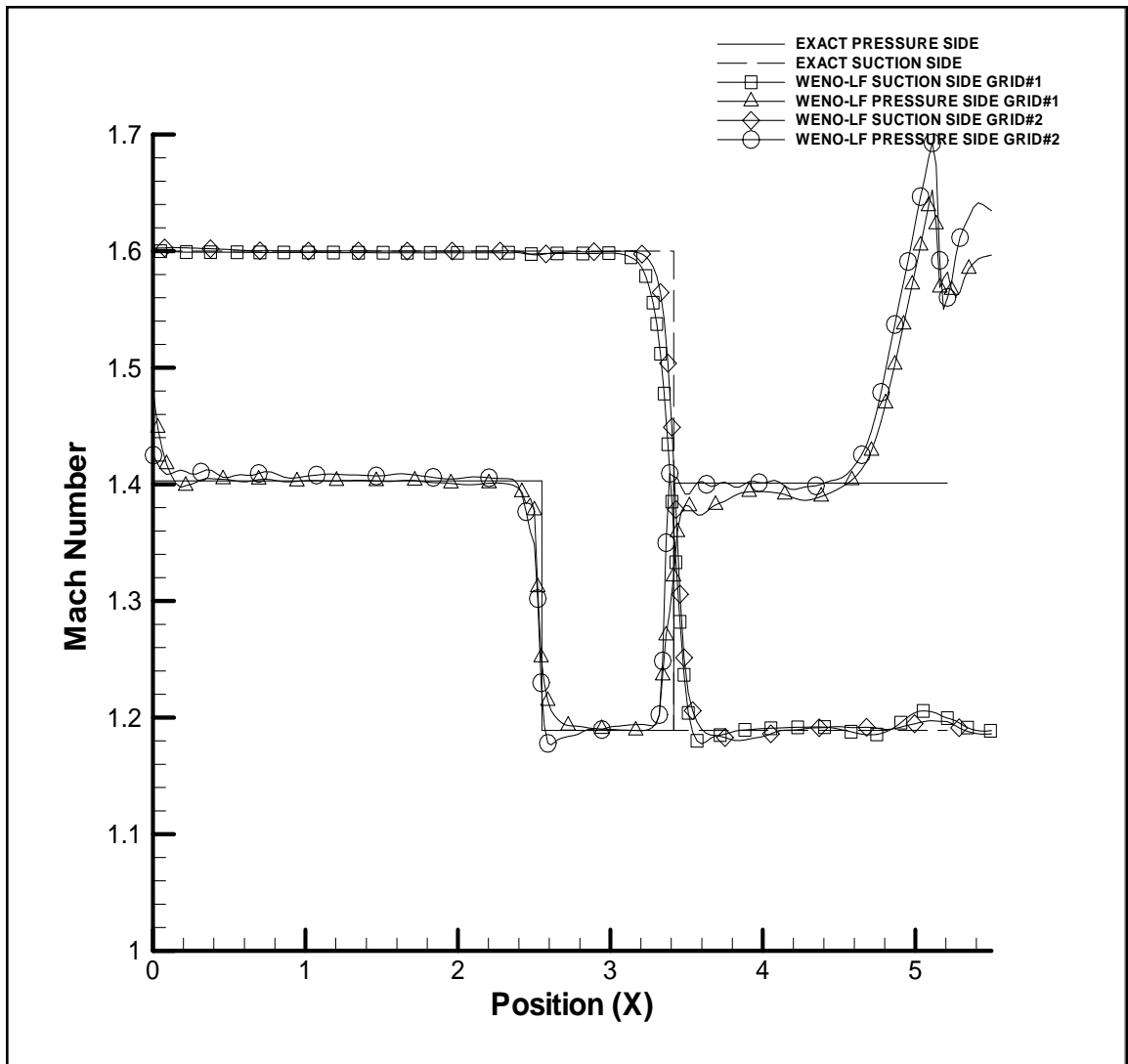


Figure 4.77. Mach number contour obtained by WENO-RUSANOV scheme



**Figure 4.78.** Comparison of Mach Number distributions obtained by WENO-HLLC scheme for different grids

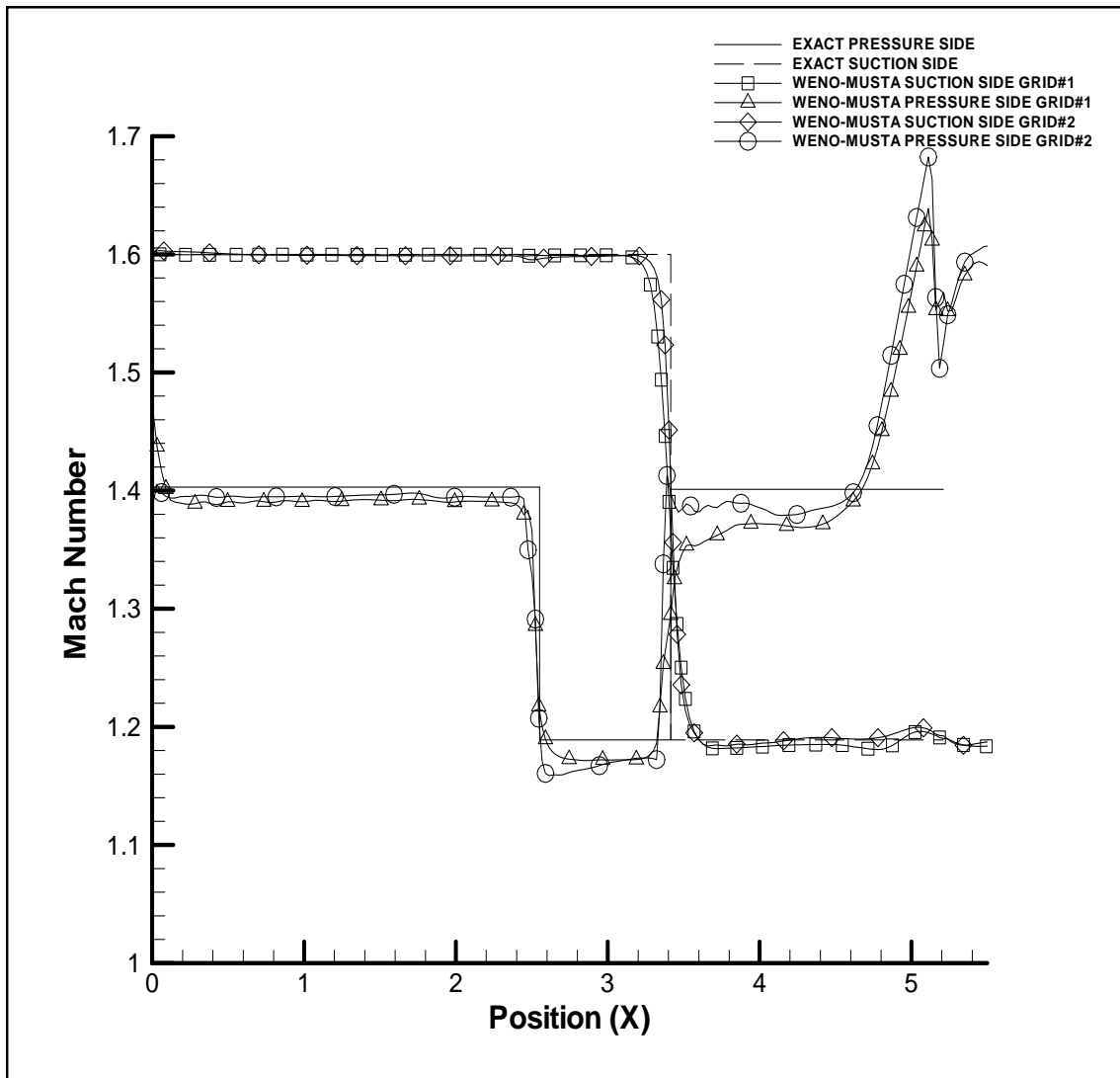
It can be observed from figure 4.78 that by the decreasing skewness of the grid along the boundaries the result of HLLC flux is improved. Also according to figure 4.74 the resolution of the scheme is increased and the shock wave thicknesses on the pressure side of the cascade wall is decreased.



**Figure 4.79.** Comparison of Mach Number distributions obtained by WENO-LF scheme for different grids

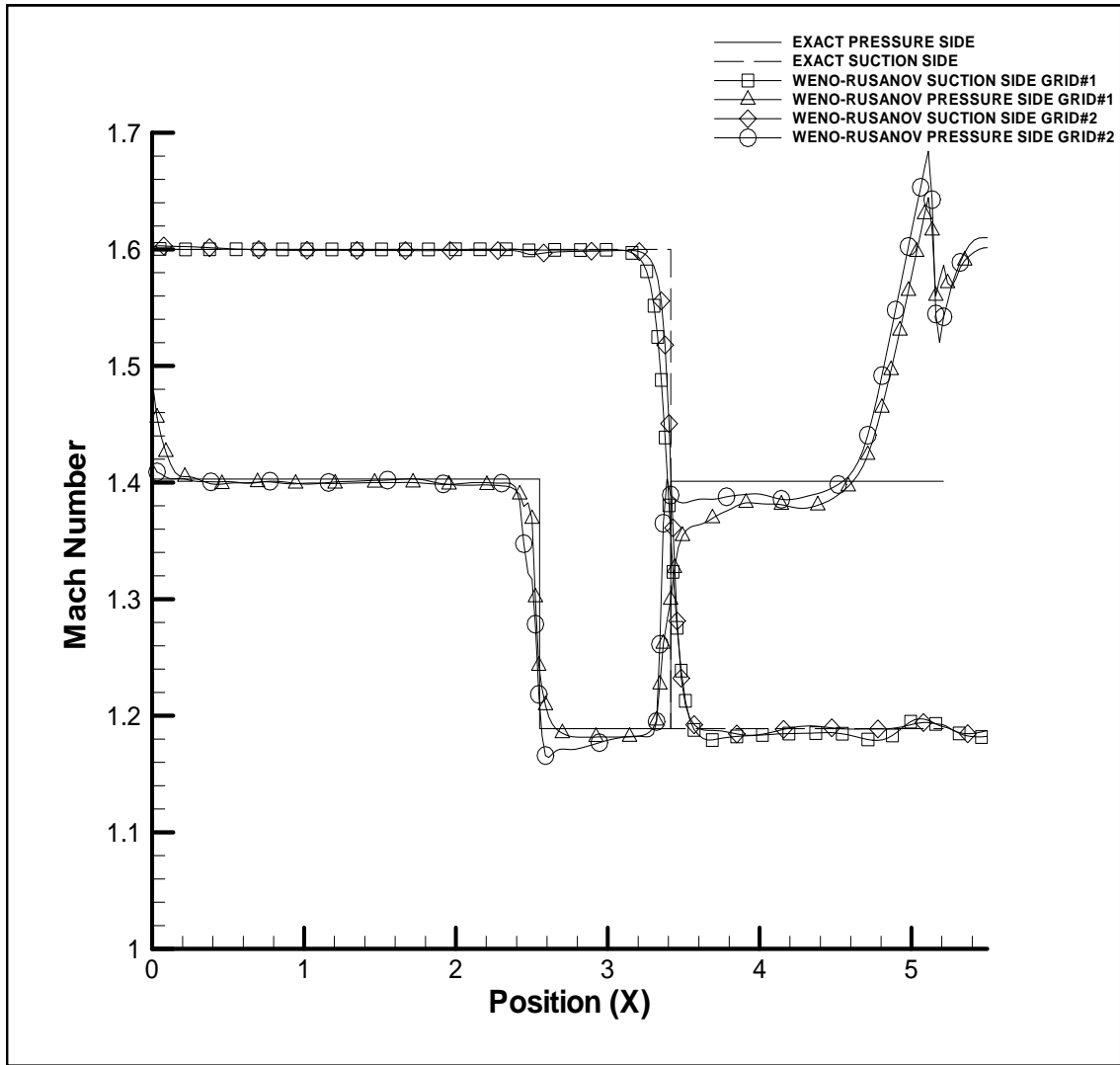
Unlike HLLC flux, using grid#2 with the Lax-Friedrich flux does not have obvious results. If the location where the first shock wave is occurred on the middle of the pressure side is considered, grid#2 disturbs the solution of the Lax-Friedrich. Whereas, the solution is improved after the expansion fan. (Figure 4.79)

Moreover, figure 4.75 shows that the resolution of the scheme is increased by using grid#2



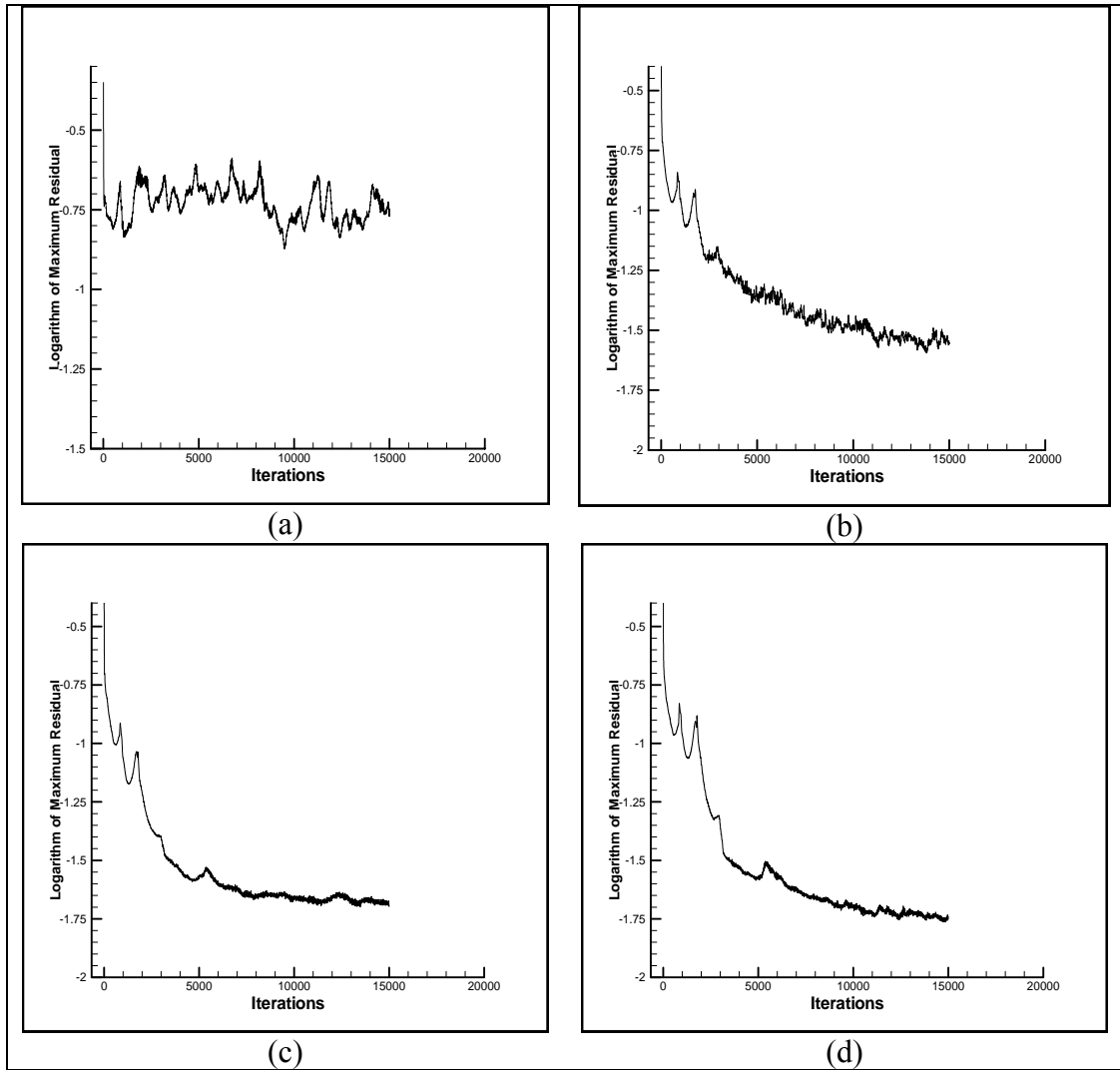
**Figure 4.80.** Comparison of Mach Number distributions obtained by WENO-MUSTA scheme for different grids

Figure 4.80 and Figure 4.81 show that using grid#2 has disturbed the results of WENO-MUSTA and WENO-RUSANOV schemes. As Lax-Friedrich flux, MUSTA flux has some improved profile after the expansion fan.



**Figure 4.81.** Comparison of Mach number distributions obtained by WENO-RUSANOV scheme for different grids

The solution obtained by Rusanov flux has been disturbed by less skewed meshes near the boundary. Using grid#2 provides no advantage for Rusanov flux.



**Figure 4.82.** Convergence History of the schemes (a) WENO-HLLC, (b)WENO-LF, (c) WENO-MUSTA, (d)WENO-RUSANOV

Figure 4.82 shows the convergence history of the schemes for grid#2, As concluded before, WENO schemes does not have strong convergence. The weakest scheme is the WENO-HLLC scheme.

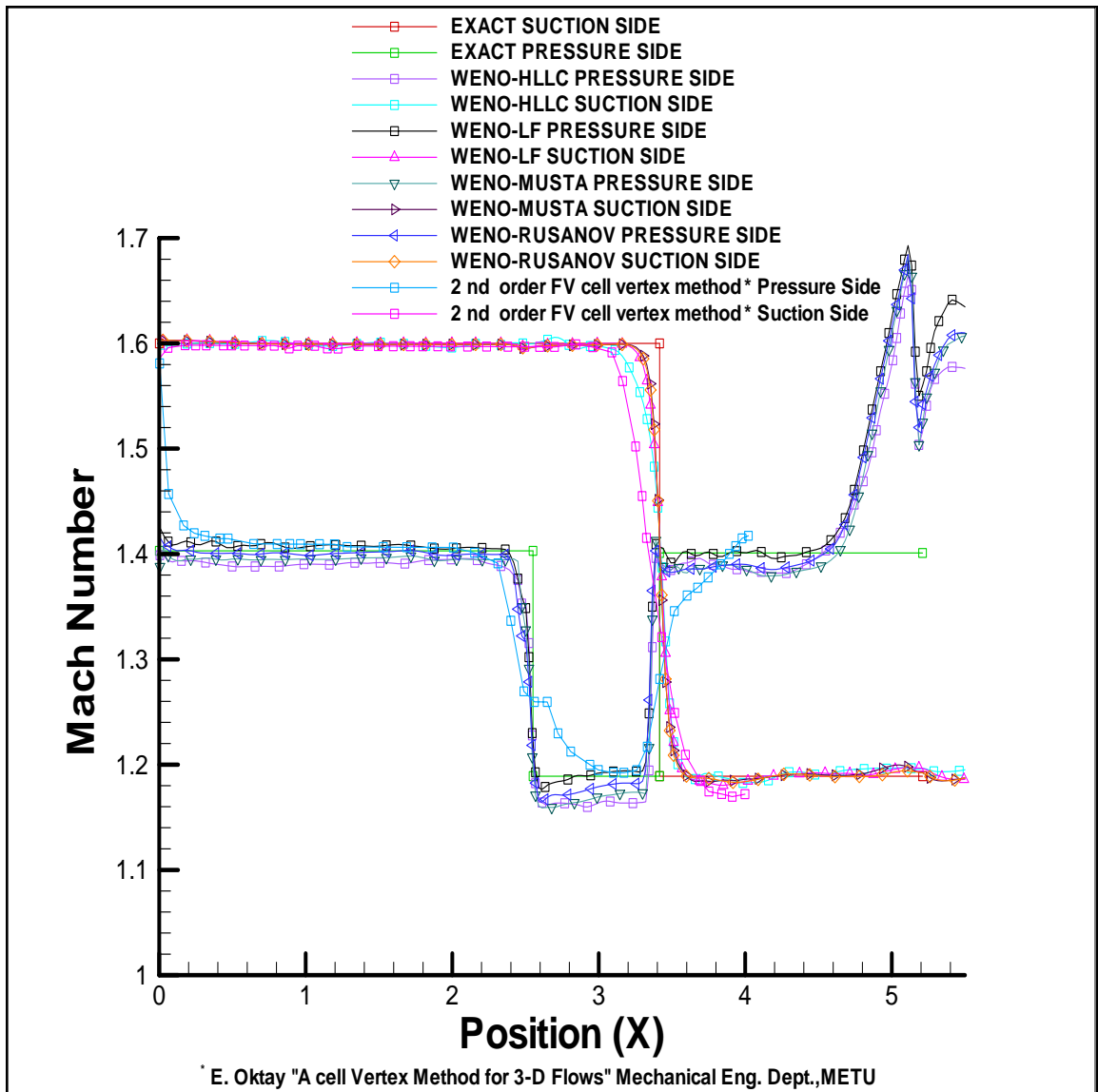


**Figure 4.83.** Comparison of Mach number distributions for all schemes for grid #2

Finally, in figure 4.83 all the fluxes are compared for grid#2. Using less skewed grids has some advantages and disadvantages. Firstly, it provided more sharp fits for the shock and expansion fan of the pressure. Also it has provided the solution of HLLC flux to be more accurate. However, it has disturbed the solution for the other fluxes.

## CHAPTER 5

### CONCLUSION

This thesis aimed to develop higher order FV-WENO scheme with different flux algorithms for solving two-dimensional Euler equations on complicated structures. The scheme and fluxes are tested for one and two-dimensions.

FV-WENO scheme has provided superior performance for 1-D Shock tube problem. Almost all the fluxes fit the exact solution of the problem. The difference in fluxes can be seen only when critical regions are closely investigated. The critical regions involve; expansion fan, contact surface, shock wave regions. In expansion fan region, the HLLC flux has the best fit with the exact solution. Also in contact surface and shock wave regions, the result of Lax-Friedrich flux is the best one. The Rusanov and Musta fluxes also have approximate results with Lax-Friedrich flux. These superior solutions were expected for FV- WENO schemes in 1-D. Also the behavior of HLLC flux shows the ability of the flux to open the Riemann fan.

For 2-D, three test case problems are used to test the scheme and fluxes. Initially the Double Mach Reflection (DMR) problem is solved. DMR is a classical test case for higher-order schemes. DMR problem involves complicated shock wave structure but the computational domain is rectangular and smooth. The resolution of the schemes can be obtained by DMR problem. Generally, FV-WENO scheme has logical results for this test case. Two sizes of the grids are used for this case. The coarser grid result shows the resolution of all flux algorithms. HLLC flux gives higher resolution. After that, Musta flux has good resolution as HLLC flux. The Rusanov and Lax-Friedrich fluxes have worse resolution than the other ones. In finer grid case, some conclusions can be drawn about numerical dissipation of the

algorithms. The more instability means less numerical dissipation when same size of meshes is considered. So, HLLC flux the least dissipative scheme. After that, Musta flux has also less numerical dissipation. But Lax-Friedrich and Rusanov schemes are the most dissipative schemes.

Secondly, the scheme and fluxes are tested with 2-D supersonic channel flow problem. This test case problem involves shock structure. However, different than DMR problem; the computational domain is more complicated. The mesh is not smooth as in the DMR case. Also for this test case problem, a grid refinement study is done. In this study four fluxes are tested with four different sizes of the meshes. When the pressure distribution along the bottom wall is investigated, it can be concluded that the grid size affects HLLC flux mostly. Other fluxes behave almost same with different sizes of grid. As another conclusion HLLC flux is not suitable for complex geometries. Because it oscillates more than other fluxes where all the fluxes approximately fits the analytical solution. All the fluxes have good resolutions with bigger mesh size.

As a last one, the scheme and fluxes are tested with Staggered wedge cascade problem. In this test case problem, the computational domain is very complicated when compared with the others. Beside computational domain, boundary conditions imposed also makes problem complicated. For this test case different CFL numbers and different grids are used. In the first grid, the meshes near the wall boundary are highly skewed. For this mesh size two different CFL numbers are tested. Generally, all the fluxes are approximately same character for two different CFL numbers. FV-WENO scheme gives a reasonable result for this test case problem. However, the resolution of the results is not as good as the ones obtained for rectangular smooth domains. When all the fluxes are compared it can be observed that the most acceptable result is obtained by Lax-Friedrichs fluxes. The result of HLLC flux has underestimated the solution. In the second grid the meshes near the boundary are less skewed than the other fluxes. By doing this shock capturing property of the fluxes is improved. It can be concluded the grid dependency of the flux algorithms are increased when computational domain becomes complicated.

These results shows that FV-WENO scheme is very efficient on 1-D. In two-dimensions scheme is only efficient for smooth rectangular domains. When the domain gets complicated the accuracy and efficiency of the scheme is decreased. Also the accuracy of FV-WENO is much dependent on flux algorithms used.

For the efficiency of the scheme centered flux algorithms (Lax-Friedrichs, Rusanov) are feasible for the scheme. Because they are accurate and simple to use. The computational time required for FV-WENO scheme is very big. To use FV-WENO for very complicated shock structure and smooth computational domain is logical . But to use FV-WENO for complex computational domains would decrease the accuracy of the scheme.

As future works, 2-D FV WENO scheme can be extend in 3-D. Also in 2-D, FV-WENO scheme can be tried with multigrid methods. About the fluxes, the order of accuracy of the fluxes can be increased by using different features of the fluxes together. An implicit scheme can be developed. For 2-D; Unstructured FV-WENO reconstruction can be developed.

## REFERENCES

- [1] T. J. BARTH and H. DECONINCK, *High-Order Methods for Computational Physics*, Springer-Verlag, 1999.
- [2] C.-W. SHU, *TVB uniformly high order schemes for conservation laws*, *Mathematics of Computation*, v49 (1987), pp.105-121.
- [3] B. COCKBURN and C.-W. SHU, *TVB Runge-Kutta local projection discontinuous Galerkin finite element method for conservation laws II: general framework*, *Mathematics of Computation*, v52 (1989), pp.411-435.
- [4] G. A. SOD, *Numerical Methods in Fluid Dynamics*, Cambridge University Press, Cambridge, 1985.
- [5] R. J. LEVEQUE, *Numerical Methods for Conservation Laws*, Birkhauser Verlag, Basel, 1990.
- [6] E. GODLEWSKI and P.-A. RAVIART, *Numerical approximation of hyperbolic systems of conservation laws*, Springer, 1996.
- [7] A. HARTEN, B. ENGQUIST, S. OSHER, and S. CHAKRAVARTHY *Uniformly High-Order Accurate Non-Oscillatory Schemes*, *Journal of Computational Physics*, v71 (1987), pp.231-303.
- [8] C.-W. SHU, *Numerical Experiments on the Accuracy of ENO and Modified ENO Schemes*, *Journal of Scientific Computing*, v5 (1990), pp.127-149.
- [9] X. -D. LIU, S. OSHER and T. CHAN, *Weighted Essentially Non-Oscillatory Schemes*, *Journal of Computational Physics*, v115 (1994), pp. 200-212.
- [10] G. JIANG and C. -W. SHU, *Efficient implementation of weighted ENO schemes*, *Journal of Computational Physics*, v126 (1996), pp.202-228.

- [11] D. S. BALSARA and C. W. SHU, *Monotonicity Preserving Weighted Essentially Non-Oscillatory Schemes with Increasingly High Order of Accuracy*, Journal of Computational Physics. V160, (2000), pp. 405-452.
- [12] O. FRIEDRICH, *Weighted essentially non-oscillatory schemes for the interpolation of mean values on unstructured grids*, Journal of Computational Physics, v144 (1998), pp.194-212.
- [13] C. HU and C.-W. SHU, *High order weighted ENO schemes for unstructured meshes: preliminary results*, Computational Fluid Dynamics 98, Invited Lectures, Minisymposia and Special Technologies Sessions of the Fourth European Computational Fluid Dynamics Conference, K. Papailiou, D. Tsahalis, J. Piaux and D. Knorzer, Editors, John Wiley and Sons, v2, September 1998, pp.356-362.
- [14] C. HU and C.-W. SHU, *Weighted Essentially Non-Oscillatory Schemes on Triangular Meshes*, Journal of Computational Physics. V150, (1999), pp. 97-127.
- [15] D. LEVY, G. PUPPO and G. RUSSO, *Central WENO schemes for hyperbolic systems of conservation laws*, Mathematical Modelling and Numerical Analysis, v33 (1999), pp.547-571.
- [16] F. LAFON and S. OSHER, *High-order 2-dimensional non-oscillatory methods for solving Hamilton-Jacobi scalar equations*, Journal of Computational Physics, v123 (1996), pp.235-253.
- [17] J. SHI, C. HU and C.-W. SHU, *A Technique for Treating Negative Weights in WENO Schemes*, Journal of Computational Physics, v175 (2002), pp. 108-127.
- [18] V. A. TITAREV and E. F. TORO, *Finite-volume WENO schemes for three-dimensional conservation laws*, Journal of Computational Physics, v201, N.1 (2004), pp.238-260.

- [19] W. E and C.-W. SHU, *A Numerical Resolution Study of High Order Essentially Non-Oscillatory Schemes Applied to Incompressible Flow*, Journal of Computational Physics, v110 (1994), pp.39-46.
- [20] E. F. TORO, *Riemann Solvers and Numerical Methods for Fluid Dynamics*, Second Edition, Springer-Verlag, 1999.
- [21] J. QIU and C.-W. SHU, *On the Construction, Comparison, and Local Characteristic Decomposition for High Order Central WENO Schemes*, Journal of Computational Physics, v183 (2002), pp. 187-209.
- [22] D. Kröner, *Numerical Schemes for Conservation Laws*, Wiley Teubner, 1997.
- [23] C. HIRSCH, *Numerical Computation of Internal and External Flows, Vol II: Computational Methods for Inviscid and Viscous Flows*, Wiley, 1990.
- [24] E. F. TURO, *Multi-stage predictor-corrector fluxes for hyperbolic equations*, Preprint NI03037-NPA. Isaac Newton Institute for Mathematical Sciences, University of Cambridge, UK, submitted to Journal of Computational Physics, 2003.
- [25] E. F. TORO and V. A. TITAREV, *MUSTA schemes for systems of conservation laws*, Preprint NI04033-NPA. Isaac Newton Institute for Mathematical Sciences, University of Cambridge, UK, 2003.
- [26] V. A. TITAREV and E. F. TORO, *MUSTA schemes for multi-dimensional hyperbolic systems: analysis and improvements*, Preprint NI04032-NPA. Isaac Newton Institute for Mathematical Sciences, University of Cambridge, UK, 2003.
- [27] E. SARIGÖL, *Weighted essentially non-oscillatory (WENO) euler solution of two-dimensional high speed flows*, MS Thesis, METU, Ankara, 2002.

- [28] M. A. ELFARRA, *Two-dimensional finite volume weighted essentially non-oscillatory euler schemes with uniform and non-uniform grid coefficients*, MS Thesis, METU, Ankara, 2005.
- [29] K. A. HOFFMANN and S. T. CHIANG, *Computational Fluid Dynamics*, EES, v2 (2000).
- [30] G. A. SOD, *A survey of several finite difference methods for systems of nonlinear hyperbolic conservation laws*, *Journal of Computational Physics*, v27 (1978), pp. 1-32.
- [31] P. D. LAX, *Weak solutions of non-linear hyperbolic equations and their numerical computations*, *Communications in Pure and Applied Mathematics*, v7 (1954), pp.159-193.
- [32] P. WOODWARD and P. COLELLA, *The numerical simulation of two-dimensional fluid flow with strong shocks*, *Journal of Computational Physics*, v54 (1984), pp. 115-173.
- [33] J. D. ANDERSON, *Fundamentals of Aerodynamics*, McGraw Hill, Third Edition, 2001.
- [34] AGART ADVISORY, *Test Cases for Computation of Internal Flows in Aero engine Components*, Report No. 275.
- [35] C.-W. SHU, T. A. ZANG, G. ERLEBACHER, D. WHITAKER, and S. OSHER, *High Order ENO Schemes Applied to Two- and Three- Dimensional Compressible Flow*, *Applied Numerical Mathematics* V9, (1992), pp. 45-71.
- [36] S. C. CHAPRA and R. P. CANALE, *Numerical Methods for Engineering*, McGraw Hill, Third Edition, 1998.
- [37] E. F. TORO, M. SPRUCE, and W. SPEARES, *Restoration of the Contact Surface in the HLL-Riemann Solver*, *Shock Waves*, v4 (1994), pp. 25-34.

- [38] S. F. DAVIS, *Simplified Second-order Godunov-Type Methods*, SIAM Journal of Sci. Stat. Comput., v9 (1988), pp.445-473.
- [39] V. V. RUSANOV, *Calculation of Interaction of Non-steady Shock Waves with Obstacles*, Journal of Comput. Mathematics and Physics, v1 (1961), pp.267-279.

# APPENDIX

## A. CODE DESCRIPTION AND FLOW CHARTS

The code consists of 8 subroutines: the MESH, INIT, BC, FLUX\_X, FLUX\_Y, WENO,CFLC, RK, and STORE. In the MESH subroutine, grid is read and the ghost points are set outside the computational domain, also  $dx$  and  $dy$  needed for the spatial integration are calculated at each grid point. Needed metrics for the boundary conditions and for finding normal and tangential velocity components are also calculated here. The grid coefficients constants are evaluated in this subroutine.

In the INIT subroutine, the CFL number and the initial conditions are set, and the boundary conditions are set in the BC subroutine.

In FLUX\_X subroutine, first the Cartesian velocity components  $u$  and  $v$  are transformed into normal and tangential components using:

$$V_n = \frac{u \xi_x + v \xi_y}{\sqrt{\xi_x^2 + \xi_y^2}}$$

$$V_t = \frac{v \xi_x - u \xi_y}{\sqrt{\xi_x^2 + \xi_y^2}}$$

those are the velocity components to be used though out this subroutine.

Then, Roe-averaging is applied. The eigenvalues and the corresponding eigenvectors and inverse eigenvectors are calculated. WENO subroutine is called in

which the reconstruction is performed to obtain the fluxes at the cell faces. After getting the fluxes, the ones corresponding to  $x$  and  $y$  momentum equations  $f_x, f_y$  are transformed back into Cartesian using:

$$Fx = \frac{f_x \xi_x - f_y \xi_y}{\sqrt{\xi_x^2 + \xi_y^2}}$$

$$Fy = \frac{f_y \xi_x + f_x \xi_y}{\sqrt{\xi_x^2 + \xi_y^2}}$$

In FLUX\_Y subroutine, again the Cartesian velocity components  $u$  and  $v$  are transformed into normal and tangential components using:

$$V_n = \frac{u \eta_x + v \eta_y}{\sqrt{\eta_x^2 + \eta_y^2}}$$

$$V_t = \frac{v \eta_x - u \eta_y}{\sqrt{\eta_x^2 + \eta_y^2}}$$

those are the velocity components to be used though out this subroutine.

Then, Roe-averaging is applied. The eigenvalues and the corresponding eigenvectors and inverse eigenvectors are calculated. WENO subroutine is called in which the reconstruction is performed to obtain the fluxes at the cell faces. After getting the fluxes, the ones corresponding to  $x$  and  $y$  momentum equations  $f_x, f_y$  are transformed back into Cartesian using:

$$F_x = \frac{f_x \eta_x - f_y \eta_y}{\sqrt{\eta_x^2 + \eta_y^2}}$$

$$F_y = \frac{f_y \eta_x + f_x \eta_y}{\sqrt{\eta_x^2 + \eta_y^2}}$$

In the WENO subroutine, One dimensional WENO reconstruction is applied Also The fluxes ,(HLLC ,MUSTA, Lax-Friedrich and Rusanov) are implemented.

In the CFLC subroutine, the time increment  $dt$  is calculated.

The time discretization is carried in the RK subroutine using 3<sup>rd</sup> order TVD RK method.

Iterative procedure includes: BC, FLUX\_X, FLUX\_Y, WENO, CFLC and RK subroutines. Finally the results obtained from the RK subroutine are stored in the STORE subroutine.

The following flow chart explains the code:

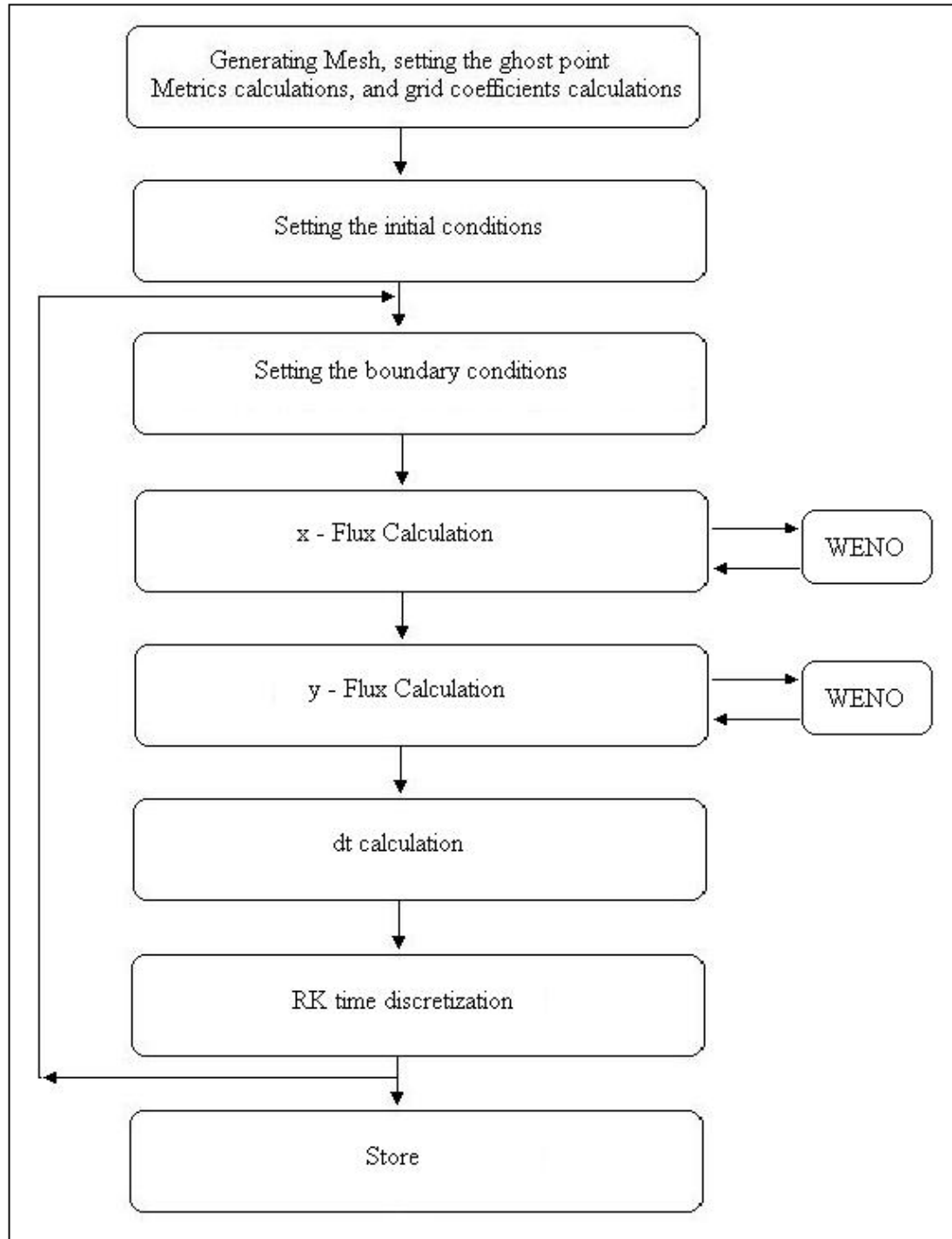


**Figure A.1.** Algorithm flow chart [28]